Structure of Excited States Seen in Double Beta Decay Investigated with the ^{148}Nd(^{3}He, nγ)^{150}Sm and ^{98}Mo(^{3}He, nγ)^{100}Ru Two proton Stripping Reactions.

by

Preston Vymers

Dissertation presented for the degree of Doctor of Philosophy in the Faculty of Science at Stellenbosch University

Department of Physics
University of
Stellenbosch
Private Bag X1, Matieland 7602, South Africa

Supervisors:

Prof Paul Papka
University of Stellenbosch

Prof J.F. Sharpey-Schafer
University of the Western Cape

December 2019

Declaration

By submitting this dissertation electronically, I declare that the entirety of the work contained therein is my own, original work, that I am the sole author thereof (save to the extent explicitly otherwise stated), that reproduction and publication thereof by Stellenbosch University will not infringe any third party rights and that I have not previously in its entirety or in part submitted it for obtaining any qualification.

December 2019

Abstract

Structure of Excited States Seen in Double Beta Decay Investigated with the ^{148}Nd(^{3}He, nγ)^{150}Sm and ^{98}Mo(^{3}He, nγ)^{100}Ru Two proton Stripping Reactions.

P. Vymers

Department of Physics
University of Stellenbosch
Private Bag X1, Matieland 7602, South Africa

Dissertation: PhD (Physics)

December 2019

The two proton transfer reaction (^{3}He, nγ) has been measured on two targets ^{98}Mo and ^{148}Nd. High resolution data were taken using the neutron time of flight method and a wall of six NE102A plastic scintillator trigger detectors. These were operated in coincidence with the AFRODITE HPGe detector array to detect the γ-rays that originates from ^{100}Ru and ^{150}Sm. Thus made it possible to investigate the validity of the BCS proton pair stripping approximations. That is assumed in the nuclear matrix element calculations of the QRPA based models, for decays to the ground states of the candidate $0\nu\beta\beta$ nuclei. A strong proton pair stripping $L = 0$ transition to the $I^{\pi} = 0_2^+$ spin state of ^{100}Ru has been observed, while non were found for the case of ^{150}Sm due to technical problems. This indicate a breakdown of the BCS proton pairing description in the ground state of ^{100}Ru. In addition the low-lying spin members ($I^{\pi} = 2_1^+$, 4_1^+, 6_1^+ and 8_1^+) of the yrast bands of both nuclei are clearly visible. Their population are attributed to the single neutron fusion evaporation channels.

Uittreksel

Titel van proefskrif in Afrikaans

P. Vymers

Fisika Departement
Universiteit van Stellenbosch
Privaatsak X1, Matieland 7602, Suid-Afrika

Proefskrif: PhD (Fisika)

Desember 2019

Die twee proton direkte oordrag reaksie (^{3}He, nγ) was uitgevoer op die ^{98}Mo soveel as op die ^{148}Nd teiken kerne. Hoe resolusie γ-stralings meetings was waargeneem met die AFRODITE spektrometer in kominasie met die NE102A plastiek sintillator detektore. Waar die laas genoemde detektore gebruik was om die neutrone op te neem deur middel van die vlieg tyd metode. Hierdie metode het dit moontlike gemaak om die geldigeheid van die BCS proton paar oordrag benadering, wat in die QRPA modelle vir die grond toestand oorgegange wat vir die $0\nu\beta\beta$ kandidaat kerne van ^{100}Ru en ^{150}Sm aanvaar word te ondersoek. n Sterk proton paar $L = 0$ oordrag na die opgewekte $I^\pi = 0_2^+$ vlak van ^{100}Ru was wargeneem, maar geen soortgelyke oorgang was gewas waargeneem vir die ^{150}Sm kern, as gevolge van tegniese redes. Die ^{100}Ru waarneeming stel voor n afbreek van die BCS proton paar oordrag aanname. Verder die opgewekte toestande ($I^\pi = 2_1^+$, 4_1^+, 6_1^+ en 8_1^+) van beide kerne was duidelike waargeneem tydens die meetings, dit word toegeskrywe aan kern saammesmelting.

Acknowledgements

I am very thankfull to my thesis advisor, Professor Paul Papka for his willingness to take me on as a PhD student, for the assistance with setting up the experimental setup and for the interest during all phases of this work. The advice and encouragement extends also to my co-supervisor Professor John Sharpey-Schafer who suggested the measurement and for the valuable discussions that we had to clear up misconceptions. I also want to thank Dr. Pete Jones for the assistance with the setup and Midas data acquisition system. A word of thanks to Dr. Bongani Maqabuka for his many weekends of assistance to sort the data on Midas and general discussions. Also want to express my appreciation to the South African tax payer for their financial support via the national research foundation (NRF). Finally thanks to all who participated to data acquisition.

Dedications

This dissertation is dedicated to my family who encouraged me to pursue my dreams and finish my dissertation.

Chapter 1

Double Beta Decay

1.1 Motivation

Normal double β-decay happens when a nucleus (A,Z) with proton number Z and mass number A converts a neutron pair into a proton pair $(A,\ Z{+}2)$ and two electrons $(2e^-)$ and two electron anti-neutrinos $(2\bar{\nu}_e)$ are emitted. Thereby the daughter nucleus can reach a more stable energy configuration. This decay process is described in equation 1.1 and illustrated in Fig.1.1.

$$(A, Z) \rightarrow (A, Z + 2) + 2e^- + 2\bar{\nu}_e \tag{1.1}$$

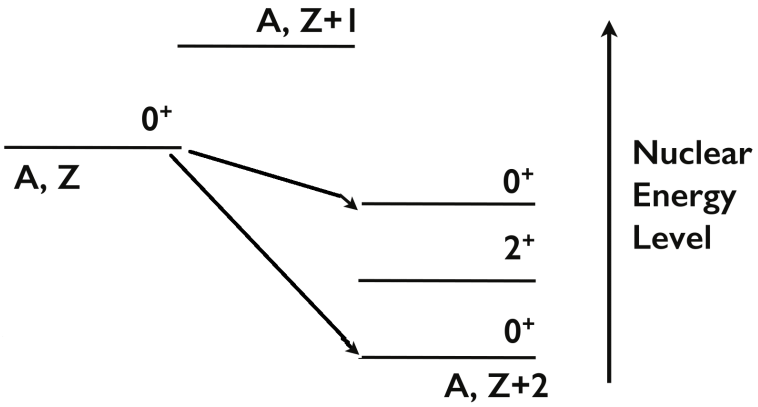

Figure 1.1: A schematic double β-decay energy scheme; where the decay goes from the ground state of the mother nucleus $(A,\ Z)$ directly to the ground state of the grand-daughter nucleus $(A,\ Z{+}2)$. Decay to the intermediate nucleus $(A,\ Z{+}1)$ is energetically forbidden.

It takes place between two even-even isobars when the decay to an intermediate nucleus is energetically forbidden due to the pairing interaction. This type of decay conserves the lepton number and was first postulated by Goeppert-Mayer in 1935

[1, 2]. It was only discovered in the laboratory in 1987 in ^{82}Sr [1, 3] by detecting the two emitted electrons. Their kinetic energy sum did not exactly match the reaction Q-value end point see Fig 1.2. Therefore it was deduced that the missing energy was carried away by the emitted antineutrinos. Furthermore it is a second order nuclear weak process, which accounts for the rarity of this radioactive decay mode. Currently it has been observed in the eleven isotopes listed in Table 1.1. [4]. The decay is more likely to occur in nuclei that have large reaction Q-values with decay half-lifes $t^{2\nu}_{1/2}$ that range from 10^{18} to 10^{21} years and are described by equation 1.2:

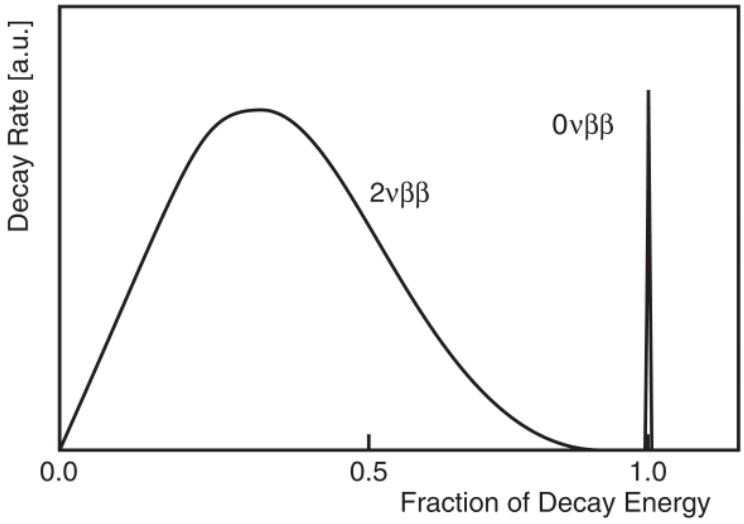

Figure 1.2: The kinetic energy summed spectrum for the two electrons that are emitted from this $2\nu\beta\beta$-decay process and the expected two electron kinetic energy summed spectrum for the $0\nu\beta\beta$-decay mechanism are shown [5].

$$(t^{2\nu}_{1/2})^{-1} = G^{2\nu}(Q, Z)|M^{2\nu}|^2. \tag{1.2}$$

Where $G^{2\nu}(Q, Z)$ is the phase space factor term that contains the charge and reaction Q-values. The nuclear matrix element term $M^{2\nu}$ holds all the essential physics. The latter term cannot be measured but can only be deduced by measuring $(t^{2\nu}_{1/2})$. Many different approaches are followed in order to calculate its value for a specific decay. Ranging from the interacting boson model (IBM) [6], the large scale shell models (LSSM) [7], to the quasiparticle random phase approximation (QRPA) [8, 9] amongst others. The latter model assumes that both the ground state of the mother nucleus and daughter nucleus have a collective origin.

$$(Z, A) \rightarrow (Z + 2, A) + 2e^- \tag{1.3}$$

Apart from the $2\nu\beta\beta$-decay, there is also $0\nu\beta\beta$-decay (equation 1.3), a hypothesized process currently under scrutinty that has never been observed in which only electrons would be emitted. In 1937, Ettore Majorana [1, 10] demonstrated that all results of β-decay theory remain unchanged if the neutrino were its own

Table 1.1: The listed 2ν 2β-decay nuclei with their corresponding reaction Q-values, $I^\pi = 0_2^+$ spin states excitation energies and γ-ray transitions from the $I^\pi = 0_2^+$ spin states [4]. Double β-decay to the $I^\pi = 0_2^+$ spin state have been found only for the ^{150}Nd to ^{150}Sm and for the ^{100}Mo to ^{100}Ru decays.

Nucleus	Q-value [keV]	$I^\pi = 0_2^+$ [keV]	γ-ray lines [keV]
^{48}Ca $\rightarrow$ ^{48}Ti	4271	2997.22	2013.66, 983.53
^{76}Ge $\rightarrow$ ^{76}Se	2040	1122.28	563.18, 559.10
^{82}Ge $\rightarrow$ ^{82}Kr	2995	1487.60	711.2, 776.52
^{96}Zr $\rightarrow$ ^{96}Mo	3350	1148.13	369.80, 778.22
^{100}Mo $\rightarrow$ ^{100}Ru	3034	1130.2	590.79, 539.51
^{110}Pd $\rightarrow$ ^{110}Cd	2013	1473.07	815.31, 657.76
^{116}Cd $\rightarrow$ ^{116}Sn	2802	1756.86	463.25, 1293.56
^{124}Sn $\rightarrow$ ^{124}Te	2228	1657.28	1051.55, 602.73
^{130}Te $\rightarrow$ ^{130}Xe	2533	1793.52	1257.5, 671.9, 586.05, 536.07
^{136}Xe $\rightarrow$ ^{136}Ba	2479	1578.99	760.49, 818.51
^{150}Nd $\rightarrow$ ^{150}Sm	3367	740.46	406.51, 334.96

anti-particle (requiring the neutrino to have mass), now known as a Majorana particle. In 1939, Wendell H. Furry [1, 11] proposed that if neutrinos are Majorana particles, then double β-decay can proceed without the emission of any neutrinos. Through the neutrino annihilating with its antineutrino partner resulting in neutrinoless double β-decay. This emplies that the expected electron spectrum must be a delta function at maximum Q-value, again see Fig 1.2. It is not yet known whether the neutrino is a Majorana particle and, relatedly, whether neutrinoless double β-decay exists in nature. It must be noted that this decay process violates lepton number conservation as set out in the standard model and the rate of decay is described by equation 1.4:

$$(t_{1/2}^{0\nu})^{-1} = G^{0\nu}(Q, Z)|M^{0\nu}|^2 < m_{\beta\beta} >^2. \tag{1.4}$$

where $m_{\beta\beta}$ is the effective Majorana mass of the electron neutrino, given by

$$< m_{\beta\beta} >^2 = |\sum_{i=1}^{3} |U_{ei}|^2 e_i^{i\alpha} m_i|^2. \tag{1.5}$$

where m_i are the masses of the neutrino flavors, α_i are the Majorana phases (flavors) and U_{ei} is the unitary neutrino mixing matrix. It relates the flavors and mass eigenbasis and is parameterised as:

$$\nu_\alpha = \sum_i^3 U_{\alpha i}^* \nu_i. \tag{1.6}$$

$$\nu_i = \sum_i^3 U_{\alpha i}\nu_\alpha. \tag{1.7}$$

where

- ν_i is a neutrino with mass m_i = 1,2,3.
- ν_α is a neutrino with flavor $\alpha = \tau$, μ, electron.

Recently it was found that ^{100}Mo [12] undergoes $2\nu\beta\beta$-decay to excited spin state of ^{100}Ru in particular to the $I^\pi = 0_2^+$ spin state that is located at 1130 keV excitation energy (see Fig 1.3). Similairly ^{150}Nd [13] was also found to undergoes $2\nu\beta\beta$-decay to the $I^\pi = 0_2^+$ spin state of ^{150}Sm that is located at 740 keV excitation energy in the decay scheme (see Fig 1.4). Thereafter both nuclei undergo γ-ray decay to their respective ground states. These two isotopes are currently the only two nuclei where $2\nu\beta\beta$-decay to the $I^\pi = 0_2^+$ spin states is observed. A half-life of $t_{1/2}^{2\nu}$ = $[5.9^{+1.7}_{-1.1} \pm 0.6] \times 10^{20}$ yr for the decay of ^{100}Mo to ^{100}Ru and a half-live of $t_{1/2}^{2\nu}$ = $(1.33^{+0.63}_{-0.36}) \times 10^{20}$ yr for the decay of ^{150}Nd to ^{150}Sm were extracted.

Again the QRPA based models assumes that the ground states of the mother (^{100}Mo and ^{150}Nd) and daughter (^{100}Ru and ^{150}Sm) nuclei are collective and can be approximated by the BCS pairing description. However it is not known if this approximation is still valid after the detection of a $I^\pi = 0_2^+$ spin state. The best available tools to answer this question are the two nucleon transfer reactions in particular the (^{3}He, n) two-proton stripping reaction. The observation of large proton pair strengths to the ground states wills validates the BCS pairing hypothesis. However appreciable strengths to the $I^\pi = 0_2^+$ spin states is an indication of a collapse of the BCS theory and thus will require a review of the nuclear structure assumptions contained in the nuclear matrix element formula of the QRPA based formalisms.

Thus it is important to have a good understanding of the proton pair component of the $I^\pi = 0_2^+$ spin states wave functions of ^{100}Ru and ^{150}Sm. Since these two nuclei are candidates for the possible detection of the $0\nu\beta\beta$-decay mode, if observe the latter spin states, wave functions information will be needed to extract the nuclear matrix elements values and indirectly the neutrino mass.

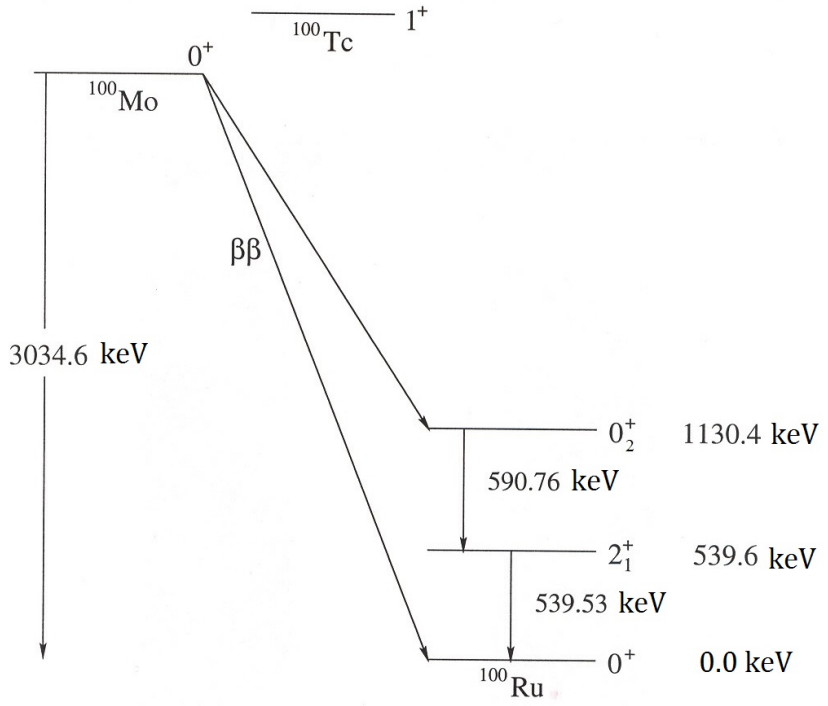

Figure 1.3: The ^{100}Mo $2\nu\beta\beta$-decay scheme to excited states in ^{100}Ru. Decay to ^{100}Tc is energetically forbidden [12].

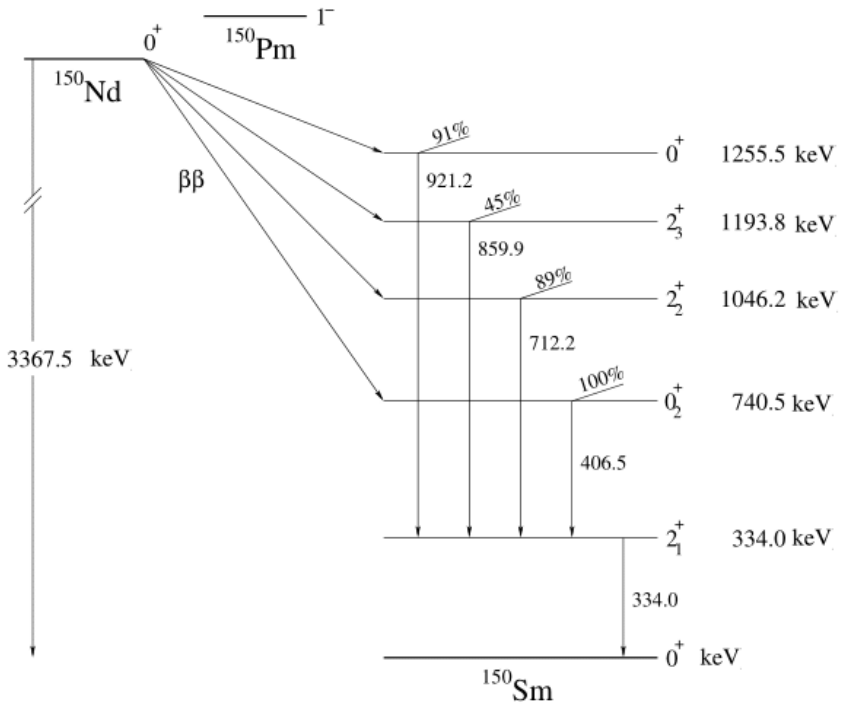

Figure 1.4: The ^{150}Nd $2\nu\beta\beta$-decay scheme to excited states in ^{150}Sm. Decay to ^{150}Pm is energetically forbidden [13].

Chapter 2

Collective $I^{\pi} = 0_2^+$ spin states

2.1 Collective Excitations

The aim of this chapter is to show how collective nuclear shape oscillations can result in low-lying $I^{\pi} = 0_2^+$ spin states. The nuclear shape deformations will first be discussed followed by the collective excitational modes.

$$R(\theta, \phi) = R_0[1 + \sum_{\lambda} \sum_{\mu} \alpha_{\lambda\mu} Y_{\lambda\mu}(\theta, \phi)] \tag{2.1}$$

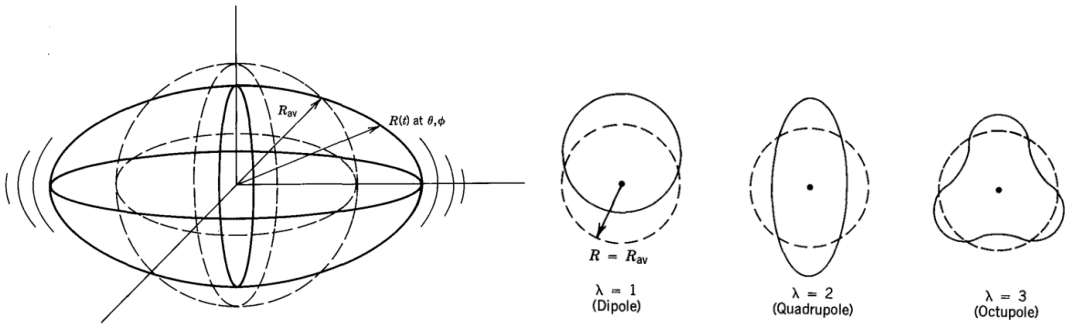

Figure 2.1: Collective nuclear shape oscillations [14].

The nucleus can be viewed as an incompressible spherical liquid drop with radius R_0 given in equation 2.1. Any shape distortion $R(\theta, \phi)$ (see Fig.2.1) away from sphericity can be described by expressing R_0 as multiple expansions in spherical harmonics $Y_{\lambda\mu}(\theta, \phi)$. Here the parameter $\alpha_{\lambda\mu}$ denotes the distortions from an equilibrium spherical shape, λ is the multipolarity (angular momentum: l) of the surface with μ the angular momentum z projection also known as m. The quantity μ takes $(2\lambda + 1)$ integer values between - λ to λ. The $\lambda = 0$ term indicates monopole vibrations which corresponds to compressions and decompressions of the nuclear surface. This type of oscillation occur at high excitation energy at

roughly $E_0 \sim 80A^{-1/3}$MeV above the ground state in even-even nuclei, due to the incompressibility of the nuclear fluid. The $\lambda = 1$ term is not considered as it corresponds to a translation of the centre of mass. The most important collective low energy excitations of the nucleus are the $\lambda = 2$ (quadrupole), the $\lambda = 3$ (octupole) and the $\lambda = 4$ (hexadecapole) modes which are all illustrated in Fig 2.1, higher modes are unimportant.

$$R(\alpha_2, \theta, \phi) = R_0[1 + \sum_\mu [\alpha_{2\mu} Y_{2\mu}(\theta, \phi)]. \tag{2.2}$$

This analysis is restricted to the description of quadrupole shapes which will be discussed. Equation 2.2 describes the radius of a quadrupole deformed nucleus in the body fixed frame. The quadrupole body fixed distortion $(\alpha_{22}, \alpha_{14}, \alpha_{20}, \alpha_{2-1}, \alpha_{2-2})$ can be related to those in the laboratory reference frame by relation 2.3 (see eq 2.15 for definitions)

$$\alpha_{2\mu} = \sum_\nu D^*_{\mu\nu}(\theta_I) a^*_{2\nu} \tag{2.3}$$

If the principal axes of the laboratory coincide with the nuclear body fixed frame, then $\alpha_{22} = \alpha_{2-2}$ and $\alpha_{21} = \alpha_{2-1} = 0$. The three Euler angles Ψ, ϑ and φ together with the coefficients α_{20} and α_{22} and the polar coordinates $(\beta_2,\ \gamma)$ completely describe the system. In terms of the polar coordinates α_{20} and α_{22} are equal to

$$\begin{aligned} \alpha_{20} &= \beta_2 cos(\gamma) \\ \alpha_{22} &= -1/\sqrt{2}\beta_2 sin(\gamma) \end{aligned} \tag{2.4}$$

where the parameter β_2 indicates the total deformation along the symmetry axis and is given by:

$$\beta_2^2 = \sum_\mu |\alpha_{2\mu}|^2. \tag{2.5}$$

The coefficient γ indicates the lengths along the principal axes. For $\gamma = 0^0$ the shape is prolate and for $\gamma = 60^0$ the shape is oblate.

2.1.1 Spherical Vibrational Modes

Simple spherical harmonic quadrupole ($\lambda = 2$) surface vibrations will be discussed to show that $I^\pi = 0_2^+$ spin states can result from such oscillations. In Fig 2.2 the excitation energy spectra of a spheroidal nucleus is shown in the left illustration. Starting from the classical Lagrange and Hamiltonian functions for a vibrating surface

$$L_{coll}(\alpha_{\lambda,\mu}, \dot{\alpha}_{\lambda,\mu}) = \frac{1}{2} \sum_{\lambda,\mu} (B_\lambda |\dot{\alpha}_{\lambda,\mu}|^2 - C_\lambda |\alpha_{\lambda,\mu}|^2). \tag{2.6}$$

where the parameters B_λ are the inertia coefficients or collective masses and C_λ are the stiffness coefficients for the collective potential. The classical Hamiltonian

can also be written in terms of the conjugate momenta term $\pi_{\lambda,\mu}$.

$$H_{coll}(\pi_{\lambda,\mu}, \alpha_{\lambda,\mu}) = \sum_{\lambda,\mu}(\frac{|\pi_{\lambda,\mu}|^2}{2B_\lambda} - \frac{C_\lambda}{2}|\alpha_{\lambda,\mu}|^2). \tag{2.7}$$

Upon quantization of equation 2.7 the harmonic multipole vibrator Hamiltonian is now written as:

$$H_{coll} = \sum_{\lambda=0}^{\infty}\sum_{\mu=-\lambda}^{+\lambda}\hbar\omega_\lambda(\hat{\beta}^+_{\lambda,\mu}\hat{\beta}_{\lambda,\mu} + \frac{1}{2}). \tag{2.8}$$

where $\omega_\lambda = \sqrt{\frac{C_\lambda}{B_\lambda}}$ is the oscillation frequency term and $\hat{\beta}^+_{\lambda,\mu}$ is the oscillation quantum phonon creation operator, while $\hat{\beta}_{\lambda,\mu}$ is the phonon annihilation operator. The term $\hat{\beta}^+_{\lambda,\mu}\ \hat{\beta}_{\lambda,\mu}$ counts the number of phonons. The lowest lying state is the phonon vacuum and is written as:

$$|N = 0, \lambda = 0, \mu = 0 \tag{2.9}$$

Its energy is the zero point energy:

$$H0 = \frac{5}{2}\hbar\omega_2 0. \tag{2.10}$$

- The first excited state is the multiplet one phonon state which has two units of angular momenta, it donates a $Y_{2\mu}(\theta, \phi)$ spherical harmonic dependence to the nuclear wave function similar as a $Y_{2m}(\theta, \phi)$ spherical harmonic with $l = 2$.

$$|N = 1, l = 2, m = \hat{\beta}_{l,m}0. \tag{2.11}$$

- The 2nd set of excited states are the quadrupole two phonon $(l + l)$ states with excitation energy $2\hbar\omega_2$ and $m = m_1 + m_2$ now have five possible components link to each phonon which represent ellipsoidal shapes and thus 25 possible combinations of lm are formed for the two vibrational quanta see Table 2.1.

$$|N = 2, lm = \hat{\beta}_{l,lm}0. \tag{2.12}$$

Table 2.1: The combinations of m of the two quadrupole phonons forming a resultant total m component.

	m_1				
m_2	-2	-1	0	1	2
-2	-4	-3	-2	-1	0
-1	-3	-2	-1	0	+1
0	-2	-1	0	+1	+2
1	-1	0	+1	+2	+3
2	0	+1	+2	+3	+4

However by taking symmetric combinations (e.g. for $m = +2$: $(m_1, m_2) = (+2, 0)$, $(+1,+1)$ and $(0,+2)$) of the vibrational quanta's wave functions the 25 possible combinations of lm now reduces to 15 allowed combinations see Table 2.2.

Table 2.2: Final symmetric combinations of the two quadrupole phonons wave functions.

$l =$	4	$m =$	+4	+3	+2	+1	0	-1	-2	-3	-4
$l =$	2	$m =$	+2	+1	0	-1	-2				
$l =$	0	$m =$	0								

Thus a triplet of states having spins $I^+ = 0_2^+$, 2_2^+ and 4_1^+ at two times the first $I^+ = 2_1^+$ state's energy is expected and is indeed observed in vibrational nuclei which validate the simple vibrational model.

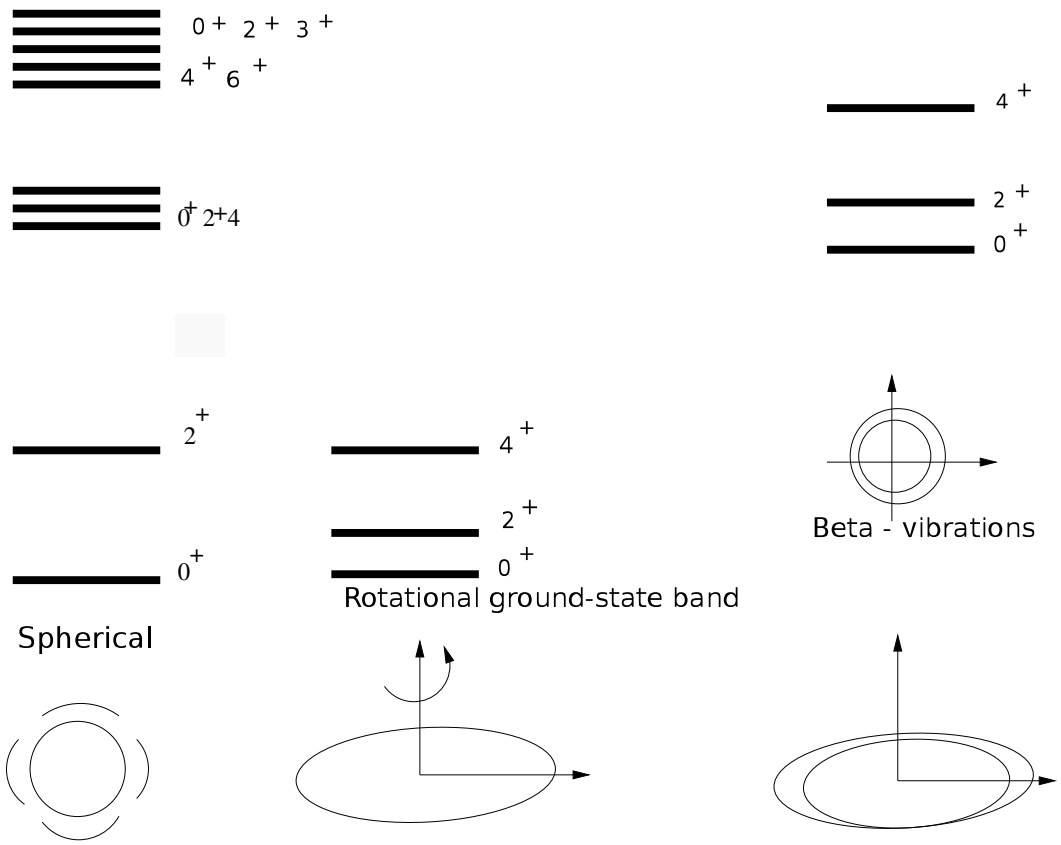

Figure 2.2: The energy spectra for a spheroidal and a deformed nucleus.

2.1.2 Deformed Vibrational Modes

Low-lying $I^\pi = 0_2^+$ spin states can also result from collective shape oscillations along the axis of symmetry in axially deformed even-even nuclei. The most successful account of collective nuclear motion is given by the Bohr and Mottelson Hamiltonian [15], written in equation 2.13 in terms of the polar coordinates (β, γ) and Euler angles θ_I.

$$\hat{H}(\beta, \gamma, \theta_I) = \hat{T}_{vib}(\beta, \gamma) + \hat{T}_{rot/vib}(\beta, \gamma) + V(\beta, \gamma). \tag{2.13}$$

with general solution

$$\hat{H}\Psi^\alpha_{IM}(\beta, \gamma, \theta_I) = E^\alpha_I \Psi^\alpha_{IM}(\beta, \gamma, \theta_I). \tag{2.14}$$

where

$$\Psi^\alpha_{IM}(\beta, \gamma, \theta_I) = \sum_k D^I_{MK}(\theta_I) g^\alpha_k(\beta, \alpha). \tag{2.15}$$

$\sum_k D^I_{MK}(\theta_I)$ is a rotational matrix term, it describes the orientation of the nucleus with respect to the laboratory reference frame and the $g^\alpha_k(\beta, \alpha)$ term denotes the

body-fixed coordinate system. It describes the motion of the nucleons with respect to the intrinsic coordinate system.

The collective Hamiltonian has the following approximate solution:

$$E_{I,K,n\beta,n\gamma} = \frac{\hbar}{2J_0}[I(I+1) - K^2] + (\hbar\omega_\beta n_\beta) + \hbar\omega_\gamma(2n_\gamma + \frac{|K|}{2})[16]. \tag{2.16}$$

- The γ vibrational band is denoted by this $\hbar\omega_\gamma(2n_\gamma + \frac{|K|}{2})$ term.
- The β vibrational band is denoted by this $\hbar\omega_\beta.n_\beta$ term.

with moment of inertia J_0. The quantum numbers I, K and M describe the rotations of the axial symmetric nucleus where M and K are the components of I along the intrinsic symmetry and space fixed (Z) axis respectively (see Fig 2.3).

2.1.3 Ground State Rotational Band

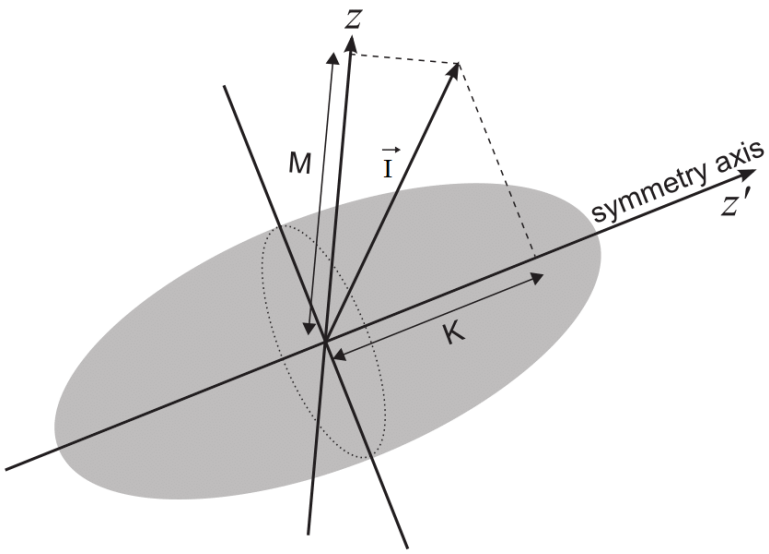

Figure 2.3: An illustration of an axially symmetric nuclear shape. The total angular momentum quantum number I has projection K onto the axis of symmetry and projection M onto the space fixed Z axis [17].

The ground state rotational band energy levels ($E_{I,0,0,0}$) for a deformed even-even nucleus with axial symmetry are described by this relations

$$E_{I,0,0,0} = \frac{\hbar}{2J_0}[I(I+1) - K^2]. \tag{2.17}$$

with the quantum numbers K, n_β, and n_γ all set to zero. Equation 2.17 assumes that the nucleus rotates about an axis perpendicular to the its symmetry axis $Z^{'}$,

generating a sequence of regular spaced energy levels $E_{I,0,0,0}$ with even spin values $I^\pi = 0_1^+$, 2_1^+, 4_1^+ etc which are shown in Fig 2.2.

2.1.4 Gamma Vibrational Band

Gamma vibrational states (see Fig 2.2) are formed from collective surface oscillations that occur perpendicular to the symmetry axis, there are two types of γ-vibrations:

- Lowest energy γ-vibrations for quantum numbers given by ($K = 2$, $n_\beta = 0$, $n_\gamma = 0$) are described by the relation below.

$$E_{I,2,0,0} = \frac{\hbar}{2J_0}[I(I+1) - 4] + \hbar\omega_\gamma. \tag{2.18}$$

- Higher energy γ-vibrations for quantum numbers given by ($K = 0$, $n_\gamma = 1$, $n_\beta = 0$) are described by the relation below.

$$E_{I,0,0,1} = \frac{\hbar^2}{2J_0} I(I+1) + 2\hbar\omega_\gamma. \tag{2.19}$$

2.1.5 Beta Vibrational Band

It corresponds to surface oscillations that occur along the symmetry axis and corresponds to quantum numbers $K = 0$, $n_\beta = 1$, and $n_\gamma = 0$, leading to excited states that are shown in the far right illustration of Figure 2.2. It has a bandhead spin of $I^\pi = 0_2^+$ with energy $E_{I,0,1,0}$ that is calculated from equation 2.20. Note that the spin $I^\pi = 2_2^+$, 4_2^+ etc levels correspond to an adiabatic rotation of the nucleus as a whole.

$$E_{I,0,1,0} = \frac{\hbar^2}{2J_0} I(I+1) + \hbar\omega_\beta \tag{2.20}$$

It has been shown that low-lying $I^\pi = 0_2^+$ spin states can result from collective surface vibrations along the axis of deformation in an axial symmetric nucleus. Further such spin states can also result from small amplitude collective surface oscillations about an equilibrium spherical shape. In conclusion other mechanisms that can also give rise to excited $I^\pi = 0_2^+$ spin states are shape coexistence, 2 phonon excitations (e.g. γ-γ or octupole-octupole modes) multi-quasiparticle excitations and pair excitations amongst others. In the following section the pairing interaction will be discussed.

2.2 Nuclear Pairing

The physics of nuclear pairing can be summarised as follows:

- The ground state of all even even nuclei has spin-parity $I^\pi = 0^+$ due to the pair wise coupling of the nucleons.
- The last term of the Weizsacker mass formula results from proton pairs and neutron pairs forming tendency, which is manifested in the better stability that nuclei with even number of particles have compare to those with odd number particles.
- The odd-even staggering in binding energies [18] can once more be attributed to the stability that nuclei with even number of particles have compare to those with odd number particles.
- The reduced rotational moments of inertia of quadrupole deformed nuclei compared with the rigid rotor values [18] can be explained if it is assumed that the nucleon pairing effect reduces the size of the coherence length with respect to the overall nuclear size. Thus the nucleus would be a superfluid having irrotational flow with a corresponding inertial dynamics.
- The gaps in the excitation spectra of even even deformed nuclei [18] are due to pairing and the first excited states occurs roughly at $E_{ex} \sim 2\Delta_{BCS}$ and are formed by pair breaking.
- The compressed quasi-particle spectra in odd nuclei [15] results from both single particle (last unpaired nucleon) as well as collective core excitations.
- The backbending phenomena in deformed even-even nuclei at A $\sim$ 160 mass region is due to pair breaking of two $i_{13/2}$ orbital neutrons and their subsequent spin alignment along the collective rotational axis.
- Apart from the ground state, excited states within the pairing gap also benefits from the energy gain as a results of pairing correlation. For example under rotation, the energy of the alignable $i_{13/2}$ two-quasineutron configuration is reduced, as a result of the centrifugal force.
- Weakly bound states are described by perturbation theory.
- Scattering results if there are vacancies close to the Fermi surface which requires that the occupation function near the Fermi surface must be smeared out. Thus pairing can result in partial occupancies for orbitals that are close to the occupied orbitals. This give rise to the concept of quasi-particles see section 2.2.3.
- Due to pairing correlations at low excitation energy the nucleon binding energy in nuclei increases see the second bullet.

- Pairing correlations are restricted to paired nucleons in identical time reversed orbitals with their resultant angular momentum coupled to 0.

Apart from the above mentioned pairing phenomena, pairing can also account for the properties of excited $I^\pi = 0^+$ spin states. For example it was postulated by Broglia and Bes [19] that pairing may give rise to so-called *Giant Pairing Vibrations* predicted for heavy nuclei at large excitation energy ($\sim 70\ A^{-1/3}$). It is defined as a correlated two-nucleon (2particle-2particle or 2hole-2hole) mode predicted to occur in the second oscillatory shell above the Fermi surface. The main tool used to search for such states are two nucleon transfer reactions, however these states have never been experimentally detected [20].

In addition the nuclear pairing theory has been developed by a number of authors such as Racah [21] who introduced the seniority concept. This concept was latter used by Jensen and M.Goeppert-Mayer [22] in their shell model to show why even-even nuclei have spin zero, and odd mass nuclei have the spin of the last unpaired particle. In condense matter physics Bardeen, Cooper and Schieffer [23] use the pairing interaction to explain superconductivity in metals. It was postulated by Bohr, Mottelson and Pines that the energy gap found in the excitation spectra of even-even nuclei may be caused by correlation effects similar to those in superconductors, they proposed the BCS theory of nuclear interactions [23]. Belyaev et al., [24] explain pairing properties in complex nuclei, Migdal [25] studied superfluidity and pairing in neutron matter, Kisslinger and Sorensen [26] listed the occupation probability values that are found by the Bogoliubov Valatin transformation. Bardeen, Bogolyubov and Valatin [27] formulated the mathematical basis for solving the many body problem that involve the pairing interaction. Yoshida [28] used the newly formulated BCS pairing theory to account for the enhancement in the ground state two nucleon transfer reaction cross sections of open shell superfluid nuclei.

2.2.1 Nuclear Pairing and Seniority

This concept was originally introduced by Racah [21] for classification of electrons with l^n configuration and having the same spin-orbit quantum numbers. It must be noted that the L-S coupling scheme is the preferred scheme when it comes to atomic electrons, over the jj-coupling scheme. The latter coupling scheme was introduced by Flowers, Racah and Talmi for nuclei [29]. It is based on the idea of pairing of particles into $J = 0$ pairs and represents the earliest attempts to account for the effects of pairing in nuclei; thus the seniority quantum number refers to the number of unpaired nucleons in the j^n configuration.

Starting from the pair creation operator written in occupation number representation as

$$A^\dagger = \frac{1}{\Omega^{1/2}} \sum_{m>0} a^\dagger_{jm} a^\dagger_{-jm} \tag{2.21}$$

Racah showed that the pairing interaction for a j^2 coupled state is given by

$$H = -G\Omega A^{\dagger}A \tag{2.22}$$

and in the case of several j-orbitals the pairing interaction is defined by

$$< (jm)(j-m)|V_{pair}|(j^{'}m^{'})(j^{'}-m^{'}) >= -G\left\{(2j+1)(2j^{'}+1)\right\}^{1/2}\sigma_{J0}\sigma_{M0}$$

where G is the pairing strength, $\Omega = j + 1/2$ is the level degeneracy parameter, j is the angular-momentum and m is the angular-momentum projection on the z-axis quantum number for a single-particle orbital $|jm>$ and $a^{\dagger}_{-jm}$ is the creation operator for the time reversed orbital that is given by $a^{\dagger}_{-jm} = (-1)^{-jm}a_{-jm}$. The pair interaction scatters a pair of nucleons in the states $|jm>$, $|-jm>$ that are coupled to total angular momentum $J{=}0$ to any other $|j^{'}m^{'}>$, $|-j^{'}m^{'}>$ state with constant intensity G, independent of j and m. In addition G is given by

$$G \approx \frac{constant}{A}$$

where the value of the constant factor dependants on the mass region. Thus the pairing interaction allows the pair to switch orbits and thereby mixing $J^{\pi} = 0^+$ states with their final wave function having a mixture of two particles in $|jm>$, $|-jm>$ and two in $|j^{'}m^{'}>$, $|-j^{'}m^{'}>$.

It must be noted that the $J{=}0$ configuration has non vanishing matrix elements or eigenvalue given by

$$E_0 = -G\Omega \tag{2.23}$$

Further when the pair creation operator acts on the pairing interaction an equation is obtained that gives the eigenstates:

$$[HA^{\dagger}] = GA^{\dagger}(\Omega - n) = -G(\Omega - n + 2)A^{\dagger} \tag{2.24}$$

Here n is the number operator

$$n = \sum_{m} a^{\dagger}_{jm}a_{jm} = \sum_{m>0}(a^{\dagger}_{jm}a_{jm} + a^{\dagger}_{j\bar{m}}a_{j\bar{m}}) \tag{2.25}$$

In a semi-magic nucleus the $J = 0$ ground state configuration is assigned seniority $\nu{=}0$ and is derived from the vacuum state ($|0>$) when the pair creator operator $A^{\dagger}$ operates on it, its eigenstate is given by

$$HA^{\dagger}|0 >= -G\Omega A^{\dagger}|0 > \tag{2.26}$$

Adding an additional coupled pair to the vacuum configuration, then the eigenstates becomes

$$H(A^{\dagger})^2|0>= -2G(\Omega-1)(A^{\dagger})^2|0> \tag{2.27}$$

In general for N coupled pair configurations their eigenstates can be found from equation 2.28

$$H,(A^{\dagger})^{N/2}|0>= -\frac{G}{4}N(2\Omega-N+2)(A^{\dagger})^2|0> \tag{2.28}$$

and their eigenvalues can be obtained from equation 2.29

$$E_{\nu=0}(N) = -\frac{G}{4}N(2\Omega-N+2) \tag{2.29}$$

Larger degenerate angular momentum states e.g. *J= 2, 4, 6 ... 2j-1* which are shown in Fig.2.4 can be obtained by breaking up a nucleon pair. Thereby resulting in configurations that have seniority $\nu = 2$. The eigenstate of such configurations can be obtained, if the $(\Omega-1)$ operator $B_J^{\dagger}$ is defined which creates pairs of particles that have resultant angular momentum $J \neq 0$. Here $B_J^{\dagger}$ is denoted by

$$B_J^{\dagger} = \sum_{m>0}(-1)^{j+m}(jj-m|J0)a_m^{\dagger}a_{j\bar{m}} \tag{2.30}$$

and the degenerate eigenstates are found from eq.2.30

$$H(A^{\dagger})B_J^{\dagger}|0>= H|6,4,2,J>= -G(\Omega-2)|6,4,2,J> \tag{2.31}$$

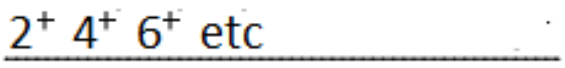

Figure 2.4: It is assumed that the pairing interaction is responsible for the gap between the degenerate *J= 2, 4, 6 ... 2j-1* levels and the J=0 ground state

In general seniority $\nu = 2$ eigenstates for a N particle system is given by

$$H(A^{\dagger})^{(N-2)/2}B_J^{\dagger}|0>= H|N,2,J>= -\frac{G}{4}(N-2)(2\Omega - N)|N,2,J> \quad (2.32)$$

Similarly seniority $\nu = 1$ eigenstates for a N particle system is given by

$$H(A^{\dagger})^{(N-1)/2}B_J^{\dagger}|0>= H|N,1,\gamma>= -\frac{G}{4}(N-2)(2\Omega - N + 1)|N,1,\gamma> \quad (2.33)$$

2.2.1.1 Seniority Shortcomings

- The scheme is limited to a single j-shell in a semi-magic nucleus.
- It is no longer relevant far away from closed shells since nuclei becomes deformed and single particle levels are more or less equally spaced, therefore this model collapsed completely.

2.2.2 BCS Model

It is found that the ground state Hamiltonian operator is easy to use in the BCS approximation and it is much cited in nuclear physics, here $H_{s.p}$ describes the single particle states and H_{pair} denotes the pairing interaction. If the single particle term is diagonalized, the BCS operator can be written in the formalism of the second quantization as

$$H = H_{s.p} + H_{pair} \quad (2.34)$$

$$H = \sum_{j,m} \varepsilon_j a_{jm}^{\dagger} a_{jm} - G \sum_{jj',mm'>0} a_{jm}^{\dagger} a_{j\bar{m}}^{\dagger} a_{j'\bar{m}}, a_{j'\bar{m}'} a_{j'm'}. \quad (2.35)$$

Where ε_j are the single-particle energies for levels j and G is the pairing strength between orbitals j and $j^{'}$. In the monopole pairing approximation, all the two-body matrix elements $G_{jj'}$, are taken to be equal to a single G.

2.2.3 Quasiparticles formalism

For a nucleus in its ground state pairs of nucleons occupying orbitals close to the unoccupied levels can scatter to the "empty" single-particle states. The probability amplitudes for the $|jm>$ orbital being occupied and unoccupied by a pair of particles are V_{jm} and U_{jm} respectively such that

$$V_{jm}^2 + U_{jm}^2 = 1 \quad (2.36)$$

These amplitudes are better known as quasiparticles, a quasiparticle is a mathematical tool invented to avoid the use of interacting particles and their creation operators are calculated via the Bogolyubov-Valatin canonical transforms to be:

$$b_{jm} = U_{jm}a_{jm} - V_{jm}a^\dagger_{-jm} \qquad jm > 0. \quad (2.37)$$
$$b^\dagger_{jm} = U_{jm}a^\dagger_{jm} - V_{jm}a_{-jm} \qquad jm > 0. \quad (2.38)$$

Now the ground state of an even-A nucleus can be described as a quasi-vacuum state $b_{jm}|0>$ provided that the quasiparticle destruction operator b_{jm} acted on the wave function.

$$|BCS>= \prod (U_{jm} + V_{jm}a^\dagger_{jm}a^\dagger_{-jm})|0> \quad (2.39)$$

where $a^\dagger_{jm}a^\dagger_{-jm}$ refers to the pair with single particle orbital jm. This wave function does not contain a fixed particle number, it instead describe a distribution. In condense matter physics the non-conservation of particle number is not of concern since there are Avogadro's number 10^{23} of particles and small variations of the number of particles does not matter. However in nuclei such an approach is not valid and will result in errors since we are dealing with a limited number of particles at most 200. Therefore the number operator $\hat{\mathrm{N}}$ is introduced to the monopole pairing Hamiltonian with a Lagrange multiplier λ which is control by n where n is given by $2\sum_{jm} V^2_{jm}$. The total monopole pairing Hamiltonian is thus expressed by

$$H - \lambda\hat{n} = \sum E_{jm}a^\dagger_{jm}a_{jm} - G\sum a^\dagger_{jm}a^\dagger_{\bar{jm}}a_{\bar{jm}}a_{jm} - \lambda\sum a^\dagger_{jm}a_{jm} \quad (2.40)$$

here E_{jm} are single quasiparticle energies and is given by:

$$E_{jm} = ((\varepsilon_{jm} - \lambda)^2 + \Delta^2)^{1/2} \quad (2.41)$$

Further, λ is now the Fermi surface and Δ is the diffuseness of the Fermi surface. If one assumes that the valence single particle orbitals coincide with the Fermi surface $\varepsilon_{jm} \approx \lambda$ then the energy of a quasiparticle state will be roughly Δ, which accounts for the odd-even staggering in nucleon binding energy. For even even nuclei the lowest excited state is the two-quasiparticle BCS state which is equal to $2E_{jm} \approx 2\Delta$. It can be seen that the energy gap between the ground state and two-quasiparticle state is approximately equal to 2Δ. It must be noted that no intrinsic excitations are expected below the energy gap. In even A nuclei the first intrinsic state has an excitation energy between 1-2 MeV. If there are lower states these are assume to have a collective structure. In the non-degenerate case, the constants U_{jm} and V_{jm} for which the expectation value of $H - \lambda\hat{n}$ is zero are given by

$$U_{jm}^2 = \frac{1}{2}[1 + \frac{\varepsilon_{jm} - \lambda}{\sqrt{(\varepsilon_{jm} - \lambda)^2 + \Delta^2}}] \tag{2.42}$$

$$V_{jm}^2 = \frac{1}{2}[1 - \frac{\varepsilon_{jm} - \lambda}{\sqrt{(\varepsilon_{jm} - \lambda)^2 + \Delta^2}}] \tag{2.43}$$

$$\Delta = G \sum_j U_{jm} V_{jm} \tag{2.44}$$

The monopole (BCS) pairing gap parameter Δ can be estimated from the empirical mass differences between adjacent nuclei with odd and even numbers of nucleons. The even and odd proton pairing gaps maybe written in terms of the odd-even binding energy staggering. The neutron pairing gaps are described by similar notations below.

$$\Delta_{o,Z}(P) = \frac{1}{2}(E_b(Z, P+1) - 2(E_b(Z, P) + (E_b(Z, P-1) \tag{2.45}$$

$$\Delta_{e,Z}(P) = -\frac{1}{2}(E_b(Z, P+1) - 2(E_b(Z, P) + (E_b(Z, P-1) \tag{2.46}$$

2.2.4 Monopole Pairing Correlations

In superfluid spherical nuclei [30–35] the $I^{\pi} = 0_1^+$ ground and pairing vibrational states (see section 2.2) are populated with large two nucleon transfer reaction cross section strengths and are correlated by the monopole pairing interaction. It is written in second quantization notation in equation 3.1, where G_0 is the pair strength parameter and $\bar{i}$ is the time reversal orbital to i. These states result when the single particle energy gap around the Fermi surface is of the same order of magnitude or larger than the corresponding odd-even mass differences. In addition monopole pairing also accounts for the large ground state (p, t) and (t, p) transfer reactions strengths in deformed nuclei for which there is no single particle energy gap around the Fermi surface [36–42]. In contrast their transfer cross sections to I^{π}=0_2^+ spin states are of the order $10^{-2} \times \sigma(gs \rightarrow gs)$ [30, 36, 42].

$$H_{pair}(\lambda = 0) = -G \sum_{jj',mm'>0} a_{jm}^{\dagger} a_{j\bar{m}}^{\dagger} a_{j'\bar{m}}, a_{j'\bar{m}'} a_{j'm^{\bar{}}}. \tag{2.47}$$

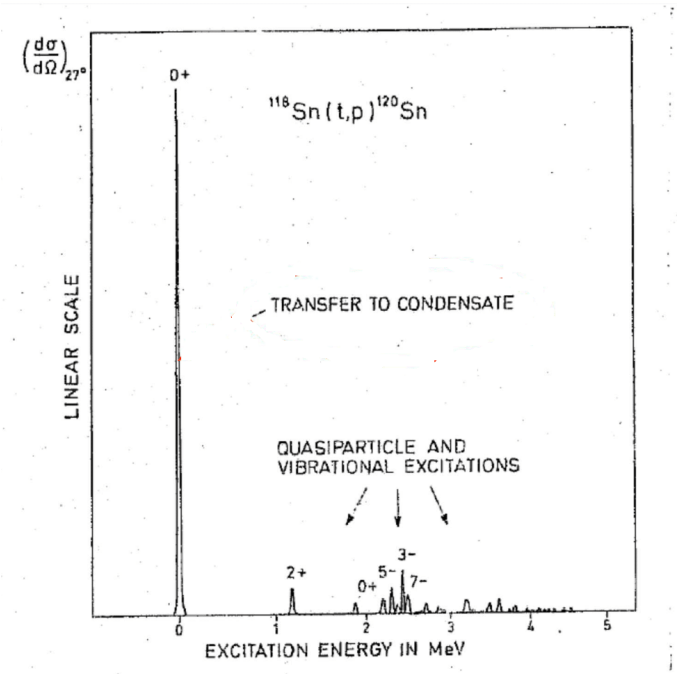

Figure 2.5: The large two neutron stripping reaction cross section to the ground state of ^{120}Sn is correlated by the monopole pairing interaction [30].

2.2.5 Quadrupole Pairing

Evidence for the existence of quadrupole pairing correlations comes from the large two neutron transfer reaction strengths to specific $I^{\pi}= 2_1^+$ spin states for the Pb isotopes [43]. A better description of the rare earths moments of inertia have been obtained by using quadrupole pairing [44]. Quadrupole pairing has also been applied to the actinide region in an attempt to explain the origins of the low-lying $I^{\pi} = 0_2^+$ two quasi-particle states. Figure 3.3 shows the two neutron pick-up reaction spectrum for ^{236}U, it has a pronounced peak at 920 keV which corresponds to the $I^{\pi}= 0_2^+$ spin state [45]. While in Figure 3.4 the same 920 keV peak is missing from the two neutron stripping reaction spectrum [45]. Similar $I^{\pi} = 0_2^+$ spin states were also identified in the excitation spectra of $^{228\text{-}246}$Th , ^{238}U and the ^{242,244}Pu isotopes [46].

Actinides $I^{\pi}= 0_2^+$ spin state properties

1. They appear inside the normal pairing gap and display large asymmetries in their two neutron pick-up (p, t) and two neutron stripping reaction (t,p) population strengths.

2. They are weakly populated in Coulomb, inelastic and single nucleon transfer reactions and have weak B(E2, $0_2^+ \rightarrow 2_1^+$) and B(E0, $0_2^+ \rightarrow 0_1^+$) reduced transition probability strengths to the ground state band.

3. They are based on steep upsloping oblate high-Ω Nilsson levels that are extruded to the Fermi surface by the quadrupole deformation.

The above listed properties do not correspond to those of a pair vibrator, β-vibrator, shape coexistence, 2 phonon or multi-quasiparticle excitations [46].

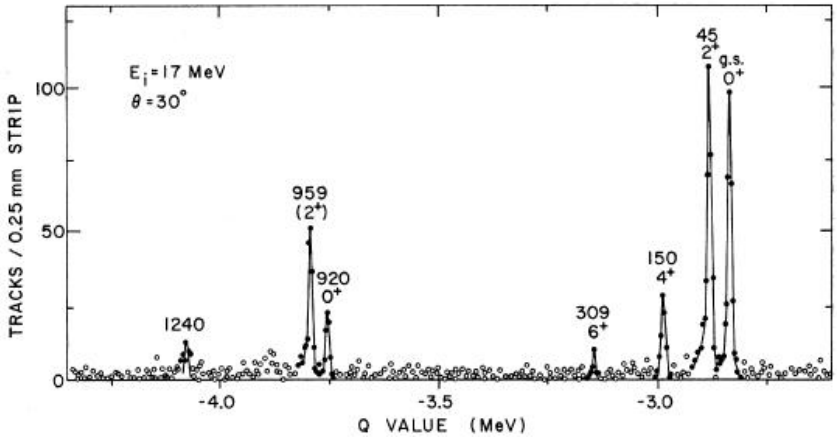

Figure 2.6: In the two neutron pick-up ^{238}U(p,t)^{236}U spectrum. The pairing isomeric spin state is populated by the 920 keV peak [45].

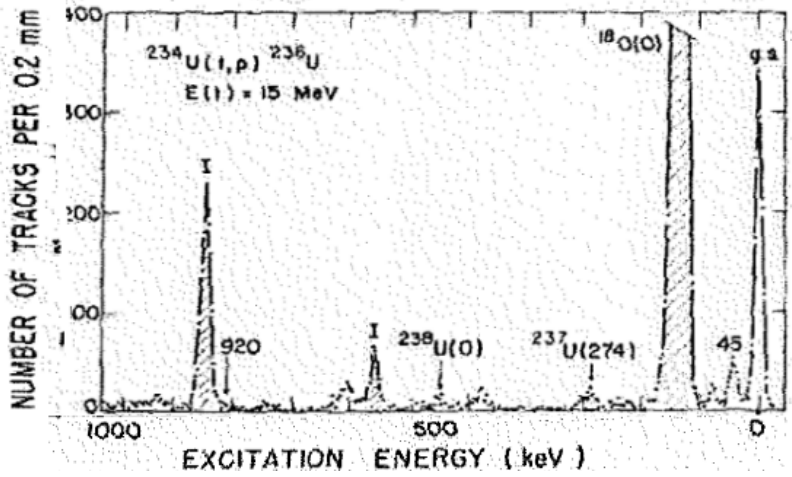

Figure 2.7: In the two neutron stripping reaction ^{234}U(t,p)^{236}U spectrum the pairing isomeric spin state at 920 keV excitation energy was not populated [46] and reference theirein.

Explaining the $I^\pi = 0_2^+$ spin state in the Actinides

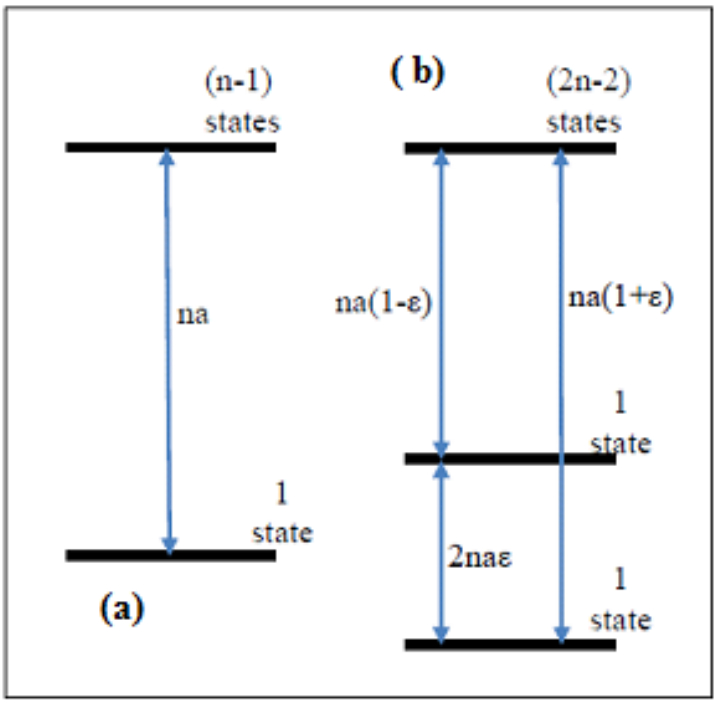

Figure 2.8: (a) Depicts the monopole pairing correlations with one state lowered below all the others. While (b) depicts quadrupole pairing correlations with the oblate-prolate pairing strength G_{op} weakened by $\varepsilon << 1$ [47].

Griffin, Jackson and Volkov [47] suggested that the properties of the low-lying $I^\pi = 0_2^+$ spin states found in the actinide nuclei can be accounted for by using configuration dependent pairing which arises as a result of weaknesses in the oblate prolate pair scattering matrix element compared to the matrix elements that connects only prolate or only oblate orbitals. They illustrated this by considering a toy model in which there are n prolate and n oblate degenerate levels at the Fermi surface. Prolate orbitals are near the equatorial plane with respect to the rotational axis, they have small magnetic quantum numbers m, a positive quadrupole moment and have down-sloping trajectories on the prolate side of the Nilsson diagram. Oblate orbitals are near polar planes passing through the rotational axis, have large m values and are associated with up-sloping trajectories on the prolate side of the Nilsson diagram. Assume that each pairing matrix element is the same -a for the same type, prolate-prolate or oblate-oblate, but the prolate-oblate matrix elements are very weak -εa. Then if the prolate $n * n$ matrix is A, the oblate matrix is also A and the matrix for the total system is;

$$\begin{bmatrix} A & \varepsilon a \\ \varepsilon a & A \end{bmatrix} \tag{2.48}$$

This matrix has (2n-2) eigenvalues with zero energy and two eigenvalues with energies $E_{1,2}$ = -(1 $\pm$ εna) and an energy separation between the two lowered states ΔE = 2 εna which is shown in Fig.3.5(b).

Mathematical Formulation

The ideas of Griffin, Jackson and Volkov [47] were put on a firm mathematical bases by Ragnarsson and Broglia by using the BCS and RPA methods [48]. Starting from the BCS equation the ground state of a deformed nucleus can be obtained from the total Hamiltonian.

$$H_T = \{\mathrm{H}_{s.p} + H(20) + H(22) + H(02)\} \tag{2.49}$$

where $H_{s.p}$ is the single particle Hamiltonian given by

$$H_{s.p} = \sum_i \varepsilon_i (c_i^+ c_i + c_{\bar{i}} c_i) \tag{2.50}$$

The multipole pairing Hamiltonian H(20) + H(22) is defined as

$$H(2\lambda) = -G_\lambda P_\lambda^+ P_\lambda \tag{2.51}$$

where P_λ^+ is the multipole pair creation operator and λ is the multipole order index.

$$P_\lambda^+ = -\sum_i Q_i^\lambda c_i^+ c_i \tag{2.52}$$

and Q_i^λ is the intrinsic quadrupole moment of the Nilsson single particle orbital i and is describe by

$$Q_i^\lambda = < i|r^\lambda Y_{\lambda 0}|i > \tag{2.53}$$

Further, it is assumed that $G_0 \approx G_2$ for a surface delta force with constant surface amplitude. One can rewrite the multipole pairing Hamiltonian in terms of quasi particles by plugging in the Bogoliubov quasi-particle transformation

$$c_i^+ = U_i d_i^+ + V_i d_{\bar{i}} \tag{2.54}$$

$$c_{\bar{i}}^+ = U_i d_{\bar{i}}^+ - V_i d_i \tag{2.55}$$

and the normalization condition

$$U_i^2 + V_i^2 = 1 \tag{2.56}$$

into the pairing Hamiltonian H_p.

$$H_p = \sum_i (\varepsilon_i - \lambda)(c_i^+ c_i + c_{\bar{i}} c_i) - G_\lambda P_\lambda^+ P_\lambda \tag{2.57}$$

where c^+c is the deformed single particle orbital with energy ε_i, λ is the Fermi level, G_λ are the multipole pairing strengths parameters and d_i^+ creates a quasi-particle in a Nilsson orbitals.

It follows that the pairing operator P_λ^+ can now be written in terms of a Hermitian quasi-particle operator

$$P_\lambda^+ = -\sum_j Q_j^\lambda U_i V_j (1 - n_i) + \sum_j (\sqrt{\frac{n}{2}} P_j^\lambda X_i + i\sqrt{\frac{1}{2}} Q_i^\mu \prod_j) \tag{2.58}$$

where

$$n_j = d_j^+ d_{\bar{j}}^+ + d_{\bar{j}}^+ d_j^+ = n_j^+ \tag{2.59}$$

$$X_j = \sqrt{\frac{1}{2}} (d_j^+ d_{\bar{j}}^+ + d_{\bar{j}}^+ d_j^+) = X_j^+ \tag{2.60}$$

$$\prod_j = i\sqrt{\frac{1}{2}} (d_j^+ d_{\bar{j}}^+ - d_{\bar{j}}^+ d_j^+) = \prod_j^+ \tag{2.61}$$

$$p_j^{(\lambda)} = Q_j^{(\lambda)} (U_j^2 - V_j^2) \tag{2.62}$$

and the pair interaction Hamiltonian becomes now

$$H_p = U + H_{11} + H_{20} + H_{40} + H_{31} + H_{22} \tag{2.63}$$

where

$$U = 2\sum_i V_i^2 (\varepsilon_i - \lambda) - \sum_\lambda [\frac{\Delta_\lambda^2}{G_\lambda} - G_\lambda \sum_i (Q_i^\lambda)^2 V_i^4] \tag{2.64}$$

$$H_{11} = 2\sum_i [(\varepsilon_i^{'} - \lambda)(U_i^2 - V_i^2) + 2\sum_\lambda (\Delta_\lambda Q_i^\lambda U_i V_i)] n_i \tag{2.65}$$

$$H_{20} = \sum_i [(\varepsilon_i^{'} - \lambda) 2U_i V_i - \sum_\lambda \Delta_\lambda p_i^\lambda] (d_i^+ d_{\bar{i}}^+ + d_{\bar{i}} d_i) \tag{2.66}$$

Assuming the quasi-particle approximation is a good approximation then the lower excited states will have only a few quasi particles. Neglecting the terms H_{40} + H_{31} +H_{22} and setting H_{20}=0 and using the normalization condition we then get

$$U_i = \sqrt{\frac{1}{2}(1 + (\varepsilon_i^{'} - \lambda)/E_i)^{1/2}} \tag{2.67}$$

$$V_i = \sqrt{\frac{1}{2}(1 - (\varepsilon_i^{'} - \lambda)/E_i)^{1/2}} \tag{2.68}$$

Here E_i is the quasi-particle energy and is given by

$$E_i = \sqrt{(\varepsilon_i^{'} - \lambda)^2 + \Delta_i^2} \tag{2.69}$$

Δ_i is the state dependent pairing gap

$$\Delta_i = \Delta_0 + \sum_\lambda Q_i^{(\lambda)} \Delta_\lambda \tag{2.70}$$

and Δ_λ is the multipole pairing gap.

$$\Delta_\lambda = G_\lambda \sum_i Q_i^{(\lambda)} U_i V_i \tag{2.71}$$

Substituting U_i and V_i into (34) we then arrive at the two equations

$$\Delta_0 (\frac{2}{G_0} - \sum_i \frac{1}{E_i}) = \Delta_2 (\sum_i \frac{Q_i}{E_i})^2 \tag{2.72}$$

$$(\frac{2}{G_0} - \sum_i \frac{1}{E_i})(\frac{2}{G_2} - \sum_i \frac{Q_i^2}{E_i}) = (\sum_i \frac{Q_i}{E_i}) \tag{2.73}$$

From the particle number constraint we get the third equation

$$n = 2 \sum_i V_i^2 = \sum_i (1 - \frac{\varepsilon_i - \lambda}{E_i}) \tag{2.74}$$

In these equation the unknowns are the monopole (Δ_0) and quadrupole (Δ_2) pairing gaps

$$\Delta_0 = G_0 \sum_i (U_i V_i) \tag{2.75}$$

$$\Delta_2 = G_2 \sum_i (Q_i U_i V_i) \tag{2.76}$$

Lastly an expression for the BCS ground state can be obtained

$$|0> = \prod (U_i + V_i c_i^\dagger c_{\bar{i}}^\dagger) |\nu>$$

where ν is the single particle vacuum state with energy

$$W = 2\sum_i V_i^2 c_i - G_0[\sum_i V_i^4 - (\sum_i U_i V_i)^2] - G_2[\sum_i Q_j^2 V_i^4 - (\sum_i Q_i U_i V_i)^2]$$

The pair correlation energy is then given by

$$\sigma W = W - W_{diagonal}$$

where

$$W_{diagonal} = 2\sum_i \varepsilon_i - \sum_i (G_0 + G_2 Q_i^2)$$

2.2.6 Pair Isomers

The matrix element of the pairing interaction that acts among the valence particles in the case of a quadrupole deformed nucleus is given by

$$G = < i\bar{i}|H(20) + H(22)|j\bar{j} > -G_0 - G_2 Q_i Q_j$$

One can thus identify two different types of pairing matrix elements those that are related between pairs of single particle orbitals that display the same sign of the quadrupole moment. Here we refer to the scattering between the bunch of prolate levels around the Fermi surface

$$G_{pp} = < i_p\bar{i_p}|H(20) + H(22)|i_p^{'}\bar{i_p}^{'} > G_0 - G_2 Q_i(p) Q_{i'}(p) \tag{2.77}$$

and the scattering of a pair of particles among oblate single particle orbitals that are found below the Fermi surface

$$G_{oo} = < i_o\bar{i_o}|H(20) + H(22)|i_o^{'}\bar{i_o}^{'} > G_0 + G_2 Q_i(o) Q_{i'}(o) \tag{2.78}$$

and pair scattering between oblate and prolate pairs of orbitals with opposite sign of the quadrupole moment.

$$G_{op} = < i_o\bar{i_p}|H(20) + H(22)|i_o^{'}\bar{i_p}^{'} > G_0 - G_2 Q_i(o) Q_{i'}(p) \tag{2.79}$$

In the model of van Rij and Kahana [49] the suggestions of Griffin, Jackson and Volkov [47] were used to explain how monopole plus quadrupole pair correlations results in the formation of low lying non-collective $I^{\pi} = 0_2^+$ spin states in the actinide region. Their arguments were based on the small B(E2:$0_2^+ \rightarrow 2_1^+$) and on the small $\rho(E0,0_2^+ \rightarrow 0_1^+)$ reduced transition probabilities values as well as on the orbitals located around the Fermi surface. The neutron single particle level

distribution of Fig.3.6 is similar to those levels that are found around the Fermi surfaces in the actinides.

In the schematic the levels around the Fermi surface are prolate while (0.5 - 1) MeV below the Fermi surface there is a small group of oblate levels. In this case the $I^\pi = 0_1^+$ ground state will be built from the downsloping prolate orbitals since these levels have large pair scattering amplitudes ($G_{pp}/\Delta\varepsilon_{pp}$), because they are closely spaced ($G_{pp} << \Delta\varepsilon_{pp}$). Oblate levels have a similar pair scattering amplitude. While the oblate-prolate levels have a smaller pair scattering amplitude value, which results from the large average spacings $\Delta\varepsilon_{op} >> G_{op}$ between oblate-prolate levels. It follows thus that $|G_{pp}| \approx |G_{oo}| >> |G_{op}|$ because of the weaknesses in the $|G_{op}|$ pair matrix elements one observes a dynamic decoupling of the single particle levels.

Consequently one can expects an additional $I^\pi = 0^+$ spin state whose main component corresponds to a scattered neutron pair that moves in an oblate level, that is extruded to the Fermi surface by the nuclear deformation. The oblate state exist inside the normal pairing gap because it has a small quasi-particle energy $E_i = \sqrt{(\varepsilon - \lambda)^2 + \Delta_i^2}$ which results from the small average values of the Δ_i's of the oblate levels below the Fermi surface. The (p, t) cross section is large because the DWBA $(\frac{d\sigma}{d\Omega})^0$ cross section contain the two nucleon transfer amplitude which contain the parentage factor $\beta_{\gamma LSJ}$ or Yoshida's spectroscopic factor term $B(J, j_1 j_2)$. This term accounts for the pairing correlations and is responsible for the two nucleon transfer reaction cross section enhancement [28].

Further, the (p, t) cross section for the $I^\pi = 0_2^+$ spin state is proportional to $V^2 \approx 1$ and is given by

$$\delta^{(p,t)}(g.s \rightarrow 0_2^+) \approx ((\frac{d\sigma}{d\Omega})^0 b_i^n V^2)^2 \approx 1$$

while its (t, p) cross section is proportional to $U^2 \approx 0$ (oblate levels fully occupied) and is given by

$$\delta^{(t,p)}(g.s \rightarrow 0_2^+) \approx ((\frac{d\sigma}{d\Omega})^0 b_i^n U^2)^2 \approx 0$$

Finally pairing isomers are not only limited to the actinide region, but have also been found in the rare earth isotopes of ^{154}Gd [50] and ^{152}Sm [51]. It is because these nuclei have their neutron Fermi surfaces near the upsloping oblate high-Ω Nilsson $\nu[505]\ 11/2^-$ level. In addition they have a lower density of oblate Nilsson levels compare to the density of prolate levels, meaning the oblate-prolate pair matrix elements G_{op} will be weaker than the prolate-prolate G_{pp} or oblate-oblate pair matrix elements G_{oo}.

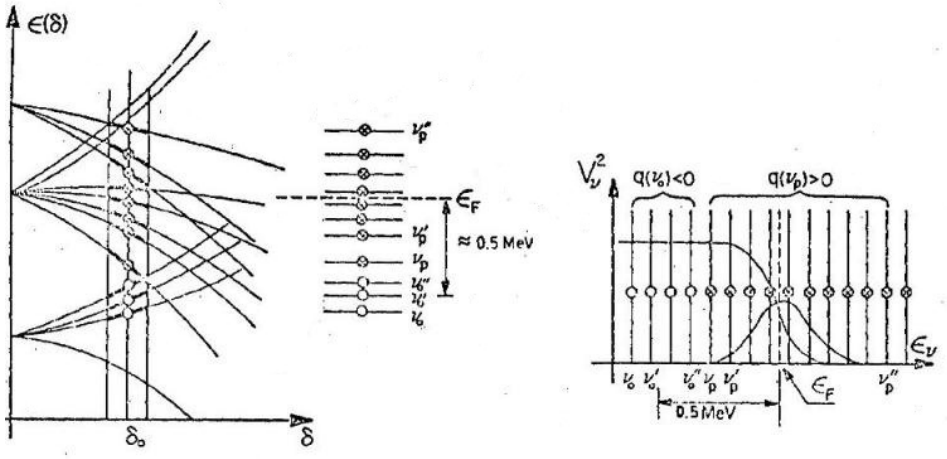

Figure 2.9: Simplified distribution of possible prolate and oblate levels around the Fermi surface of the actinides isotopes drawn against the quadrupole deformation, with the occupation probability on the rigth [48].

Chapter 3

Nuclear Models and Simulations

3.1 Overview

In this chapter the statiscal model will be discussed. Followed by the PACE4 [52], the HIVAP [53] and the CACARIZO [54, 55] statistical model codes. These codes were used to estimate the strengths of the evaporation channels in particular the 1n exit channels that lead to ^{150}Sm and ^{100}Ru. Further each code implement the statistical model differently.

This is followed by the FRESCO as well as the GOSIA Coupled Channels multistep reaction calculations [56, 57]. The CCBA calculations were performed to verify if the observed large relative strengths of the yrast spin states are not the result of a multistep reaction mechanism. It has been suggested that the incoming ^{3}He projectile could Coulomb or inelastically excite the ^{98}Mo and ^{148}Nd target nuclei, to their respective yrast $I^{\pi} = 2_1^+$, 4_1^+, 6_1^+ and 8_1^+ spin states and then have direct two proton $L = 0$ transfer taking place [58], populating the yrast transitions that are seen in the γ-ray spectra of Figure 7.09 and Figure 7.10.

Shell model calculations were also performed with the NuShellX code [59]. Lastly Monte-Carlo simulations were carried out with the GEANT4 [60] toolkit to determine the response of the NE102A plastic scintillator detectors upon the detection of fusion evaporation neutrons in particular those that originate from the 1n exit channels of the compound ^{101*}Ru and ^{151*}Sm nuclei.

3.2 Statistical Model

The first attempt to explain the nuclear decay process must be credited to Niels Bohr [61], his idea is today known as the independence hypothesis and it is summarised in relation 3.1. The core of this hypothesis is the formation of a compound nucleus (CN) C^*, which started off as a target nucleus A that is bombarded by

an incident particle *a*. The deposited energy is distributed statistically among many complicated configurations, similar to the case when a body is heated. The compound system is short-lived macroscopically, but survives long enough on a nuclear time scale 10^{-20} to 10^{-15}seconds to reached thermal equilibruim.

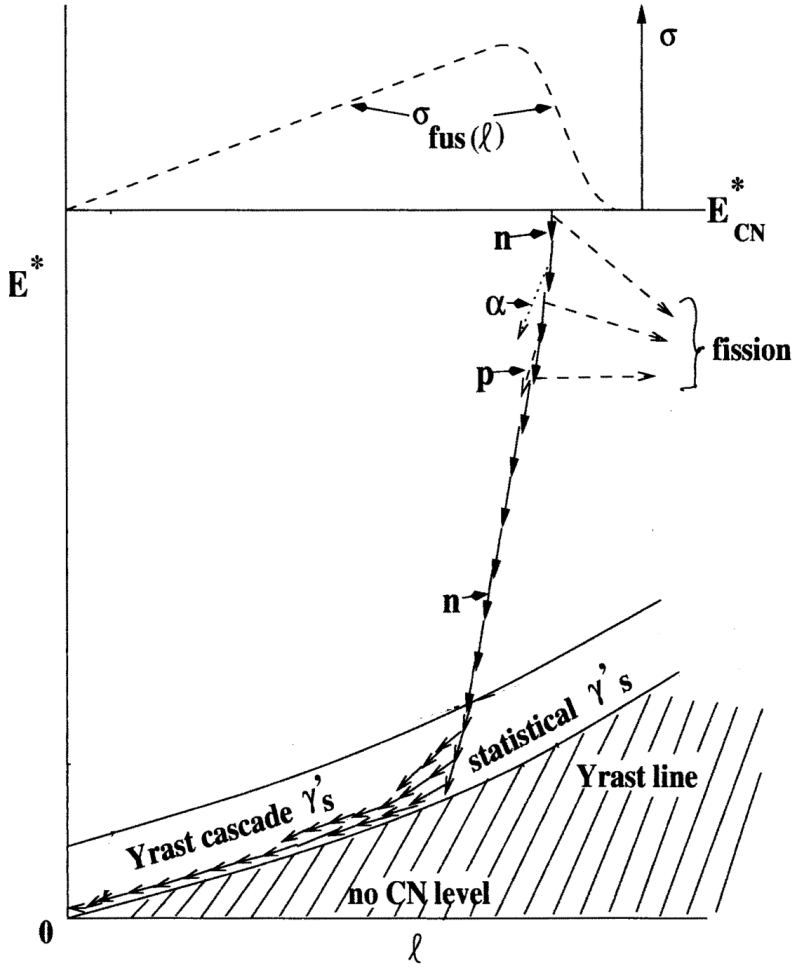

Figure 3.1: The schematic depicts the compound nucleus formation probability distribution $\sigma_{fus(l)}$ as a function of excitation energy and critical angular momentum l_{cr}. It then decays via various particle emission processes to form a bound residual nucleus which further deacay via γ-emissions [62, 63].

Once formed the compound nucleus lost all memory of its initial parts, apart from its isospin T, its angular momentum l, its parity π and excitation energy E_C^*. It decays by emitting particles b (neutrons, protons and or α's) due to statistical fluctuations, for significantly large excitation energy these emissions may be followed by the compound nucleus undergoing fission. Thereafter a bound residual nucleus often in an excited state B results. That decays in most cases to the ground state via γ-ray transitions.

$$a + A \rightarrow C^* \rightarrow B + b. \tag{3.1}$$

The cross section associated with relation 3.1 can be rewritten as

$$\sigma(a + A \rightarrow B + b) = \sigma(a + A \rightarrow C^*)P(C^* \rightarrow B + b) = \sigma(a + A \rightarrow C^*)\frac{\Gamma_{C^* \rightarrow B+b}}{\Gamma} \tag{3.2}$$

where the $\sigma(a + A \rightarrow C^*)$ term is the compound nucleus formation cross section, the $P(C^* \rightarrow B + b)$ term is the probability that the compound nucleus will decay into channel $B + b$ which can also be rewritten as the ratio of the partial width $\Gamma_{C^* \rightarrow B+b}$ to the total width Γ. The total width can also be expressed in terms of the half-life of disintegration $\tau = \frac{\hbar}{\Gamma}$ of the compound nucleus.

The basic assumption of Bohr's model stipulates that compound nucleus decay is independent and all possibilities for decays are possible. For a compound nucleus with zero spin, if it is energetically allowed nucleons will first be isotropically emitted. Meaning any angle θ_{com} is equally probable and among the nucleons depending on Z it is usually the neutrons that will come first having energy distribution that is best describe by Maxwell-Boltzmann statistics see equation 3.3 [64]. This happens because the Coulomb barrier prevents the release of charged particles from the compound nucleus for low center-of-mass energies see Fig.3.2.

$$I(E) \propto E \exp\left(\frac{-E}{\theta}\right) dE. \tag{3.3}$$

where *I(E)* indicates the amount of neutrons that are emitted with energy between E and $E + dE$. The parameter θ, with units of energy, has the role of a nuclear temperature. It is related to the level density ρ(E) term of the daughter nucleus B by:

$$\frac{1}{T} = \frac{dS(E)}{dE} \tag{3.4}$$

with

$$S(E) = ln\rho(E) \tag{3.5}$$

$$\rho(E) \propto e^{2\sqrt{aE}}. \tag{3.6}$$

where S(E) is the nuclear entropy term, the dS(E)$/dE$ term is calculated at the limit of emission of a neutron with zero kinetic energy and the parameter a is known as the level density parameter. The level density specifies the number of different ways in which individual nucleons can be placed in the various single particle orbitals such that the excitation energy lies in the range E to E+dE. For nuclei located far away from close shells a changes linearly with mass number A here k is estimated to range between $k \simeq 7.5 - 8$ [65].

$$a \simeq \frac{A}{k} MeV^{-1}. \tag{3.7}$$

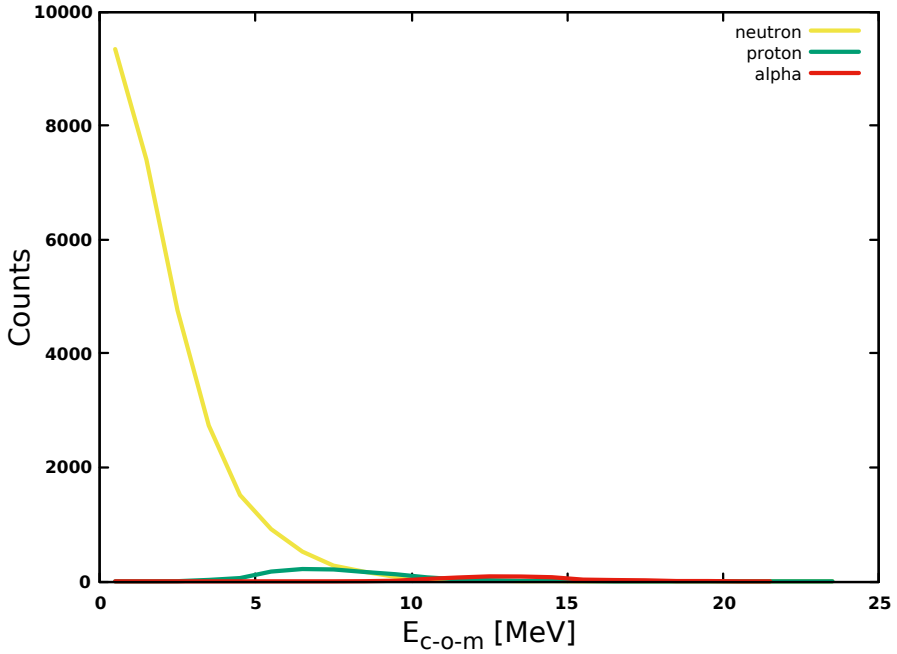

Figure 3.2: The evaporated particle yields are trended against their centre-of-mass energies, these were extracted from the CACARIZZO results for the ^{101*}Ru compound nucleus. Due to the Coulomb barrier the average kinetic energies of the protons and α-particles are larger compare to those from the neutrons.

In conclusion the independence hypothesis forms the basis of several advance statistical models for compound nuclear decay i.e. the Weisskopf stastical model which was develop by H.A. Bethe [66], L.D. Landau [67] and V.F. Weisskopf [68]. One major weak point of this theory is the lack of angular momentum and parity inclusions. Therefore it was superseded by the quantum mechanical Hauser-Feshbach approach [69], which includes angular momentum and parity terms in the compound nucleus partial reaction cross section $\sigma_b(E, I, \Pi)$ description. The latter cross section can be obtained by starting with the incidence channel a and ending with the exit channel b for a given orbital angular momentum l

$$\sigma_b(E, I, \Pi) = \sigma_a(E, I, \Pi)\frac{\Gamma_b(E, I, \Pi)}{\sum_n \Gamma_n(E, I, \Pi)}. \tag{3.8}$$

where E, I and Π are the excitation energy, the total angular momentum and parity of the compound nucleus respectively. The index n represents the possible decay channels, Γ_n denotes the particle decay width and σ_a is the compound nucleus formation cross section. This quantity is expressed in terms of the transmission coefficients $T_l^a(\epsilon)$:

$$\sigma_a(E, I, \Pi) = \frac{\pi}{k^2}\frac{2I+1}{(2l+1)(2i+1)}\sum_{S=|l-i|}^{l+i}\sum_{l=|I-S|}^{I+S} f(l, \Pi)T_l^a(\epsilon). \tag{3.9}$$

where k is the projectile (target) relative motion wave number, $(i,\ l)$ is the projectile (target) spin, l is the projectile orbital angular momentum, S is the channel spin, ϵ is the projectile energy, $\epsilon + B_a = E$, $_a$ is the projectile binding energy and the $f(l,\ \Pi)$ quantity accounts for parity conservation.

The final cross section σ_{ab} is obtained by integrating all the partial cross sections that are connected with all the levels $(I,\ \Pi)$ of the compound nucleus:

$$\sigma_{ab}(E) = \sum_{I,\Pi} \sigma_b(E, I, \Pi). \tag{3.10}$$

Lastly the particle decay width Γ_n of the compound nucleus state (E, I, Π) from where particle b is emitted is given by:

$$\Gamma_b(E, I, \Pi) = \frac{1}{2\pi\rho(E, I, \Pi)} \sum_{I'=0} \sum_{\Pi'} \sum_{j=I-I'}^{I+I'} \int_0^{E-B_b} \rho(E', I', \Pi') T_b^{l,j}(E - B_b - E')dE. \tag{3.11}$$

where B_b is the binding energy of the emitted particle b, $\rho(E', I', \Pi')$ is the level density in the compound nucleus and $T_b^{l,j}(\epsilon')$ is the transmission coefficients of particle b having channel energy $\epsilon = E - B_b - E'$ and orbital angular momentum l where E' represents the excitation of the bound residual nucleus.

3.2.1 The PACE4 code

The Monte-Carlo PACE4 (Projection Angular momentum Coupled Evaporation) code was initially developed by Gavron [52], to predict partial cross sections for the competing fusion evaporation reaction channels, that resulted from the compound nucleus de-excitation stage. PACE4 originates from the JULIAN - the Hillman-Eyal evaporation code [52]. The code performs only statistical equilibrium calculations and does not take into account the pre-equilibrium emission. It produces the angular distribution of the emitted particles or residues in the laboratory frame and most of the nuclear parameters like reaction Q-values, optical model parameters, interaction barriers and level densities are predefined and may also be manually entered. The level density is derived from the Fermi gas model but the beam energy, projectile (target) mass and charge as well as the number of simulated events must be specified. For any specific bombarding energy, the partial cross section $\sigma_{l_{cr}}$ for compound nucleus formation at a given critical angular momentum l_{cr} (the amount of angular momentum required for compound nucleus formation) is given by

$$\sigma_{l_{cr}} = \frac{\lambda^2}{4\pi}(2l + 1)T_l \tag{3.12}$$

where $\lambda = \frac{\hbar^2}{2\mu E}$ is the reduced wavelength of the incident channel in the center of mass system, and T_l is the transmission coefficient which is derived from the Fermi

gas distribution model

$$T_l = [1 + exp(l - l_{cr})/\delta)]^{-1} \tag{3.13}$$

where δ is the diffuseness parameter and l_{cr} is determined from the compound nucleus formation cross section σ_{cn} which is denoted by

$$\sigma_{cn} = \sum_{l=0}^{\infty} \sigma_{l_{cr}}. \tag{3.14}$$

In Fig 3.3 the ^{101*}Ru and ^{151*}Sm compound nuclei partial cross section distributions as functions of their angular momenta are shown. From these plots the critical angular momenta l_{cr} for both compound nuclei and their intergrated cross sections which are listed in Table 3.1 were obtained. The calculations were performed with default optical model parameters and were run for a million events. It was not possible to directly compare the calculated results with those from the measurements, since measured cross sections were not extracted. The best approach was to compare the cross section ratios for the 1n/3n exit channels from the statistical model calculations and experimental data. The latter were obtained by extracting the relative strengths for the $I^{\pi} = 2_1^+$ and 4_1^+ spin states from the total projection spectra.

It is found that the PACE4 results deviates from the measured strengths see Table 5.2.

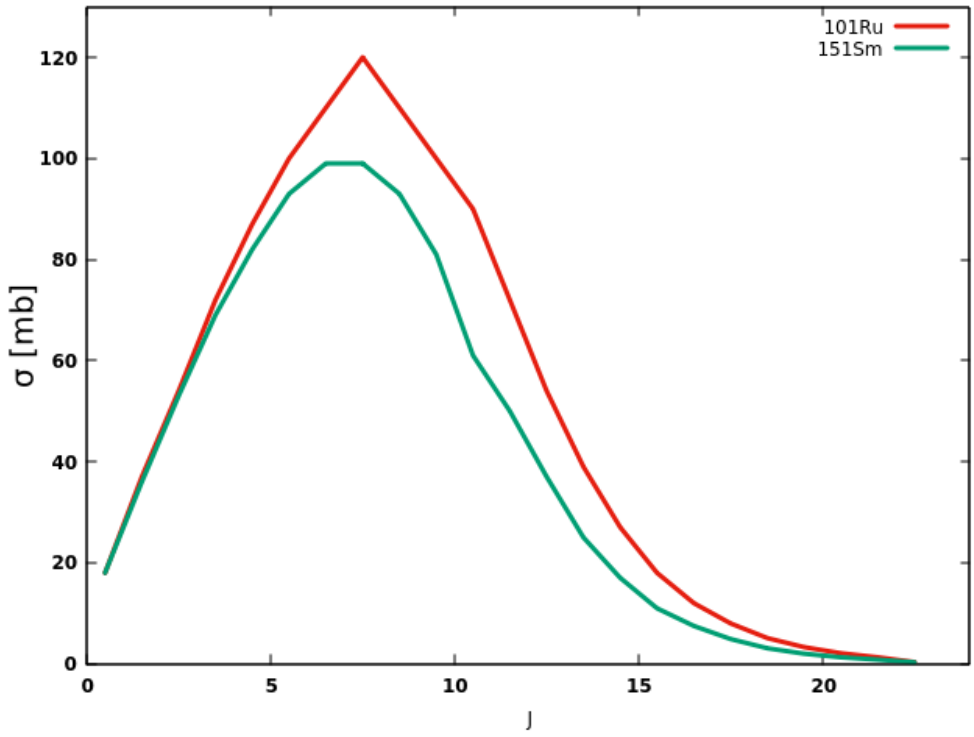

Figure 3.3: The ^{101*}Ru and ^{151*}Sm compound nuclei partial cross sections are plotted as functions of their angular momenta. Again due to the influence of the Coulomb barrier the ^{101*}Ru cross sections are larger than those of ^{151*}Sm, starting from spin $2.5\hbar$ to $23.5\hbar$.

3.2.2 The HIVAP code

The Heavy Ion VaP code is a very fast analytical program. It is based on the GROGI code [53] which was modified by W. Reisdorf [53]. The code follows the statistical Hauser-Feshbach approach and is primarily used to calculate the reaction cross sections of heavy and super heavy elements. It differs remarkably from its predecessor because it is assumed that the evaporation residue formation proceeds via the complete fusion of the projectile and target nuclei to form a compound nucleus, which decay via the competition between nuclear fission, particle evaporation, and γ-ray decay. Further, the code follows a new approach to calculate the level densities, the nuclear masses, the interaction barriers, the fission barriers, transmission coefficients and shell effects amongst others. Consult Ref.[70] for a comprehensive description of the code.

This code predicts similiar results as those given by PACE4 see Table 3.2.

3.2.3 The CACARIZO code

CACARIZO [54, 55] is a statistical evaporation simulation program which describes the de-excitation process of an excited nucleus in terms of the Hauser-Feshbach formalism. This code is a Monte-Carlo version of CASCADE [54], which assumes that the reaction begins with an initial state and ends with a final state. Starting with the formation of a compound nucleus and ending with the statistical decays of the equilibrated system via light particle and γ-ray emissions. The particle emissions are approximated in terms of semi classical angular distributions and include kinematical effects and are calculated in the center-of-mass reference frame.

The partial cross section $\sigma(I,\pi)$ for compound nucleus formation can be expressed as a function of the spin I, the parity π, the target spin I_T, the projectile spin I_p, the center of mass energy E, the transmission coefficients $T_l(E)$, the orbital angular momentum L and the channel spin S $= |I_p + I_T|$.

$$\sigma(I,\pi) = \frac{\lambda^2}{4\pi}\frac{(2I+1)}{(2I_p+1)(2I_T+1)}\sum_{|I_P-I_T|}^{|S=_P+I_T|}\sum_{|I+S|}^{L=|I-S|} T_l(E). \tag{3.15}$$

The total fusion cross section σ_{l_c} for the critical angular momentum l_c of the compound nucleus is given by

$$\sigma_{l_c} = \pi\lambda^2\sum_{L=0}^{l_c}(2l+1)T_l(E) \tag{3.16}$$

where the transmission coefficient T_l(E) is approximated from the Fermi gas distribution expression for a given angular momentum and energy:

$$T_l(E) = \frac{1}{1 + \exp[(l - l_0)/\Delta L]} \tag{3.17}$$

here l_0 is the grazing angular momentum and ΔL is the diffuseness coefficient. The transmission coefficients can be calculated by using appropriate optical model potentials. The need for such a coefficient arises due to the complicated interactions of the nucleons in the target nucleus with the incident particles in the projectile. The nuclear many-body problem can be approximated by a two-body problem assuming all the interactions can be describe by a simple potential *U(r)* that exists between the nucleus and the incident particles. This simplistic potential *U(r)* can be equated to a glass ball where the projectile and target nucleus are beams of light interacting with the glass ball. This glass ball is imagined to be somewhat murky to reproduced the occurrence of elastic scattering and absorption in the interaction.

$$U(r) = V(r)f_R(r) + iW(r)f_I(r) \tag{3.18}$$

here V(r) and iW(r) are terms that describes the real (elastic scattering) and imaginary (absorption) depths of the potentials, $f_R(r)$ and $f_I(r)$ are their radial form factor terms given by the Wood - Saxon potentials and is denoted by:

$$f_{R,I}(r) = [1 + exp(\frac{r - R_{R,I}}{a_{R,I}})]^{-1} \tag{3.19}$$

where R_R, R_I are radii and a_R, a_I are the surface diffuseness terms. The transmission coefficients can now be express in terms of such parameters, see Ref.[71].

$$T_l = \frac{-8}{\nu\hbar}\int_0^\infty dr|y_l(r)|^2 W(r) = 1 - |S_l|^2 \tag{3.20}$$

here $S_l = e^{i2\sigma_l}$ is the scattering matrix term and σ_l is a phase shift term needed due to the potential $V(R)$. Depending on the parts of the potential (real and imaginary) σ_l will correspondingly assume such a part. This way of reasoning shows that the transmission coefficients represent the probability that a particle i undergoes an inelastic interaction process.

One of the main input needed in the calculation amongst others is the nuclear level density $\rho(E, I)$ parameter. This variable is calculated from the Fermi gas expression:

$$\rho(E, I) = \frac{2J + 1}{12} a^{1/2} (\frac{\hbar^2}{2J_{eff}})^{3/2} \frac{\exp(\sqrt{[4a(E - T - E_I)]})}{(E - T - E_I)^2}) \tag{3.21}$$

where a is the level density parameter calculated from the Rotating Liquid Drop Model (RLDM) and it determines the energy dependence, T is the thermodynamic temperature, $E_I = \frac{I(I+1)\hbar^2}{2J_{eff}} + \Delta$ is the yrast curve term which is derived from the RLDM formula, Δ is the pairing correction term, $J_{eff} = J_{sph}(1+\delta_1 J^2+\delta_2 J^4)$ is the

effective moment of inertia, $J_{sph} = 2/5A^{5/3}r_{\circ}^2$ is the spherical rigid body moment of interia where A is a mass number and $r_{\circ}$ is the nucleus radius, $\delta_{1,2}$ are the deformability parameters. The deformability parameters effect the deformation of the compound nucleus under rotation, hence the compound nuclear level density (and in directly the partial fusion reaction cross sections) will be affected by the dynamic deformation of the nucleus. In Table 3.1 the inputs which were used in the present calculations are listed these are the critical angular momentum, the deformability parameters, the beam energy and the total number of simulated events. Default optical model coefficients were used.

Table 3.1: The CACARIZO code inputs for the ^{98}Mo(^{3}He, xn)^{101*}Ru and for the ^{148}Nd(^{3}He, xn)^{151*}Sm evaporation reactions. The listed compound nucleus excitation energies E_{com}[CN], cross sections σ[CN] and critical angular momenta l_{cr} values were obtained from the PACE4 code.

^{98}Mo(^{3}He, xn)^{101*}Ru						
E_{lab}	$E_{com}[CN]$	$\sigma[CN]$	l_{cr}	Total	δ_1	δ_2
[MeV]	[MeV]	[mb]	$\hbar$	Events		
25.0	39	1150	8.0	10^4	10^{-4}	10^{-6}
^{148}Nd(^{3}He, xn)^{151*}Sm						
25.0	36	950	8.0	1×10^{-4}	2×10^{-4}	1×10^{-6}

Table 3.2: The statistical model codes calculation results for the 1n/3n exit channels strengths of ^{101*}Ru and ^{151*}Sm are listed with those from the measurements.The uncertainties on the measured strengths are in the order of 5%.

Codes	Theory ^{101*}Ru	Spin Ratios	Exp	Theory ^{151*}Sm	Spin Ratios	Exp
PACE4	4.8×10^{-5}	$1n(2_1^+)/3n(2_1^+)$	0.05	6.2×10^{-5}	$1n(2_1^+)/3n(2_1^+)$	0.01
		$1n(4_1^+)/3n(4_1^+)$	0.008		$1n(4_1^+)/3n(4_1^+)$	0.003
HIVAP	4.4×10^{-6}			2.0×10^{-4}		
CACARIZO	5.4×10^{-4}			4.5×10^{-4}		

It can be seen that the CACARIZO results are no different from the results obtained with the other two statistical model codes. The latter model predicts very small strengths for the 1n/3n ratios which does not support the present observations. An alternative means of neutron production is to invoke giant dipole resonance (GDR). It is a statistical pre-equilibrium mode, which is A, Z dependent and is not contained in the statistical model. Bothe and Genter in 1937 discovered this mode via the photo-absorptions observed with the ^{63}Cu nucleus [72]. This mode is known as the Isovector Giant Dipole Resonance (IVGDR) having isospin $T = 1$ and results when the protons moves collectively relative to the

neutrons in the presents of an oscillating electric field. It's frequency was correctly predicted by Arkadii B. Migdal [73] in 1944 in terms of sum rules. It is located above the particle emission threshold energy and may de-excites through, nuclear fission, emission of neutrons having energy $E_n \simeq B_n + 2T_c^\circ$ (B_n is the neutron binding energy and T_c° is a temperature) or high-energy γ-rays ($E_\gamma \simeq 10 - 30$) MeV, or combinations of these. Other characteristics are it manifest as a broad bump in the de-excitation spectra. For medium mass nuclei the excitation energy is given by $E_{ex} \simeq 70 - 80A^{-1/3}$. The discussion thus far considered only IVGDR restricted to the ground state, however they can also be build on an excited state according to the Brink-Axel hypothesis [74].

A search of the online nuclear data archives could not found IVGDR cross sections for ^{101*}Ru and ^{151*}Sm [75]. The only information that were found were for the neigbhoring isotopes see Table 3.3, which shows that the process under discussion are populated with very small cross section and centroide excitation energies several MeV away, compared to those for compound nuclei formation see Table 3.1. This information suggest that the enhanced neutron yields detected with the NE102A plastic scintillator detectors could not have been produced as a result of IVGDR.

Table 3.3: Main GDR parameters for nuclei in the vacinity of ^{101*}Ru and ^{151*}Sm[75]

.

Z	A	E_{com}[MeV]	FWHM [MeV]	σ[mb]
42	100	27.3	7	20.3
-	98	28.11	13.3	5
-	92	25	8.2	8.2
62	natural	27.39	10	20.8

3.3 Coupled Channels Analysis

In order to investigate the possibility that the low-lying yrast spin states of ^{100}Ru and ^{150}Sm, were produced via inelastic target excitations followed by proton pair transfers, coupled channels Born Approximation (CCBA) calculations were conducted. There are various codes available that incorporates the channels technique i.e. the CHUCK3 Coupled Channels Born Approximation CCBA code [76] as well as FRESCO [56] amongst others. The latter is a general purpose coupled channel reaction computer code which was written and are still administrate by Ian Thompson [56]. The first code version was written in Fortran 77 but latter updates are Fortran 90 competable. The code can be run in both text and graphical mode (*XFRESCO interface*) on multi-platforms i.e Linux, Windows, Vax and Unix.

FRESCO uses equation 3.22 to calculate the inelastic scattering differential cross section in the laboratory reference frame in units of mb/sr. Where I_i is the excited

state spin and $|A(K_i, K)_{n_i I_i M_i; nIM}|$ is the inelastic scattering amplitude. Here K_i and K are the incoming and outgoing momenta.

$$d\sigma/d\Omega = \frac{1}{2I_i + 1} \sum_{MM_i} |A(K_i, K)_{n_i I_i M_i; nIM}|^2 \tag{3.22}$$

The coupled channel potential $V_{if}(R)$ can be parameterised in terms of the entrance $\theta_i(\epsilon)$ and the exit $\theta_f(\epsilon)$ channels as well as the transition matrix element potential $V_{if}(R, \epsilon)$.

$$V_{if}(R) = \int d\epsilon \theta_f(\epsilon)^* V(R, \epsilon) \theta_i(\epsilon) \tag{3.23}$$

which can be split into a nuclear and a Coulomb potential, the latter potential can be written as:

$$V_{if}(R) = \sum_{\lambda > 0} \frac{4\pi}{2\lambda + 1} \frac{Z_t e}{R^{\lambda+1}} f; I_f M_f | M(E\lambda, \mu) | i, I_i M_i Y_{\lambda\mu}(R) \tag{3.24}$$

Using the Wigner-Eukart theorem (see Bohr and Mottelson for definitions [15]) the Coulomb reduced matrix elements becomes

$$f; I_f M_f | M(E\lambda, \mu) | i, I_i M_i = (2I_f + 1)^{-1/2} I_f M_f | \lambda \mu I_i M_i f I_f || M(E\lambda) || i, I_i \tag{3.25}$$

- For non diagonal transitions in the frame work of the rotor model the reduced electric matrix elements $M_{if}(E\lambda)$ is given by.

$$I_f || M(E\lambda) || I_i = \sqrt{(2I_f + 1) B(E\lambda; I_f I_i)} \tag{3.26}$$

- A similiar exercises was followed to derive the expression for nuclear excitations which is related to the deformation lengths δ_λ.

$$\delta_\lambda = \beta_\lambda R = \frac{4\pi}{3 Z_t e R} \left[B(E\lambda, I_f \rightarrow I_i) \right]^{1/2} \tag{3.27}$$

where β_λ is the nuclear deformation parameter, R is the charge radius, Ze_t is the target charge and B(Eλ,$I_f \rightarrow I_i$) is the reduced electric quadrupole transition probability. The calculations were performed in which the entrance channel was treated by adopting a two state model approach. Further the states were coupled to all orders. Again in order to generate the coupling potentials, a collective model for the target nuclei was assumed. Coulomb and nuclear matrix elements were obtained from the experimental values of the reduced transition probabilities *B(E2)* and the deformation length δ_λ respectively [77, 78]. It must be noted that the ^{148}Nd nucleus has a large E3 matrix element value of B(E3; $0^+ \rightarrow 3^-$) $\sim$ 40 W.u [78] which suggest significant octupole collectivity. Further for the central potential of this ^{98}Mo + ^{3}He reaction the optical potential parameters of Vervier *et al* [79] were used, while for this ^{148}Nd + ^{3}He reaction those of WP.Alford *et al* [80] were adopted see Table 3.4.

Table 3.4: Optical potential parameters for a 25 MeV ^{3}He beam on a ^{98}Mo [79] and on a ^{148}Nd targets [80].

Ch	V_R [MeV]	r_R [fm]	a_R [fm]	W [MeV]	r_I [fm]	a_I [fm]	W_D [MeV]	r_D [fm]	a_D [fm]	V_{so} [MeV]	r_{so} [fm]	a_{so} [fm]
						^{98}Mo						
^{3}He	153.58	1.20	0.72	38.6	1.40	0.88	0	-	-	2.5	1.20	0.72
						^{148}Nd						
^{3}He	170.10	1.16	0.75	17.0	1.49	0.82	0	-	-	2.5	1.20	0.72

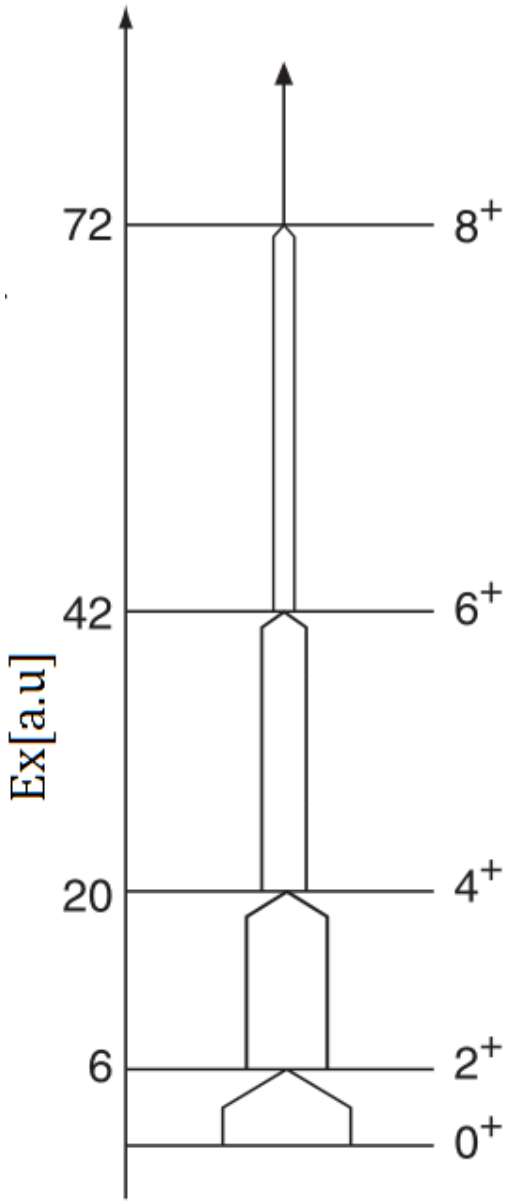

Figure 3.4: An illustration of inelastic excited spin states. The arrow thickness denotes the strengths which decrease with increasing excitation energy.

Table 3.5: The FRESCO multistep results for the low-lying yrast spin states of ^{98}Mo and ^{148}Nd. The strengths were normalised to those of the $2_1^+ \rightarrow 0_1^+$ spin states which were set to 1.

E_{ex}[MeV]	J_i^π	$\rightarrow$	J_f^π	$I_f\|\|\text{E2}\|\|I_i$[eb]	δ_2[fm]	^{98}Mo(^{3}He,^{3}He)^{98}Mo
0.787	0_1^+	$\rightarrow$	2_1^+	0.526	0.929	1.0
1.510	2_1^+	$\rightarrow$	4_1^+	1.01		3.1×10^{-2}
2.345	4_1^+	$\rightarrow$	6_1^+	0.593		1.2×10^{-3}
3.272	6_1^+	$\rightarrow$	8_1^+			5.4×10^{-5}
E_{ex}[MeV]	J_i^π	$\rightarrow$	J_f^π	$I_f\|\|\text{E2}\|\|I_i$[eb]	δ_2[fm]	^{148}Nd(^{3}He,^{3}He)^{148}Nd
0.301	0_1^+	$\rightarrow$	2_1^+	1.138	1.112	1.0
0.752	2_1^+	$\rightarrow$	4_1^+	2.0		3.0×10^{-2}
1.279	4_1^+	$\rightarrow$	6_1^+	2.62		1.0×10^{-3}
1.856	6_1^+	$\rightarrow$	8_1^+	2.89		5.0×10^{-5}

In order to compare the code estimates with the measurements a similiar procedure as in section 3.2.1 were followed. The predicted inelastic scattering strengths for the yrast spin states at $\theta_{lab} = 0^0$ are smaller than the measured strengths see Table 5.1 and 5.2. The conlusion drawn is that the inelastic excitation mechanism cannot explain the observed yrast transition strengths.

3.3.1 The GOSIA code

Gosia is a Fortran code which was orginally written by T. Czosnyka, D. Cline and C.Y. Wu [57]. It is a semiclassical coupled channel Coulomb excitation least square search code and was develop from the Winther and de Boer code [81]. This code is multifunctional since it can perform multidimensional fits of matrix elements to data points and it can simulate γ-ray transition intensities as well as excitation probabilities. It takes input (matrix elements, level scheme, spectroscopic data, particle and γ-ray detectors setups etc) from the command line however input files can also be generated with the Rachel graphical user interface routine [57]. Consult Ref.[82] and references therein for a comprehensive description of the code.

It must be noted that the criteria for Coulomb excitation, stipulates that the projectile bombarding energy should be smaller than or equal too the safe energy E_{safe} (for pure Coulomb excitation) which is parameterised in equation 3.28 in terms of the projectile (target) mass $A_{1,2}$ and projectile (target) charge $Z_{1,2}$ [57]. It was found that the present projectile beam energy is roughly 0.40% to 0.5% larger then the estimated safe Coulomb excitation energies.

$$E_{safe} = 1.44\frac{A_1 + A_2}{A_2}\frac{Z_1 Z_2}{1.25(A^{2/3} + A^{1/3})} \tag{3.28}$$

Therefore the yrast transition strengths listed in Table 6.1 and 6.2 cannot be attributed to a multistep reaction mechanism.

3.4 The NuShellX code

Independant particle calculations were done with the NuShellX codes sets written by Bill Rae [59] to evaluate if the two proton component of the $I^{\pi} = 0_2^+$ spin state located at $E_{ex} = 1.130$ MeV which belongs to ^{100}Ru is consistent with the present direct reaction observations. The code uses the proton-neutron J-coupled basis with J-scheme matrix dimensions of up to the order of 10^6. It calculate excitation energies, (iso)spins, parities, spectroscopic factors, electromagnetic transition probabilities as well as one and two particle transfer ampitudes.

The NuShellX@MSU wrapper codes sets written by Alex Brown [83] was also used, it provided a user friendly interface to input data and it converts the output into figures and tables. In Fig 3.5 the NuShellX@MSU layout is shown for a detailed description of these codes, consult Ref.[84]. In the present calculation the *gl* model space [85] and *gl* interaction matrix, employing a ^{88}Sr core were used. This model space spans the ^{100}Ru valence Z-orbitals of $2p_{1/2}$ and $1g_{9/2}$ and the valence N-orbitals of $3s_{1/2}$ and $2d_{5/2}$. It generate 12 valence nucleons (six protons and six neutrons) which did not require further truncating of the model space. In Fig 3.6 a) the measured level energies having angular momentum 0, 2, 4 and 6 are compared with those which are predicted by the shell model see Fig.3.6 b). According to the shell model both neutron and proton orbitals contributes to the final angular momenta see Table 3.7. In addition there exist large discrepancies between the relatively positions of the predicted and measured energy levels. However the relative ordering of the level energies is reproduced by the calculations. Further, an interesting observation is that the low-lying yrast transitions were populated with relative large strengths see Table 5.1 and 5.2. The yrast B(E2) transition probabilities shown in Fig 3.7 were reported by T. Konstantinopoulos *et al.*, [86] and calculated with the NuShellX code amongst others, using the *jj45pn* valence space and the *jj45pna* interaction. In Fig 3.7 it can be seen that the measured trend is reproduced but the code fell short of account for the experimental values, this is because the transitions have a collective origins.

In Table 3.6 the main code output of interest for the $I^{\pi} = 0_2^+$ level is listed. It can be seen that 78.9% of the wave function comes from $J = 0$ couplings of protons and neutrons with almost 50.0% of the wave function resulting from an excitation of the pair of $2p_{1/2}$ protons into the $1g_{9/2}$ orbital by the residual interaction. Thereby increasing the total number of protons that reside in the $1g_{9/2}$ orbital to six. The ($J_{\pi} = 2$, $J_{\nu} = 2$) coupling is responsible for 19.82% of the wave function and ($J_{\pi} = 4$, $J_{\nu} = 4$) couplings contributing 1.21%. Based on the NuShellX results it is proposed that the $I^{\pi} = 0_2^+$ spin state has a dominant proton pair character.

Table 3.6: The NuShellX [59] predictions for the $I^{\pi} = 0_2^+$ spin state of ^{100}Ru.

I^{π}	$J_{\pi} \times J_{\nu}$	E_{ex} [keV]	E_{γ} [keV]	E_{th} [keV]	ν Orbitals		π Orbitals		Partial
					$3s_{1/2}$	$2d_{5/2}$	$2p_{1/2}$	$1g_{9/2}$	Amp
					2	4	0	6	49.65
0_2^+	0	1130	590	1644	1	5	2	4	2.52
					0	6	2	4	0.57
					2	4	2	4	26.20
	2				0	6	2	4	0.23
					2	4	1	5	1.53
					2	4	2	4	18.06
					1	5	2	4	0.02
	4				2	4	2	4	1.09
					0	6	2	4	0.13

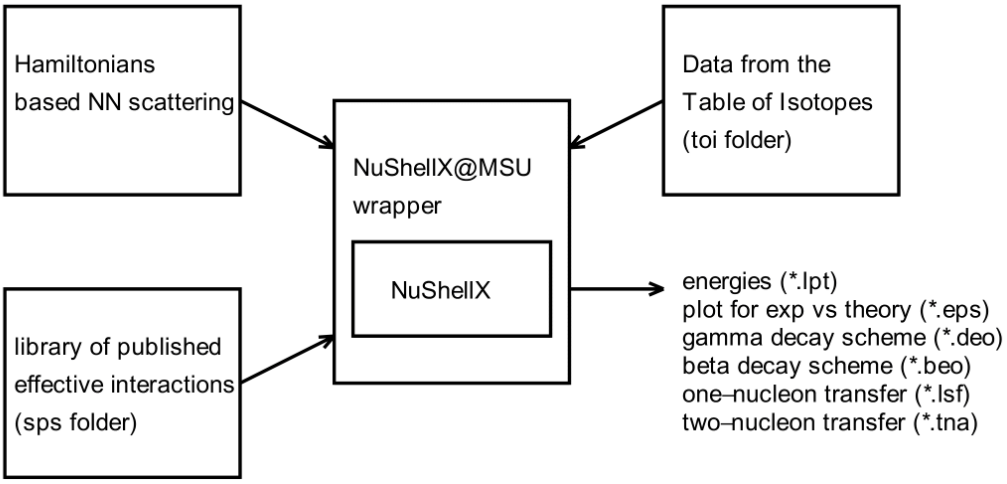

Figure 3.5: A layout of the NuShellX@MSU [84] wrapper codes sets.

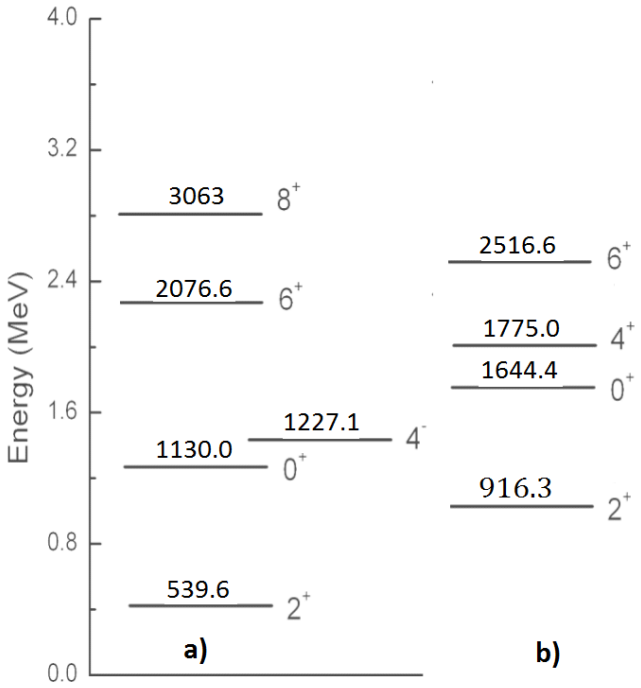

Figure 3.6: Comparison btweeen the measured a) and the NuShellX [59] predicted ^{100}Ru energy levels b). The level energies are in keV units.

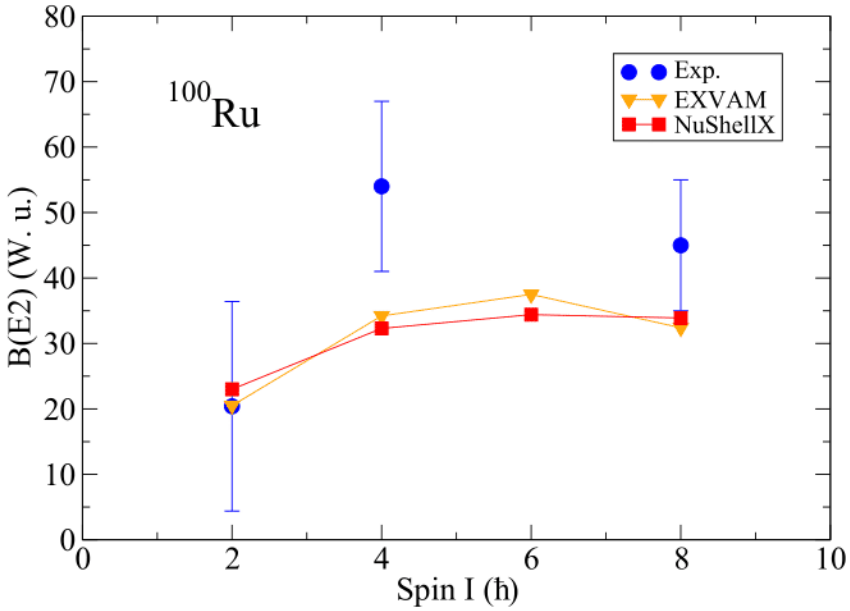

Figure 3.7: The experimental and calculated B(E2) values for the low-lying yrast transitions reported by T. Konstantinopoulos *et al* [86].

3.5 GEANT4 Simulations

The GEometry ANd Tracking (GEANT4) code [60] simulates the passage of particles through matter via Monte Carlo methods. It is an object oriented code that is written in `C++` which was first developed by CERN. It found applications in medicine, space sciences, nuclear, high energy physics and accelerators physics. In the present measurements the toolkit was used to roughly simulate how many fusion evaporation neutrons that originates from the 1n evaporation channels of the compound ^{101*}Ru and ^{151*}Sm nuclei. Deposited sufficient energy into the NE102A plastic scintillator detectors via elastic collisions with the hydrogen and ^{12}C nuclei. This information was use to deduce the neutron detection efficiency ϵ_{tot} of the plastic scintillator detectors, which assisted to explain the observed relative strengths of the low-lying yrast spin states.

In order to build the application GEANT4 requires that the experimental setup, the physics processes and the primary particles must all be defined. It must be noted that all six NE102A plastic scintillator detectors were modelled as a single $(600 \times 600 \times 100)\ mm^3$ slab without the photomultiplier tubes. In the application the predefined QGSP_BIC_HP physics list was used. It takes into account all the physics processes involved in the reaction i.e. the various interactions of the incident fast neutrons with the NE102A material. It covers the energy range from 1.0 MeV to 20 MeV as well as higher energies. Furthermore the primary particles originates from a particle gun and it was directed to shoot randomly within the solid angle covered by the plastic scintillator detectors. Additional user interaction classes (i.e. the G4UserEventAction, the G4UserRunAction and the G4UserActionInitialization) were also created to extract the 1D neutron energy distributions.

Statistical model code calculation results for emissions from the compound ^{101*}Ru nucleus (Fig 3.8) shows that the bulk of the 1n exit channel neutrons have emission energies between 14 MeV to 28 MeV. In Fig 3.9 it can be seen that these energies corresponds to relative large efficiencies. The efficiencies can be explained in terms of the rotational evaporation mechanism put forward by T.Dossing *et al* [87] and is supported by in-plane and out of plane charged particles angular distribution measurements which was conducted by D. Mahboub *et al* [88] and many others. According to T.Dossing *et al* [87, 89] the evaporated particles angular distributions in the laboratory reference frame can be classically parameterised as:

$$W(\theta_{lab}) \sim 1 + \frac{\beta_2}{2} cos^2(\theta_{lab}) \tag{3.29}$$

where the parameter $\beta_2 = \frac{\mu\omega^2 R^2}{2T}$ accounts for the rotational emissions (numerator) and thermal emissions (denumerator). The angle θ_{lab} is the emission angle with respect to the beamline. For small values of θ_{lab}, $W(\theta_{lab})$ is dominated by the rotational emissions. This happens when two spin zero particles collide with the orbital angular momentum of their relative motion orientated perpendicular to the velocity of the projectile. Hence the compound nucleus orbital angular momentum

will be in a plane perpendicular to the incident beam see Fig 3.10. The most effective way for the compound nucleus to de-excites is to emit particles. Not only does it dissipate energy but also angular momentum, once more this is orientated perpendicular to the angular velocity $v = \omega R$. Hence particle emission will mostly likely be perpendicular to the compound nucleus orbital angular momentum $J_\circ$ axis. Therefore, particles are preferentially emitted with maximum cross section probability on a disk where the diameter is along the beam axis. The traditional picture usually is to compare the disk of a grinder to the plane of rotation of a nucleus. The sparks fly within the plane (see Fig 3.10), not out of plane.

Thus happens mostly within the solid angle covered by the NE102A scintillator detectors. These detectors on averaged recieved more evaporation neutrons than initially believed meaning more γ-rays from the excited residual nuclei were detected with the clover detectors.

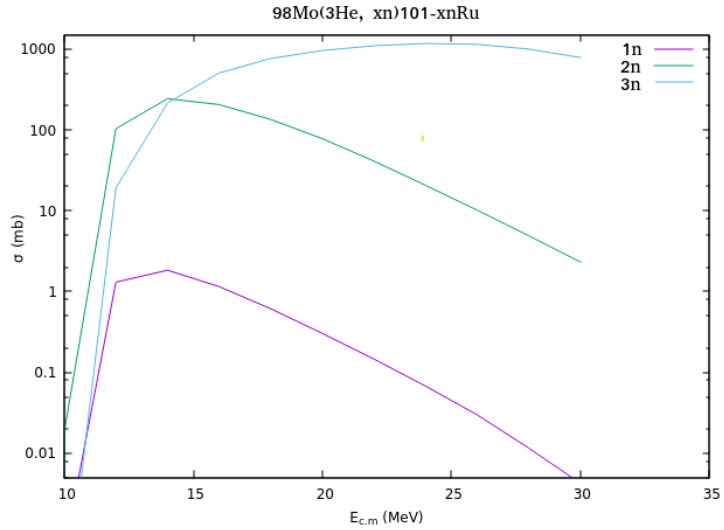

Figure 3.8: The ^{101*}Ru compound nucleus 1n, 2n and 3n exit channel center of mass emission energies are trended against cross sections, these results were estimated with the HIVAP statistical model code [53].

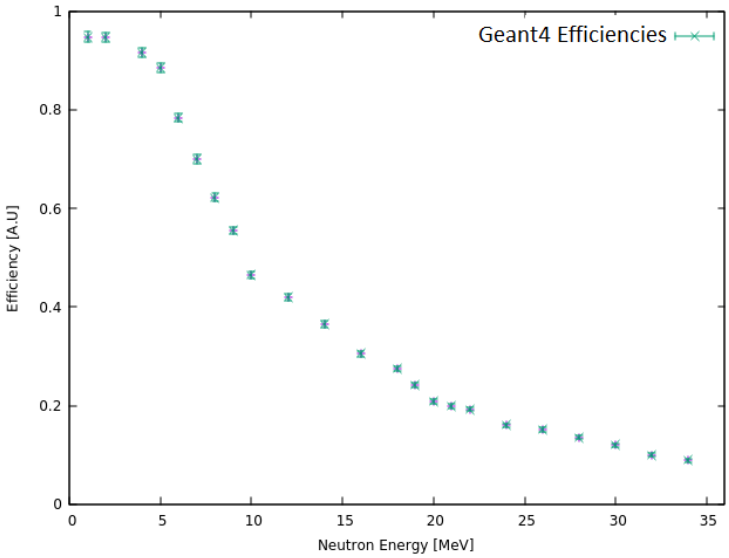

Figure 3.9: The GEANT4 simulated NE102A plastic scintillator neutron detection efficiencies versus deposition energies.

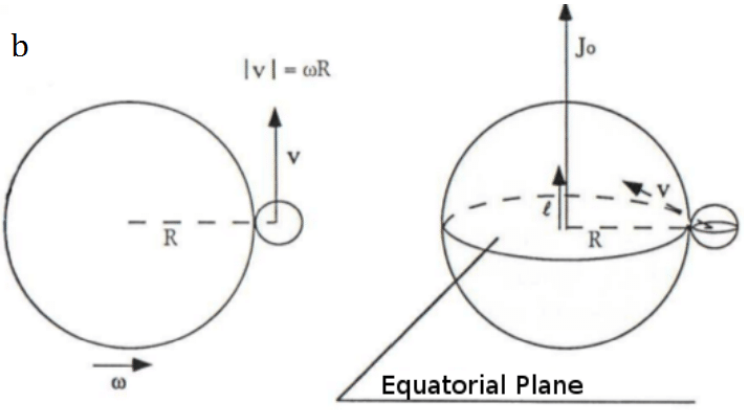

Figure 3.10: The illustration show a particle that is evaporated in a plane perpendicular to the compound nucleus orbital angular momentum [90].

Chapter 4

Experimental Method and Data Analysis

4.1 Introduction

Two sets of high resolution two proton stripping (^{3}He, nγ) reaction measurements were performed by operating the AFRODITE HPGe detector array in coincidence with a wall of large volume NE102A plastic scintillator detectors placed 2.0 m downstream of the target. The measurements took place at iThemba LABS in Cape Town, South Africa using 12 days beam on target time. The beam was produced by the Seperated Sector Cyclotron (SSC) and the choice of bombarding energy was 25.0 MeV for ^{3}He particles on isotopically enriched targets of ^{98}Mo and ^{148}Nd. This bombarding energy is less than the Coulomb barrier $\sim$ 27 MeV for α-particles on lead therefore, a lead Faraday cup was used to intercept the beam between the target and the neutron wall.

In this section the details of the measurement will be discussed.

4.1.1 Neutron Time-of-flight Trigger

Two proton states can be populated via heavy-ion reactions e.g. (^{6}Li, ^{8}B), (^{11}B, ^{13}N) and (^{18}O, ^{20}Ne) amongst many others but these reactions often lead to structureless angular distributions [91]. In addition cross sections obtained with such reactions are normally very small and poorly described by DWBA methods. Lastly ejectile and projectile excitations also contribute to spectra contamination.

An alternative way to populate two proton states is to use the (^{3}He, nγ) reaction together with the time-of-flight trigger (t-o-f). However this reaction has one major disadvantage which is the poor neutron energy detection resolution. Apart from the aforementioned problem, this reaction also have advantages for example

spectra obtained with it, have generally less contamination. Different L-value transfers can easily be selected because their angular distributions exhibit strong characteristic features.

The t-o-f trigger involves generation of a start signal at the instant of neutron detection and a stop signal generated from the radio frequency reference signal of the accelerating voltage and an electronic measurement of time interval between the two signals. In the present cyclotron based measurement the start time was derived from NE102A plastic scintillator detectors. The stop signal came from the cyclotron RF. In routinely performed t-o-f measurements most of the time resolution depends on the time jitters in the start and stop pulses, the inherent resolution of the time measuring electronic modules which in the present case was a set of time to amplitude converters (TAC's). The TAC'S experienced time jitter hence it was not possible to time calibrate them additional contributing factors were:

- The time jitters of the coincidence modules.
- The time structure of the beam pulse.
- The thickness of the neutron detectors (uncertainty of the flight path).
- The geometry of the detectors (center closer to the target than the edges).
- The transit time of the photons within the NE102A bars and electrons within the PMT's [92].

Finally, the Compton suppressed large volume HPGe detectors made it feasible to conduct the direct proton pair stripping reaction (^{3}He, nγ) at high resolution. This was achieved by detecting the direct reaction γ-rays in coincidence with the outgoing fast neutrons, which were recorded with the NE102A plastic scintillator detectors positioned at forward angles ranging from $\theta_{lab} \sim 0^\circ$ to 10°. This is in contrast to former two proton stripping measurements, where poor resolution (FWHM $\sim$ 300 keV to 500 keV) were normally obtained over short flight paths [80, 93].

4.1.2 Time Calibration

As previously pointed out the electronic modules especially the TAC's experienced time jitter. Hence it was not possible to use them to extract neutron energy distributions. However the two γ-ray peaks in the 1D time-of-flight versus counts spectrum shown in Fig.4.1, were used for that purpose. The peaks are narrow because all γ-rays travel at the speed of light and thus reach the scintillators at a time corresponding to the target (beam stop) distance divided by the speed of light 30 cm/ns. For a target separation of 200 cm the γ-ray peak centroid appears at 6.66 ns. Equation.4.2 was used to deduced the beam stop γ-ray arrival time at

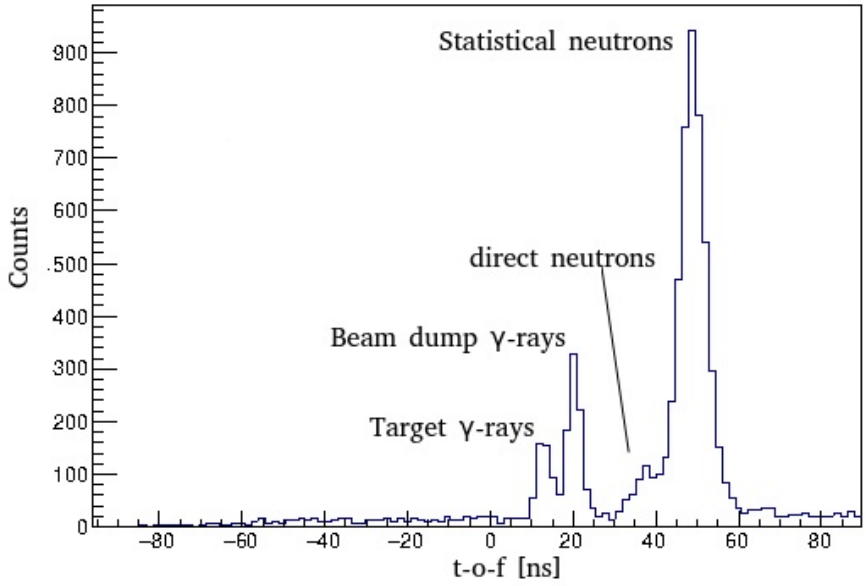

Figure 4.1: The t-o-f spectrum comes from the two proton stripping reaction (^{3}He, nγ) at a beam energy of $E_{lab} = 25$ MeV. The first peak comes from the target γ-rays, the second peak comes from the beam stop γ-rays, followed by the direct reaction neutrons. The pronounced peak originates from the relatively slow moving statistical neutrons.

the scintillators, which consist of two parts. The first part is the time (12.5 ns) that the ^{3}He beam (with a speed of 4 cm/ns) took to transverse the 50 cm to the beam stop. The second part is the time (5 ns) that the beam dump γ-rays took to cover the 150 cm to the NE102A plastic scintillators detectors. Therefore it is expected that the beam dump γ centroid will be positioned roughly at 18 ns on the time-of-flight axis. The neutrons have a much broader distribution of speeds as a direct result of their Q-values and continuous Maxwellian energy distribution of the fusion evaporation channels. Finaly the target γ-ray peak was Gaussian fitted in order to extract the FWHM time resolution of the plastic scintillators a value of 2.2 $\pm$ 0.5 ns was obtained.

4.1.3 Time-of-flight n-γ Discrimination

Equation 4.1 parameterises the kinetic energy E_n of an outgoing neutron in terms of the ground state reaction Q-value, the beam E_{beam} and recoil E_{recoil} energy. While the neutron t-o-f is formulated in equation 4.2 in terms of the flight path l , the neutron rest mass m and particle kinetic energy E_n.

When a 25.0 MeV ^{3}He beam collides with a ^{98}Mo target nucleus the reaction is exothermic with a Q-value of 7.79 MeV. PACE4 [52] estimate a recoil energy of $E_{recoil} \sim 0.74$ MeV for the ^{101*}Ru compound nucleus. This is about 2% compared to the direct reaction neutron energy of 32 MeV which correspond to a velocity of 79.0 mm/ns that take 25.0 ns to travel the 2.0 meters distance to the plastic

scintillators detectors. This is in contrast to the competing statistical neutrons from the (^{3}He, xnγ) fusion-evaporation reactions which have energies peaking at about 2 MeV (see Figure 3.2) and are less than 1% of maximum at 6 MeV. These 6 MeV neutrons have a velocity of 34 mm/ns (v/c = 11.3%) taking $\sim$ 60 ns to travel 2.0 meters. The bulk of the statistical neutrons will take $\sim$ 130 ns to transverse the 2.0 meters.

As the velocity of the neutrons is proportional to $\sqrt{E_n}$ it follows that the direct reaction neutrons have about twice the velocity of the statistical neutrons and may be separated from them by the t-o-f method over the relatively short distance of 2.0 m. Thus the γ-rays, direct neutrons and statistical neutrons are well separated by time-of-flight. It should be remembered that the statistical neutrons are emitted isotropic on a disk and symmetric at right angles to the orbital angular momentum of the compound nucleus [88]. In the slow moving centre-of-mass reference frame. Whereas the $L = 0$ neutrons from the (^{3}He, nγ) reactions have most of their cross section peaked at $\theta_{lab} = 0°$ [80, 93]. In addition the plastic scintillator detectors subtend a small solid angle to the statistical neutrons of about 1% of 4π.

$$E_n \sim Q_{g.s.} + E_{beam} - E_{recoil} \tag{4.1}$$

$$\text{t-o-f} \sim \frac{l \times \sqrt{m}}{4\sqrt{2} \times 10^{-8}\sqrt{E_n}}. \tag{4.2}$$

4.1.4 Target Manufacturing

The ^{98}Mo and ^{148}Nd targets materials were supplied by Isoflex [94]. To manufacture the ^{98}Mo target, 98.42% enriched material in powder form was melted under vacuum using a tungsten filament electron-gun in order to remove oxygen from the powder. This was followed by cold rolling of the metal pellet to the final thickness.

In the manufacturing of the ^{148}Nd target, 97.40% enriched ^{148}Nd oxide powder, was mixed with filings of Hafnium in a stoichiometric ratio of 1.5 this was convert into a metallic form [94]. The mixture was then compressed into a pellet and transferred to a Ta boat where the Nd was evaporated while it was reduced under vacuum by heating it using an electron gun. The melted Nd metal was collected on a copper water cooled crucible and finally a pure solid metallic ball was rolled under an inert atmosphere inside a glove box. This process was achieved by inserting the collected Nd metal into polished stainless steel plates folded into an envelope shape, and the process was repeated until the final thickness was reached. The rolled Nd metal was mounted on standard AFRODITE frames and stored under vacuum to minimize the oxidation process. A rough idea of the target thickness was available from the weight and surface area of the target material used in the manufacturing process. The specific thickness of the (^{148}Nd: $\sim$ 5.2 mg.cm^{-2} and ^{98}Mo: $\sim$ 10.1 mg.cm^{-2}) targets was determined by α-particle energy attenuation and X-ray absorption measurements.

4.1.5 Experimental Setup

In the present measurement a 25.0 MeV $^{3}He^{+}$ beam pulsed with a time structure of 270 ns and having a time spread of 1 ns FWHM was delivered by the Separate Sector Cyclotron onto the ^{148}Nd target. The same beam also irradiated the ^{98}Mo target. The time average count rate on the clovers was typically of the order of 25 kHz and 40 kHz on a plastic scintillator detector.

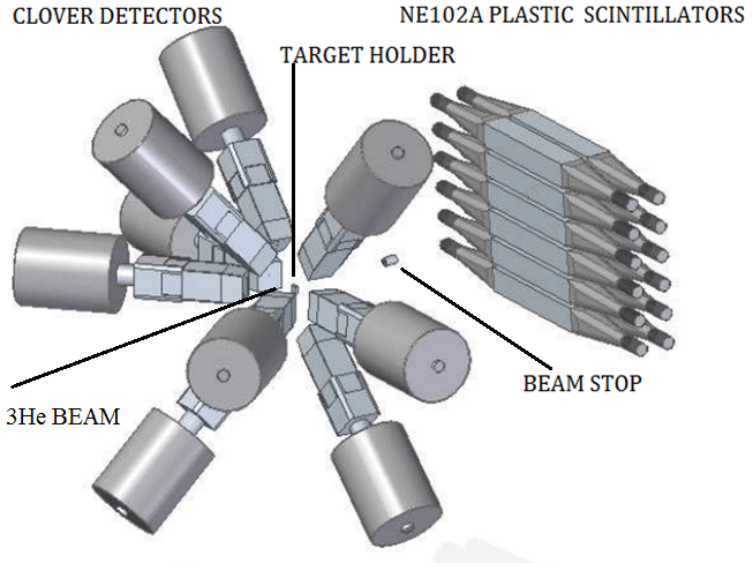

Figure 4.2: An illustration of the experimental setup. The target holder is at the centre, surrounded by nine clover detectors. The beam dump is also shown with the neutron wall positioned at the back.

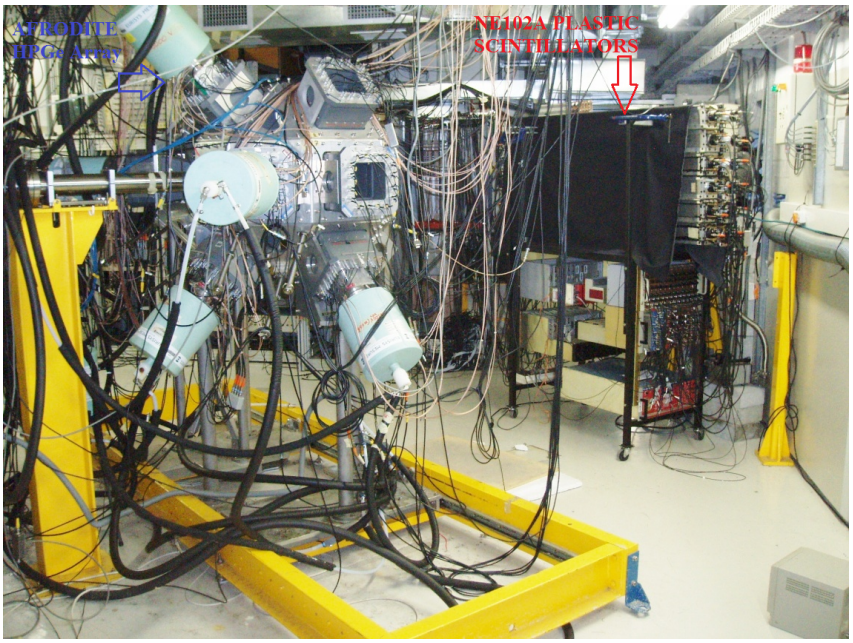

Figure 4.3: The AFRODITE HPGe detector array is shown in the foreground, while the NE102A plastic scintillators are covered with a black cloth and are at the back.

4.1.6 AFRODITE HPGe Detector Array

A picture of the AFRODITE HPGe detector array is shown in Fig 4.3. It consists of a rhombicuboctahedron with 15 detector positions. The target chamber has the same geometry with 5 mm windows on the 16 square faces. Normally the AFRODITE HPGe detector array consists of nine clover detectors which are more or less like the EUROBALL III type geranium detectors and eight LEPS detectors for photon detection between 30 keV and 300 keV. During the measurements no LEPS detectors were used. The clovers were placed in rings at $\theta_{lab} = 90°$ and 135° around the target chamber. Their fronts were covered with 1.2 mm thick copper absorber plates to absorb X-rays, especially those that originates from the relative high-Z target material. These detectors subtend a solid angle of 8% of 4π. Each clover consists of a closed arrangement of four n-type germanium crystals to improve the add-back factor. The clovers are multi-detector assemblies therefore the effect of Doppler broadening which is maximum at 90° is minimal for the clovers. The maximum gap between two adjacent crystals is 0.7 mm without any absorbent material along the whole crystal length. All four crystals are housed in a common cryostat with a tapered end cap. The distance between the front size of the end cap and the crystals is 0.2 mm . Normally germanium crystals are surrounded by a BGO shield, to suppress the Compton scattered γ-rays.

4.1.7 AFRODITE Relative Efficiency Calibrations

Not all γ-rays that are emitted by the source and that pass through the detector will produce a count in the system. The probability that an emitted γ-ray will interact with the detector and produce a hit is the peak efficiency of the detector. The peak efficiency is energy dependent because high energy γ-rays have a tendency to scatter out of the crystal, which will result in missing counts in the individual observed peaks. Therefore when extracting the intensity of a γ-ray transition one needs to correct for the missing counts by taking the ratio of the photopeak events and γ-ray transition efficiency. For this measurement the relative efficiency of the nine HPGe detectors need to be well known between 300 keV and 1600 keV as the transitions that depopulates the low lying $I^{\pi} = 0^{+}$ spin states lie within this energy range.

The relative efficiencies of the AFRODITE HPGe detectors were obtained by calibrating all the nine clover detectors with a standard ^{152}Eu γ-ray source immediately after each measurement so that the detector responses are the same as for the experimental data. The calibration sources were placed at the centre of the array and data were recorded for several hours to accumulate sufficient statistics. Thereafter the raw calibration source data file was analysed with the Radware *xmgf3* code [95]. The end result was a *.sto* file that contains the γ-ray photopeak counts, centroids, energies, and channel numbers. The Radware code *SOURCE* was used to combine the raw source *.sto* file, with a standard *.sou* data file containing fixed energies and relative intensities of ^{152}Eu γ-rays. The *SOURCE* program created a

.sin file that was used as input to the curve fitting program *EFFIT*, which fitted equation 4.3.

$$\epsilon = \exp([(A + Bx + Cx^2)^{-G} + (D + Ey + Fy^2)^{-G}]^{-1/G}). \tag{4.3}$$

to the source data points. The seven parameters of the calibration that were adjusted are labelled A through G and are listed in Table 4.1. with $x = \log(\frac{E_g}{E_1})$ and $y = \log(\frac{E_g}{E_2})$. The parameters A, B and C describe the efficiency at low energies, so that on a log-log plot the efficiency curve is $A + Bx + Cx^2$, i.e.

$$\log(\epsilon) = A + B\log(\frac{E_g}{E_1}) + C\log(\frac{E_g}{E_1})^2 \tag{4.4}$$

Similarly D, E and F describe the efficiency at high energies,

$$\log(\epsilon) = D + E\log(\frac{E_g}{E_2}) + F\log(\frac{E_g}{E_2})^2 \tag{4.5}$$

Here E_g is the γ-ray energy, and the constants E_1 and E_2 have the values 100 keV and 1 MeV, respectively. The parameter C is in general not required, and is by default fixed to zero, G is an interaction parameter between the two regions; the larger G is, the sharper will be the turnover at the top in Fig 4.4. If the efficiency turns over gently, G will be small. In Fig 4.4, it can be seen that the turnover point is at about 180 keV. From the relative efficiency fit an efficiency file was created which was used by the Radware *ESCL8R* code [95] to apply least squares fittings directly to the 2D γ-ray data in order to extract the relative intensities and energies of the level scheme transitions.

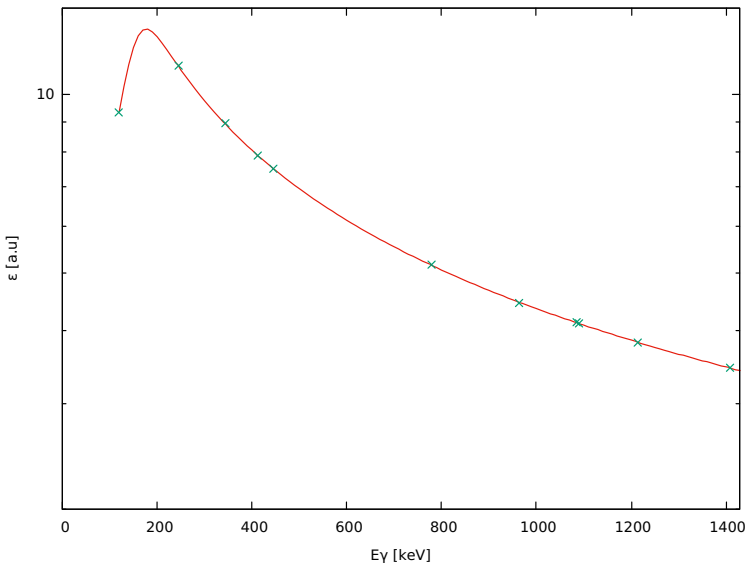

Figure 4.4: Relative efficiency plot for the AFRODITE HPGe detector array vs γ ray energies. The experimental data points are from a standard ^{152}Eu γ-ray source. The solid red line is the result of a least-square fit using the Radware [95] *EFFIT* program.

Table 4.1: Clover detector relative efficiency calibration coefficients.

Parameters	A	B	C	D	E	F	G
Values	2.0(9)	2.0(8)	0.0(0)	1.28(4)	-0.9(19)	-0.1(9)	15.0(11)

4.1.8 AFRODITE Energy Calibrations

Calibrating the clover detectors for energy is an important part of γ-ray spectroscopy analysis. By using a standard γ-ray source, one can match the detector's response to the expected results, thereby calibrating the data to the environment of the specific experiment. The clover detectors were calibrated for energy with the ^{152}Eu standard γ-ray source. The raw calibration data file was then sorted to extract a 1D histogram which provided the calibration points shown in Fig 4.5. The calibration data points were then fitted with a first order polynomial again (due to very good electronic linearity), here the calibration coefficient a=- 127.686±0.165 is the intercept on the energy axis which describe the amount of shift present in the data channel x. The coefficient b= 0.49982± 9.0×10^{-5} is known as the energy dispersion it denotes the rate of energy change in channel numbers. Both parameters values were determined by a least square fit to the multiple data points, which was performed with the Radware *ENCAL* program [95]. The linear fit provided an energy calibration with an accuracy of 0.1 keV over the energy range 0-2 MeV. Each clover elements calibration coefficients were further used as gain correction coefficients to gain match all 36 clover elements.

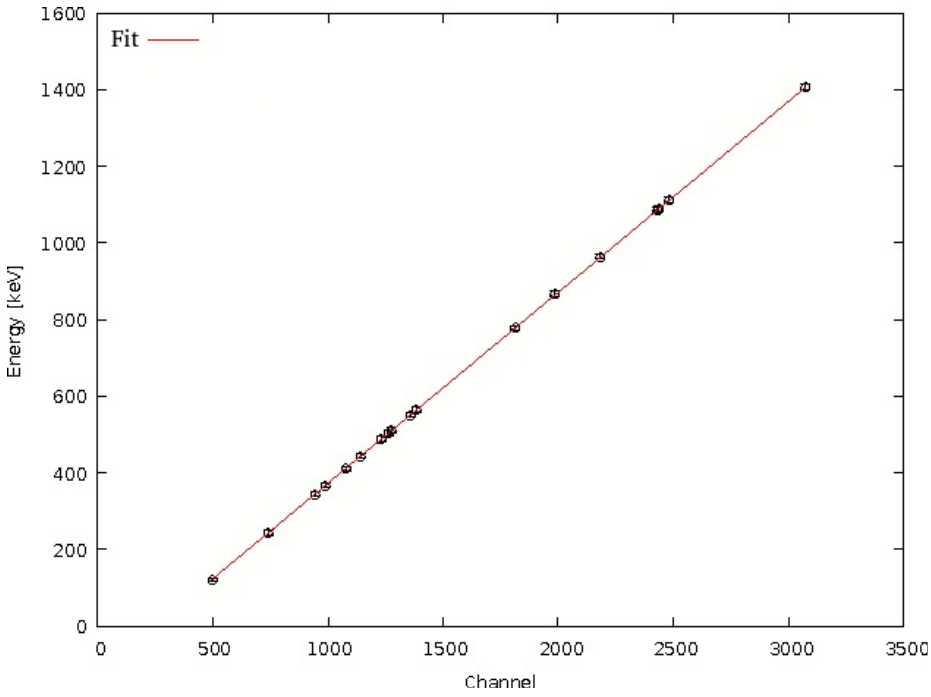

Figure 4.5: Clover detectors linear energy calibration. The data points are from a standard ^{152}Eu source and the errors are of simbol size. The solid red line is a least-square fit performed with the Radware [95] *ENCAL* program.

4.1.9 FWHM-Calibration

Gamma rays detected in a spectroscopic system produce peaks in the spectrum. These peaks can also be called γ-ray transitions by analogy to optical spectroscopy. The width of the peaks is determined by the resolution of the detector, which is a very important characteristic of γ-ray spectroscopic detectors. Good resolution enables the spectroscopist to separate two γ-ray transitions that are close to each other. The most common figure used to express detector resolution is the Full Width at Half Maximum (FWHM). This is the width of a γ-ray peak between the background underneath the peak at half of the highest point on the peak distribution. Equation 4.6 parameterised the FWHM in terms of *f*, *g* and centroide position x denoted in keV units. The first term is due to noise in the detector and amplifier and the second term originates from the statistics of the charge collection process. The experimental widths, which are, shown in Fig 4.6 were obtained from fitting a few ^{152}Eu peaks with the Radware *xmgf3* fitting procedure. These were then again fitted to obtain the parameters values of $f = 1.00 \pm 0.04$ and $g = 23.58 \pm 1.41$ for an energy dispersion of 0.5 keV per channel.

$$\mathrm{FWHM(x)} = \sqrt{f^2 + g^2 \times E_\gamma}. \tag{4.6}$$

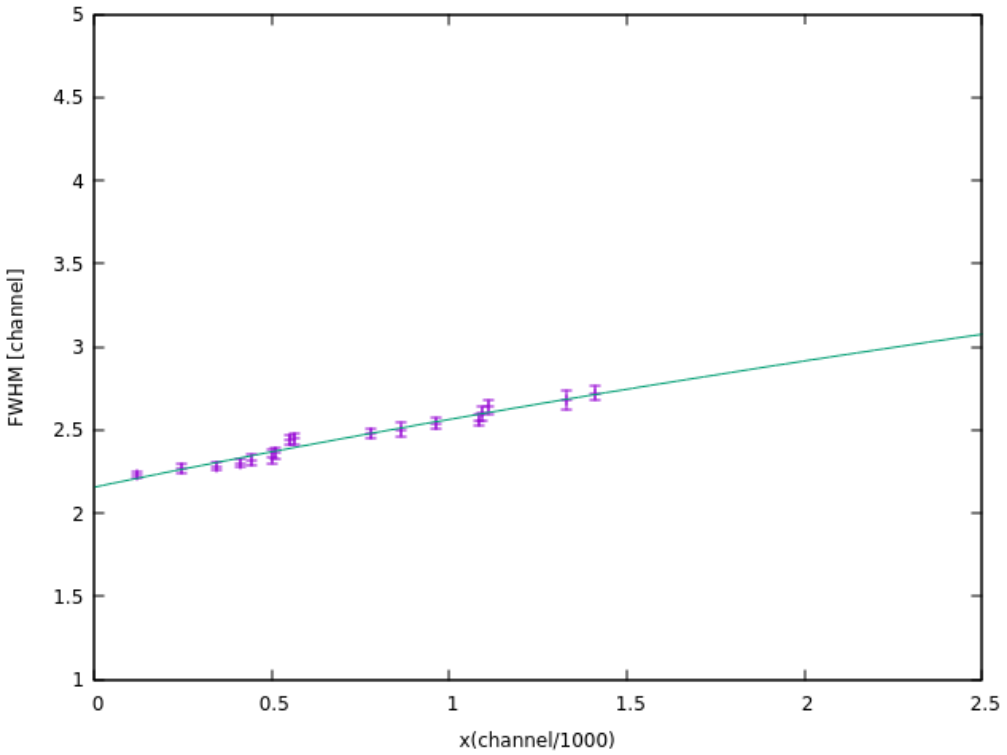

Figure 4.6: The FWHM values are trended against channel numbers. The data points were taken from a standard ^{152}Eu γ-source spectrum and the solid line is a fit of equation 4.6 to those points.

Finally the parameters were used to execute the Radware program *ESCL8R* and

to set manual gates in the matrix in order to extract 1D γ-ray spectra and to fit relative transition intensities directly to the 2D data.

4.1.10 NE102A Plastic Scintillators

In the measurement six large volume NE102A plastic scintillators detectors were used to detect the fast neutrons that were emitted at forward angles. Each detector consists of a $600 \times 100 \times 100 mm^3$ rectangular bar of NE102A plastic scintillator illustrated in Fig 4.9. The two conical Perspex light guides, at either end of the bar, transport the scintillation light to the two Hamamatsu R329 photomultiplier tubes which are covered with muon shields. The NE102A material has a density of $1.032 gcm^{-3}$, a refractive index of 1.58 and is covered with a light insulation material to completely cut-off external photons, as the photomultipliers are extremely sensitive to visible light. The high emissivity material is also important to absorb photons escaping the scintillator. It improves the energy resolution and timing. Additional properties are listed in Table 4.2.

Table 4.2: NE102A plastic scintillator standard properties.

Properties	NE102A
Relative Light Output (% Anthracene)	65
Rise Time [ns]	0.9
Decay Time [ns]	2.2-2.5
Pulse Width, FWHM [ns]	2.7-3.2
Light Attenuation Length [cm]	250
Wavelength of Max. Emission [nm]	425

The scintillators could not differentiate between neutrons and γ-ray events, since pulse shape discrimination was not used. The scintillators covered a total area of $0.6 \times 0.6 m^3$ with a wall thickness of 0.1 m. The wall was positioned 2.0 m downstream from the target position and covered a solid angle of $\Omega \sim 0.09$ sr in the forward direction with an efficiency of approximately 12% (see Fig 3.9) to detect the 32 MeV neutrons at small angles. The short flight path is sufficient to select neutrons originating from the direct reaction, since they arrived first at the neutron wall compared to the slower moving evaporation neutrons. The former were detected at the same instance when γ-rays were detected with the clover detectors. Thus allowing that high-resolution γ-ray spectroscopy measurements can be conducted with the HPGe detectors.

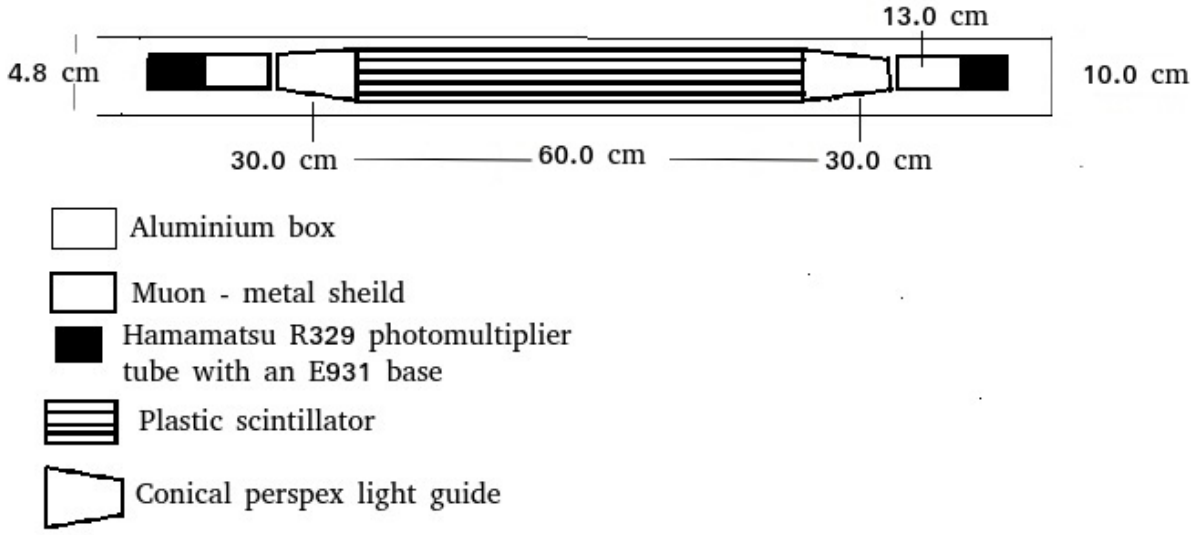

Figure 4.7: Technical illustration of a NE102A plastic scintillator detector.

4.1.11 Energy Calibration of the Plastic Scintillators

Cosmic-ray muons were used to calibrate one of the six NE102A plastic scintillators planks. Theafter the other scintillators were calibrated relative to the initial calibrated one. The muon is an elementary particle whose charge and spin are equal to that of the electron. However it is almost 207 times more massive than the electron. They have energies that ranges from sub GeV to energies that are larger than 10^{20} eV, with no upper limit ever observed. However at sea level their average energy is about 4 GeV. Thus making them an excellent freely available calibration source. According to the Bethe Bloch stopping power formula written in equation 4.7 [96], the muon energy loss E is represented by dE per unit of distance dx traveled inside a material. The negative sign accounts for the energy lost. The constant K $\sim 0.307 MeV cm^2/g$, the charge of the incident muon z, the atomic number of absorbing material Z, the atomic weight of absorbing material A, the velocity of the incident particle $\beta = v/c$, the electron mass $m_e \sim 0.511 MeV/c^2$, the speed of light c, the Lorents factor $\gamma = 1\sqrt{1-\beta}$, the maximum energy transfer per collision T_{max}, the mean excitation energy I as well as the density effect correction $\sigma(\beta\gamma)$.

It predicts that an absorber with a density of $1.032 gcm^{-3}$ (e.g. the NE102A material) has a stopping power dE/dx of roughly $2.0 MeV cm^2 g^{-1}$ on a 4 GeV muon that passes through it. Therefore the average energy that such a particle will loss (mainly via ionisation) is expected to be approximately 2 MeV/cm. Equation 4.8 parameterised the energy loss in terms of dE/dx, the distance traveled Δx as well as the material density ρ. It foreseen that when high energy muons transverses vertically through a 10 cm thick NE102A plastic scintillator detector. They will deposite an average energy of more or less 24 MeV with uncertainty $\sigma(E_m)$ that is dependant on the distance travelled through the scintillator. Further the predicted value is supported by the muon energy loss distribution shown in Figure 4.8 which

confirms that muons indeed lost a mean energy of (24.1 ± 0.3) MeV when passing through the NE102A material.

$$-\frac{dE}{dx} = Kz^2\frac{Z}{A}\frac{1}{\beta^2}\left[\frac{1}{2}ln\frac{2m_ec^2\beta^2\gamma^2T_{max}}{I^2} - \beta^2 - \frac{\sigma(\beta\gamma)}{2}\right] \quad (4.7)$$

$$E_m = \frac{dE}{dx} \times \Delta x \times \rho \quad (4.8)$$

$$\frac{\sigma(E_m)}{E_m} = \frac{\sigma x}{\Delta x}.$$

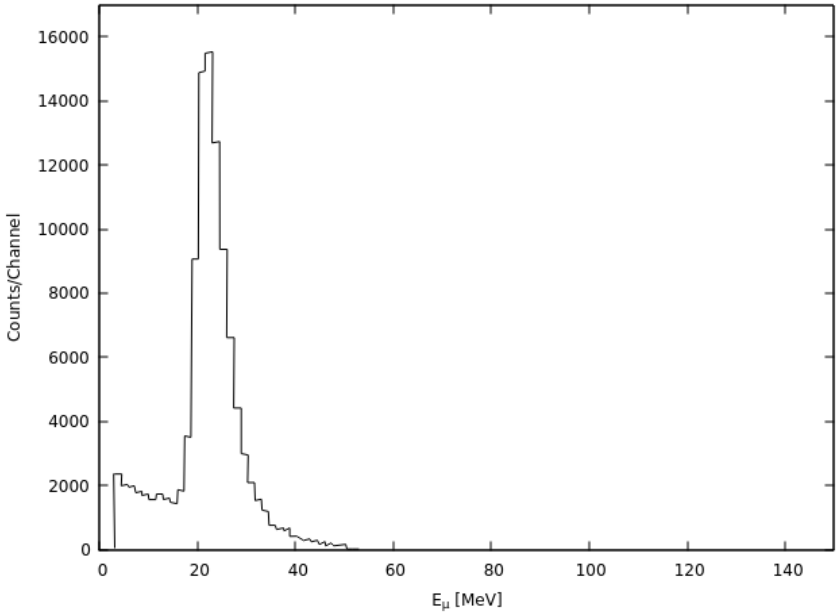

Figure 4.8: A muon energy loss spectrum measured with a NE102A plastic scintillator detector [97]. The tail on the rigth is formed when the muons suffer multiple large energy transfers during single collisions.

4.1.12 NE102A Detector Timing Circuitry

The NE102A plastic scintillator detectors provided output pulses which can be related to the emitted γ-rays and neutrons that originated from the various reaction channels. In Fig.4.09 the scintillator timing circuitry is outlined in the block diagram. These were powered with standard CAEN high voltage power supply units.

When a neutron interacts within the NE102A material the interaction produces scintillation light which is transported directly or via total internal reflection to the conical Perspex light guides. These light guides direct the light towards two photomultiplier tubes (PMT) on opposite sides of the plastic scintillator. Each PMT has an anode and dynode output points. The PMT converts the light into an electric charge signal, this signal took roughly ~ 0.9 ns to rise on an oscilloscope.

The timing signals were derived from the positive dynode output points illustrated in Fig 4.10 and were directed into the ORTEC 113 amplifiers (which were housed in a CANBERRA 2020 NIM bin power supply unit) where they were converted into voltage pulses.

Thereafter the voltage pulse was split into two parts with one going to the PIXIE16 ADCs and the other into a coincident unit in order to test for coincidence between two photomultipier tubes. From here the signals were directed into timing filter amplifier (TFA) sets via pre amplifiers. The latter devices were used as shapers to output pulses with short rise times and having exponential decay tails. The TFA's outputs were directed into twelve constant fraction discriminators (CFD) that were connected to the left and right PMT's on all the plastic scintillators detectors. Their purpose were to generate a timing signal with a fixed time between interaction, independently of the amplitude.

The CFD output signals were inspected for time coincidences with an oscilloscope after when they were confirmed to be in coincidence with each other. They were then passed to a coincidence module which determines if the CFD output is in time coincident with the RF signal. If true an output signal is generated this maybe achieved via a transmission gate or via the signal summing method. The latter method was used where the two input signals were summed together, the resultant pulse was then passed through a discriminator tuned to a height just below the sum of the two logic pulses. The discriminator is trigged whenever the amplitude of the resultant pulse is large enough. This happens when the CFD and RF signals come close in time to overlap, this time period is known as the coincidence *resolving time* and is dependant on the minimum electronics overlap and the signals widths. It must be noted that a second RF signal was directed into the TAC but was delayed by 64 ns which was achieved by using a stretcher modules. The output of the coincidence unit was fed into a time to amplitude converter where it was used as a start signal, but the delayed RF pulse was used as the TAC stop signal. The TAC output was converted into a short rise time long decay time signal before arriving at the XIA Pixie16 digital pulse processor system to be digitized.

The XIA Pixie16 system consists of a number of modules with timestamp frequency of 100 MHz, each module can accept 16 signals from any radiation detector at a sampling rate of 100 MHz. Further, each channel offset can be digitally manipulated, however their are two voltage gains any one may be selected via the relay option. Several individual modules were combined into a larger system which was housed in a PXI crate. After digitization the information was then send to the Maximum Integrated Data Acquisition System (MIDAS) [98] to be stored as raw data files for further analysis. For a more detail discussion of the XIA Pixie16 digital system and MIDAS consult Ref.[97, 99].

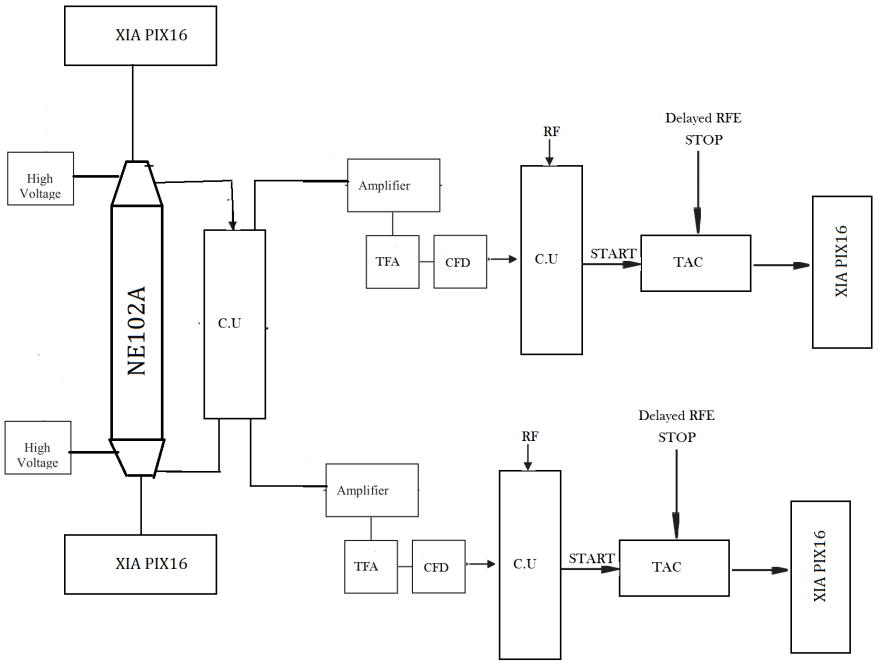

Figure 4.9: The NE102A plastic scintillator detector timing circuitry block diagram.

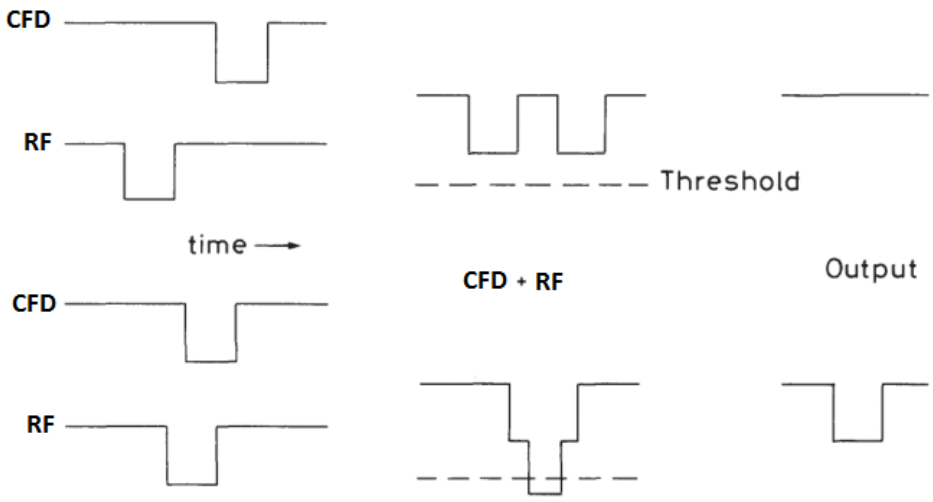

Figure 4.10: An illustration of the signal summing coincidence method at work in the C.U. module.

4.2 Overview

In this chapter the data analysis of the two proton stripping datasets will be discussed. During the off-line analysis the 2D γ-ray events were analysed with the Radware data analysis package, while those corresponding to the t-o-f were analysed with both Radware [95] and the ROOT CERN [100] analysis software.

4.2.1 ROOT Trees

ROOT is written in *C++* it is an object-oriented program and library developed by CERN [100]. It was originally designed for particle physics data analysis, but it is also used in other applications such as nuclear physics research. ROOT trees were created from the raw data files by sorting them with the SimSort code [101]. The trees are made up of nodes (i.e. branches or subdirectories) and leaves, the leaves represents variables and contain the calibrated data files.

4.2.2 Contour Plot Generation

The coincidence of a γ-ray seen in a clover detector and a neutron detected (neutron-single mode) by one of the plastic scintillator detectors made it possible to build the time-of-flight *vs* E_γ scatter plot that is shown in Fig 4.13. The latter plot was first linearised mainly to adress shape elongations that results from the electronics. Starting from the left on the contour plot the target γ-ray blob appear first, closely followed by the beam dump γ-ray blob. These are followed by the fast neutrons (black circle) and finally the statistical neutrons (grey square). Further the contour plots were used to generate the direct reaction neutron gated γ-ray spectra for ^{100}Ru and for ^{150}Sm. In order to build the 2D scatter histogram the timestamp difference spectrum between the RF and clover detectors as well as between the RF and NE102A detectors were generated.

From the aforementioned spectra two time correlated spectra were sorted for each measurement. It must be noted by taking time differences it ensures that other triggers that may be present in the raw data are eliminated. The sorted spectra are the time correlated spectrum from the timestamp difference between the neutron and clover detectors (Fig 4.11) and the time correlated spectrum between the RF and clover detectors (Fig 4.12). Each of the correlated spectra has pronounced events these correspond to prompt events that came from the target. The repeating small peaks in Fig 4.12 correspond to random events, they repeat with the cyclotron frequency of 37.0 MHz ($= \Delta\ T_{burst} \approx 270.0$ ns) and are well separated from the correlated peak. The achieved timing resolution is about $\Delta t \sim$ (15-20) ns and the prompt to random event's ratio is roughly 3:1. If the time jitter is ignored, the measured time resolution equates to the time resolution of the clover detectors.

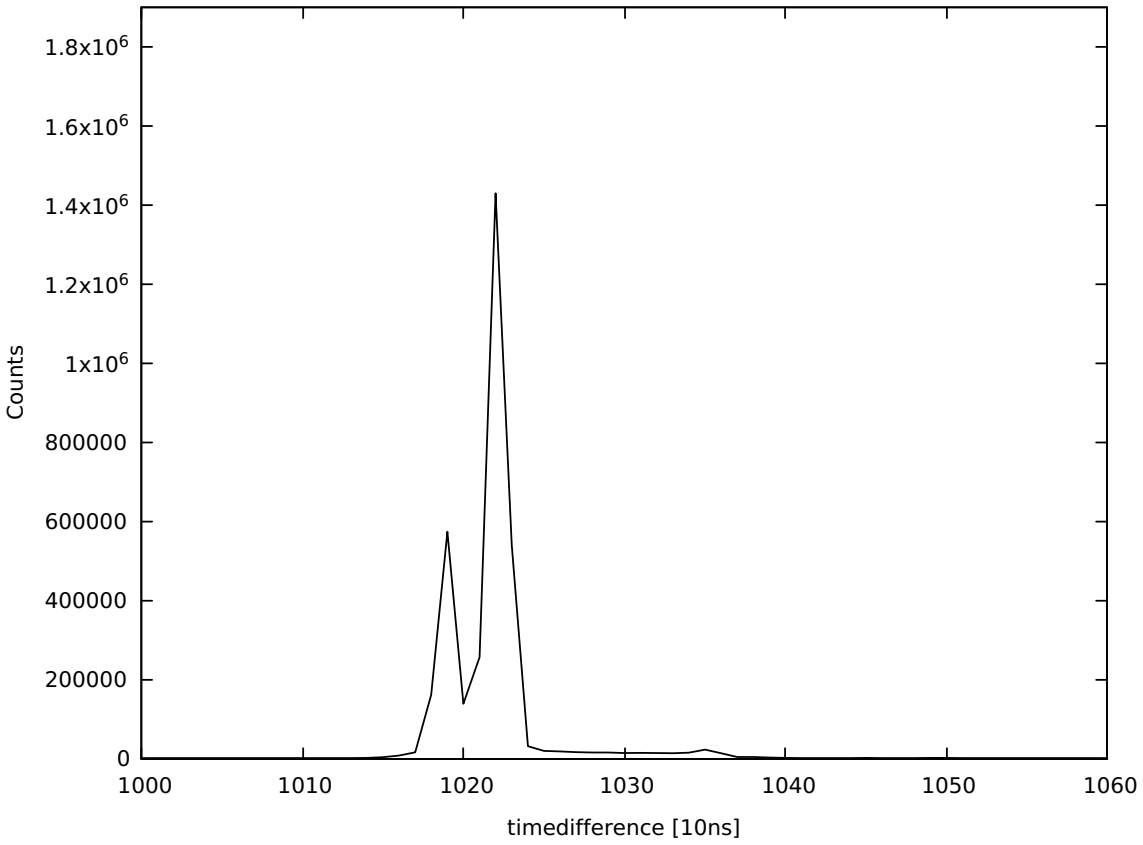

Figure 4.11: Time correlated spectrum from the time stamp difference between the neutron and clover detectors. The larger prompt peak correspond to events that came from the target while the smaller peak originates from beam dump events.

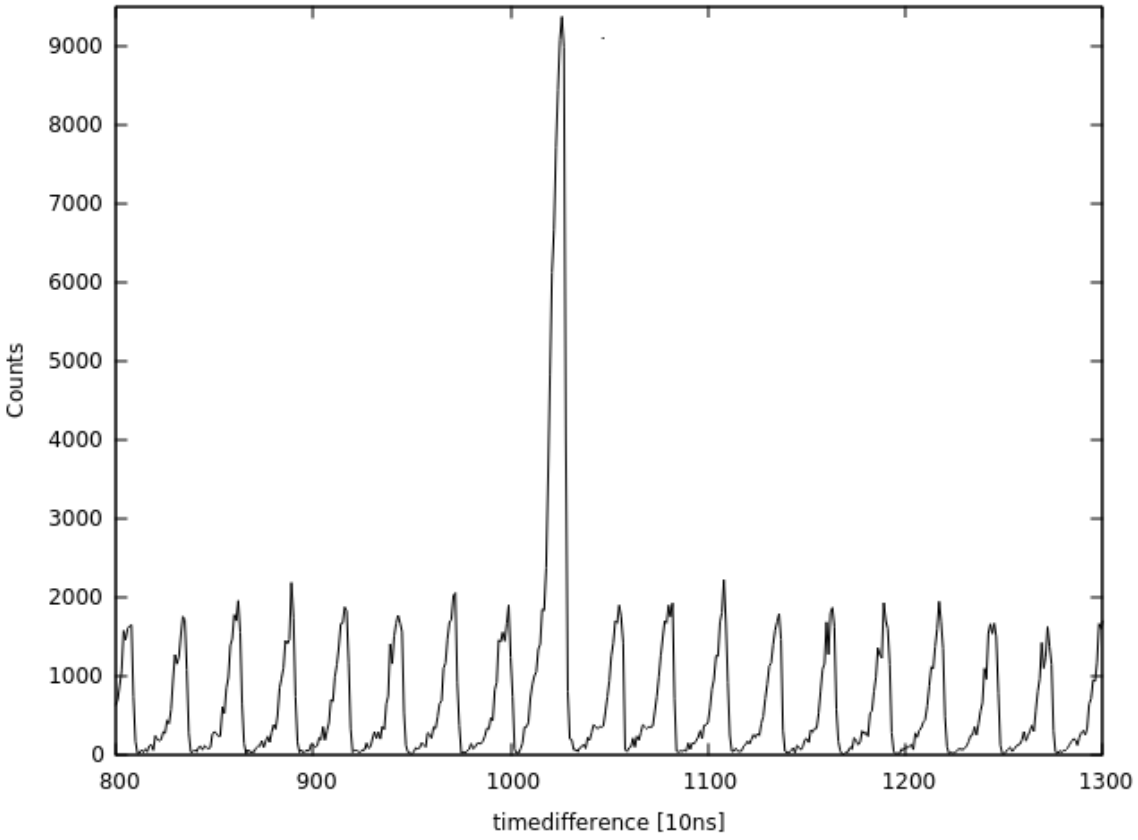

Figure 4.12: Time correlated spectrum from the time stamp difference between the RF and clover detectors. The small peaks corresponds to repeating beam burst.

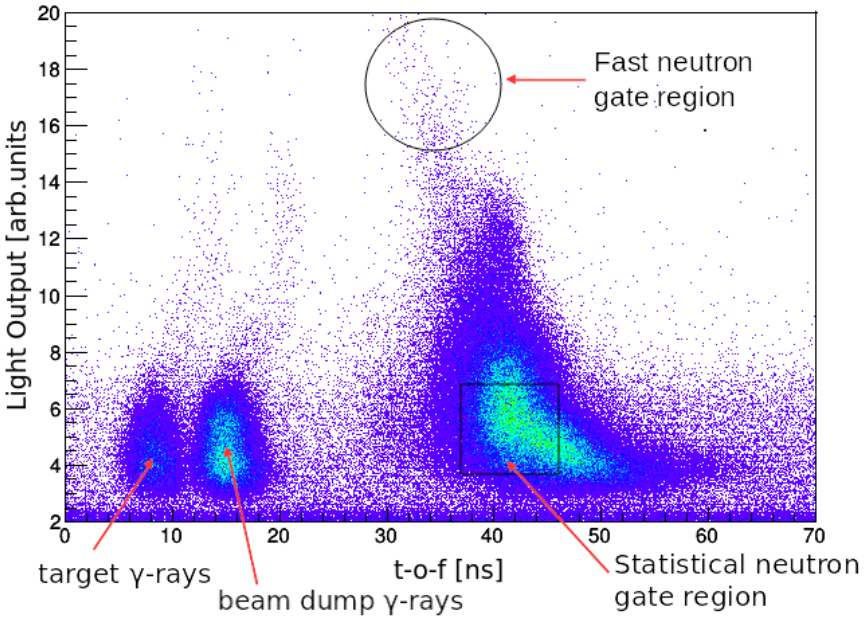

Figure 4.13: The time of flight *vs.* E_γ 2D scatter plot for the NE102A plastic scintillator detectors. Starting on the left the first locus is due to the target γ-rays, while the second one is due to the beam dump γ-rays. The direct reaction neutron region is indicated with the circle while the evaporation neutron region is labelled with the grey square.

4.2.3 Setting gates

The initial approach was to set graphical gates around the fast neutron (back circle) and statistical neutron (grey square) regions using a ROOT TCut macro. The fast neutron region is identified from the large PMT light output coming from the fast neutrons that transfer their kinetic energy to the NE102A plastic scintillator detector. The extracted γ-ray spectra were contaminated with peaks which mainly came from the strongest fusion evaporation i.e. the (^{3}He, 3nγ) and the (^{3}He, 2nγ) exit channels see panel a) in Fig.4.14.

Thereafter background statistical neutron gated γ-ray spectra were created. The counts under the peaks of the strongest contaminant transitions (i.e. the 652 keV γ-ray peak of ^{98}Ru and the 552 keV γ-ray peak of ^{148}Sm) were extracted from the neutron gated γ-ray and background γ-ray spectra by applying Gaussian fits. The extracted counts were used to calculate normalization coefficients which were applied to the background γ-ray spectra before subtraction. It can be seen that the background subtracted spectra have significantly less contaminant transitions see panel b) in Fig.4.14 and panel c) Fig.4.15. In panel b) the 406 keV transition which depopulates the $I^\pi = 0_2^+$ state at 740 keV excitation energy is part of the background. This is because the time synchronisation between the clovers and plastic scintillator detectors did not work well for the ^{150}Sm measurement. To generate panel c) shown in Fig.4.15 a narrow time gate was placed on the

fast neutrons which resulted only in the appearance of the 539 keV and 590 keV transitions. Panel d) was also generated via a narrow time gate this time placed on the 1n exite channel stastistical neutrons. It can be seen that the 590 keV transition is now much reduced whiles the low-lying yrast transitions appears. This indicates that the $I^{\pi} = 0_2^+$ spin state is largerly populated via the direct stripping of a $(0s)^2$ proton pair onto an even even ^{98}Mo target nucleus.

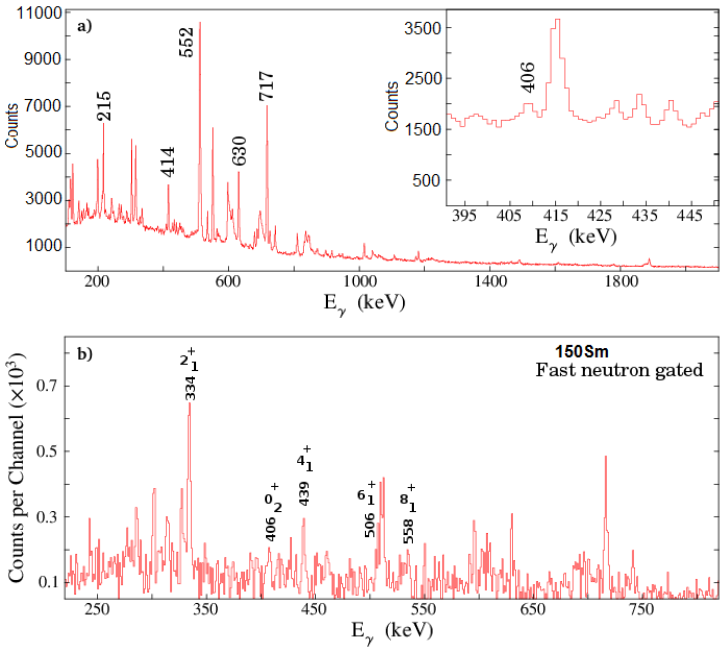

Figure 4.14: The ^{150}Sm total projection spectrum is shown in panel a) and the fast neutron γ-ray spectrum is shown in panel b). Panel b) was extracted although the time coincidences did not work well.

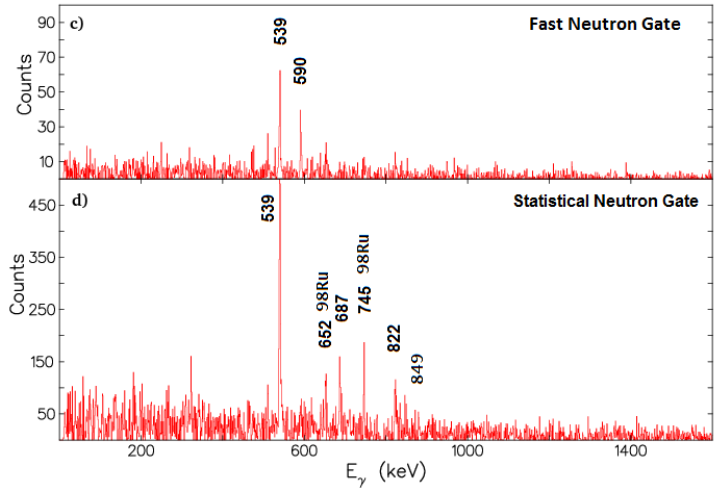

Figure 4.15: The ^{100}Ru narrow time fast neutron gated γ-ray spectrum is shown in panel c) and the tight time statistical neutron gated γ-ray spectrum is shown in panel d) here the 590 keV transition that depopulates the $I^{\pi} = 0_2^+$ state at 1130 keV excitation energy is now much reduced. This indicates that the $I^{\pi} = 0_2^+$ state is populated through direct transfer of a $(0s)^2$ proton pair to the even even ^{98}Mo nucleus.

4.2.4 Gaussian Peak Fits

The Radware programme *xmgf3* written by Radford et al., [95] was used to fit the peaks of interest in the neutron gated γ-ray and γ-γ coincidence histograms. It is a χ^2 peak-fitting program built originally to analyse γ-ray spectra, however *xmgf3* can also be used to do general purpose histogram analysis.

Xmgf3 fits a function Y which is described by equation 4.09 the function is consist of a (1) Gaussian of height H×(R/100) it is the main component of the peak which arises from the complete charge collection inside the detector, (2) a skewed Gaussian of height H×(1-R/100) accounts for events with incomplete charge collection due to crystal deffects because of neutron damage inside the detector material resulting in an exponential tail on the low-energy side and a (3) smoothed step function of height H×(Step/100) to increase the background on the low-energy side of the peak. The different constant backgrounds below and above the full peak stem from multiple interactions of one γ-ray inside the crystal where the full energy is not deposited (Compton background). The last two peak-fitting components can be set to zero if not needed.

$$\begin{aligned} Y = & \frac{H \times R}{100} \times exp\left[\frac{-(X-X_0)^2}{2\sigma^2}\right] \\ & + H \times \left[1 - \frac{R}{100}\right] \times exp\left[\frac{-(X-X_0)}{\beta}\right] \times erfc\left[\frac{(X-X_0)}{\sqrt{2\sigma}} + \frac{\sigma}{\sqrt{2\beta}}\right] \\ & + \frac{H \times S}{100} \times erfc\left[\frac{X-X_0}{\sqrt{2\sigma}} + A + B(X-X_0)\right] \end{aligned} \tag{4.9}$$

where

- Y - counts in peak
- A - a normalization factor
- R- skewed Gaussian
- X_0 - peak centroids (keV)
- σ -standard deviation
- FWHM $= 2\sqrt{2ln2}\sigma$
- *erfc*- is the complement of the error function
- X - channel number
- β-skewness of the skewed Gaussian

Before starting with the fitting analysis, it was wise to fit a few standard γ-ray source peaks over a wide energy range. In order to determine an initial set of peak shape coefficients, such that different peak shapes could be fitted similarly. For this purpose the 121.7 keV, the 344.4 keV, the 778 keV, the 1213.7 keV and the 1408 keV γ-ray peaks of ^{152}Eu were chosen as the initial fitting peaks. These peaks are well separated from other γ-ray transitions and had good statistics. Thereafter, either all the γ-ray peaks of interest can be simultaneously fitted or each peak can be fitted individually. The latter approach was adopted to first determine the peak width limits of integration and was then used with one of the initial peak shape parameters to perform the integration. The starting coefficients were varied to best fit the data, in addition linear background subtraction were also used.

4.2.5 Peak Counts and Errors

In *xmgf3* the area of the fit function is calculated by:

$$\begin{aligned}
\text{Area} &= \int_{-\infty}^{+\infty} \Big(\text{Gaussian} + \text{skewed Gaussian} \Big) dX \\
&= A \int_{-\infty}^{+\infty} \left(\left[1 - \frac{R}{100} \right] \times \exp \left[\frac{-(X - X_0)^2}{2 \times \sigma^2} \right] \right) dX \\
&+ A \int_{-\infty}^{+\infty} \left(\frac{R}{100} \times \exp \left[\frac{-(X - X_0)}{\sigma} \right] \times erfc \left[\frac{(\sigma + X - X_0}{\sqrt{2}\sigma} \right] \right) dX \\
&= A\sigma \left(\sqrt{2\pi} + \frac{2 - \sqrt{2e\pi}}{100\sqrt{e}} R \right)
\end{aligned} \tag{4.10}$$

with uncertainty

$$\frac{\sigma Area}{Area} = \sqrt{\left(\frac{\delta A}{A} \right)^2 + \left(\frac{\delta \sigma}{\sigma} \right)^2 + \left(\frac{\delta R}{R} \right)^2}. \tag{4.11}$$

The shape parameters which are listed in Table 4.3 were used in the analysis of the neutron gated γ-ray peaks of interest, they correspond to the fits with the smallest χ^2 and were used to extract the peak areas and errors by the error propagation method.

Table 4.3: Initial peak shape coefficients were derived from fitting the listed γ-ray peaks of ^{152}Eu.

E_γ[keV]	R	β	Step	χ^2
121.6	6.3	2.3	0.08	1.3
344.0	0.0	1.78	0.0	1.2
778.6	0.0	2.016	0.0	1.4
1213.7	0.0	2.221	0.0	1.25
1408.7	0.0	2.41	0.0	1.1

4.2.6 2D γ-γ Coincidence Histogram

The multiplicity distribution of all the data are plotted in Fig.4.16 it indicates that the data have a sizable amount of coincident events. Further, it can be seen that the zero-fold (neutrons), one-fold (γ-ray singles) and two-fold (γ-γ) multiplicity events are dominant while the three-fold multiplicity events are minimal, however the four-fold events are negligibly small. The two-fold events are statistically sufficient to construct two matrices with dimensions of 4096 $\times$ 4096 channels and having energy dispersion of 0.5 keV/channel and spanning the energy range up to 2 MeV. The matrices were sorted for those events that fall inside the clover clover coincidence time window .

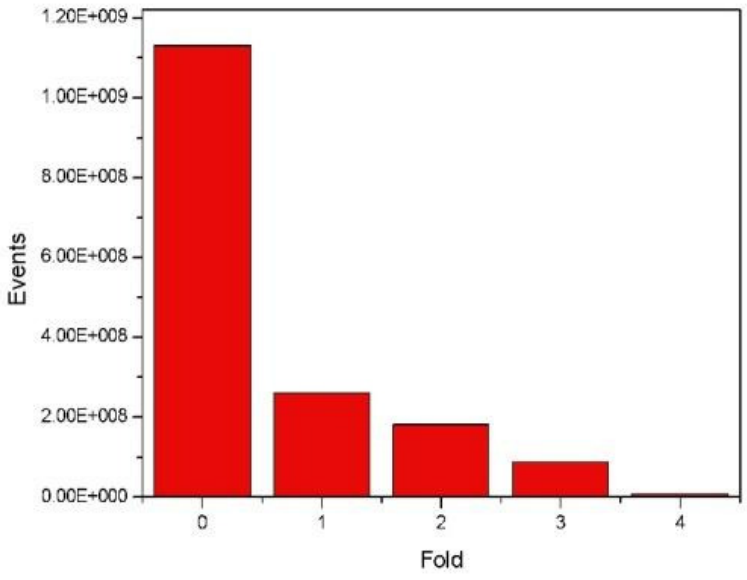

Figure 4.16: The multiplicity distribution plot of all the data indicates that most of the collected data are either zero, one, two or three fold.

4.2.7 Analysing the 2D Histogram

The γ-γ coincidence matrices were analysed with the Radware *ESCL8R* code [95]. *ESCL8R* requires a total projection spectrum which was generated by slicing the matrix with the Radware code *slice* into x and y total projections spectra. One of the two total projections spectra was used to extract a background spectrum via the *xmgf3* routine. The latter spectrum and various other (e.g. an efficiency, an energy calibration, the FWHM parameters and a γ-ray coincidence decay scheme) inputs were used to prepare the 2D γ-ray histogram for analysis. Gated spectra were extracted from the 2D histogram by making energy slices around the γ-ray peaks of interest in order to locate all γ-ray transitions that are in coincident with the primary (gated) ones see Fig.4.17 and Fig.4.18. The level scheme is built by displaying multiple gates and then visual search for new transitions these are then added to the level scheme.

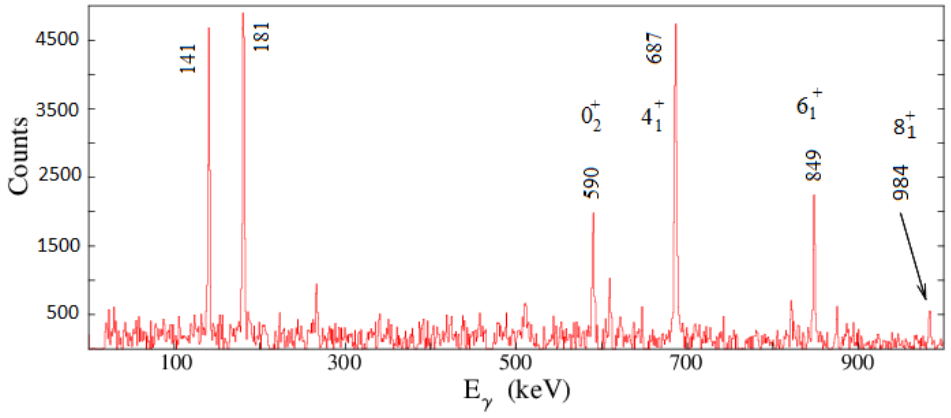

Figure 4.17: This spectrum was derived from placing a gate on the 539 keV ($2_1^+ \rightarrow 0_1^+$) ground state transition of ^{100}Ru.

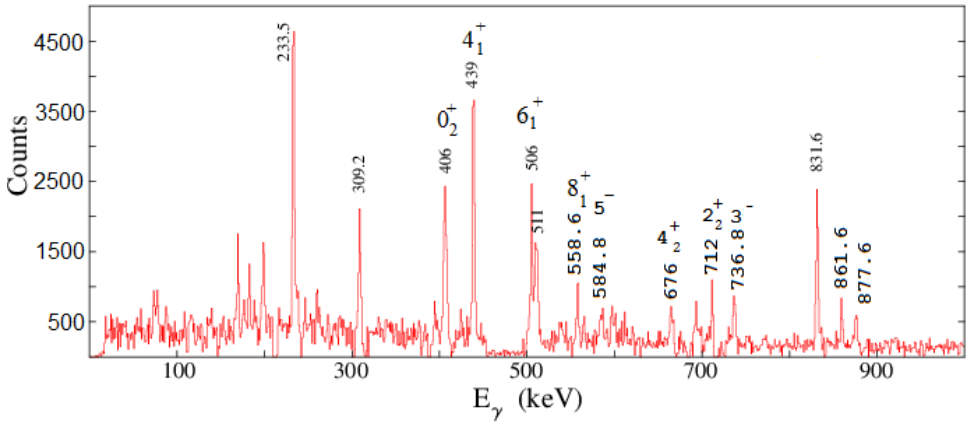

Figure 4.18: This spectrum was derived from placing a gate on the 334 keV ($2_1^+ \rightarrow 0_1^+$) ground state transition of ^{150}Sm.

4.2.8 Extracting Relative Intensities

In Table 5.1 the relative γ-γ coincident transition intensities for the ^{100}Ru isotope are listed. While in Table 5.2 those for ^{150}Sm are summarized, in both cases the relative intensity values were found by applying least-square fits directly to the 2D γ-ray data with the known level scheme used as a model. It is known that the uncertainties on the efficiency calibration and on the background subtraction will effect the fitted intensities. In addition it is also possible to find negative intensities this may occur when two or more coincident transitions are close in energy. This normally may results that one of the transitions show too large an intensity which is then balance by negative intensity obtained from one of the other transitions in the level scheme.

Chapter 5

Results

5.1 ^{100}Ru results

In Fig 5.1 the two proton stripping reaction ^{98}Mo(^{3}He, nγ)^{100}Ru relative population strength ($\sigma_{rel} \sim 13.7(1)\%$) to the $I^{\pi} = 0_2^+$ spin state of ^{100}Ru is listed amongst other strengths [104]. It was extracted by normalising the counts of the 590 keV transition to the strongest transition seen in the data of JS. Thomas *et al.*, [103]. This strength is significantly larger then this ($\sigma_{rel} \sim 0.9(0.4)\%$) strength which was extracted from the fusion evaporation reaction ^{98}Mo(α, 2nγ)^{100}Ru at a beam energy of 28 MeV and was reported by CM. Lederer *et al.*, [105]. As earlier noted the latter strength can be attributed to the fusion evaporation process. In order to determine if feeding from higher lying spin states contributed to the large relative stripping strength. A visual inspection of the 2D γ-ray data could not found any transitions that feeds the $I^{\pi} = 0_2^+$ spin state. Therefore it is concluded that the $I^{\pi} = 0_2^+$ spin state is mostly populated via the direct stripping of a $L = 0$ proton pair onto the ^{98}Mo target nucleus.

The known ^{100}Ru partial decay scheme shown in Fig.5.2 is in agreement with the one shown in Fig.5.3 for the yrast spin states up to $I^{\pi} = 8_1^+$. Further in Table 5.1 it can be seen that the present relative coincidence intensities of the yrast transitions are quite large. These were compared to those which were reported by CM. Lederer *et al* [105]. It can be seen that the yrast intensities compare very well with those from Lederer *et al* [105]. Their origins had been shown to came from fusion evaporation mechanism(see chapter 3). Finaly the coincidence technique prove to be a powerful work around to extract the relative strength for the $I^{\pi} = 0_2^+$ spin state in the absence of the measured NE102A plastic scintillator detectors efficiencies.

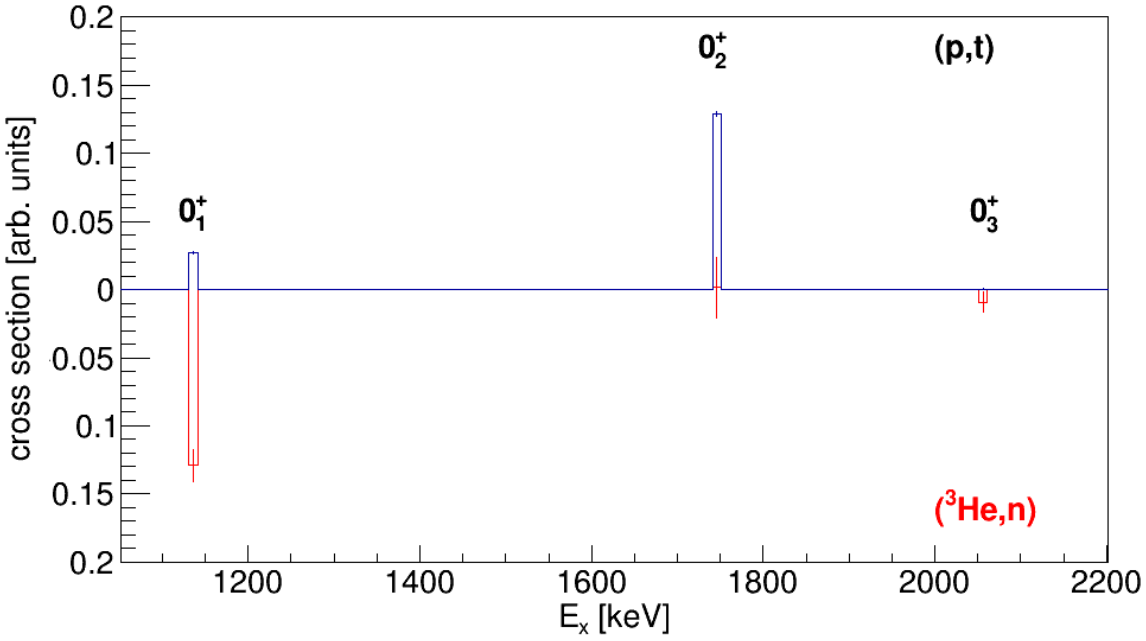

Figure 5.1: The two proton stripping reaction ^{98}Mo(^{3}He, nγ)^{100}Ru relative population strength to the $I^\pi = 0_2^+$ spin state of ^{100}Ru is plotted with the two neutron pick-up reaction strengths [104] which was reported by J.S. Thomas *et al.*, [103].

Table 5.1: The γ-ray gated coincident intensities $I_{\gamma-\gamma}$ are shown for the listed transitions of ^{100}Ru. The intensities were normalised to the $2_1^+ \rightarrow 0_1^+$ transition intensity which was set to 100. The relative intensities which were reported by CM. Lederer *et al.*, [105] were obtained from the fusion evaporation reaction ^{98}Mo($\alpha, 2n\gamma$)^{100}Ru at 28 MeV beam energy.

^{100}Ru							
E_{ex} [keV]	J_i^π	$\rightarrow$	J_f^π	E_γ[keV]	$I_{\gamma-\gamma}$	$I_{\gamma-\gamma}$[105]	Mult.
539.51	2_1^+	$\rightarrow$	0_1^+	539.10(4)	100.00(10)	100.00()	E2
1130.31	0_2^+	$\rightarrow$	2_1^+	590.55(13)	13.07(1)	0.9(0.4)	E2
1226.46	4_1^+	$\rightarrow$	2_1^+	686.72(4)	84.13(12)	86(3)	E2
2077.11	6_1^+	$\rightarrow$	4_1^+	849.14(5)	54.72(11)	63(3)	E2
3059.50	8_1^+	$\rightarrow$	6_1^+	984.50(14)	22.61(12)	25(2)	E2

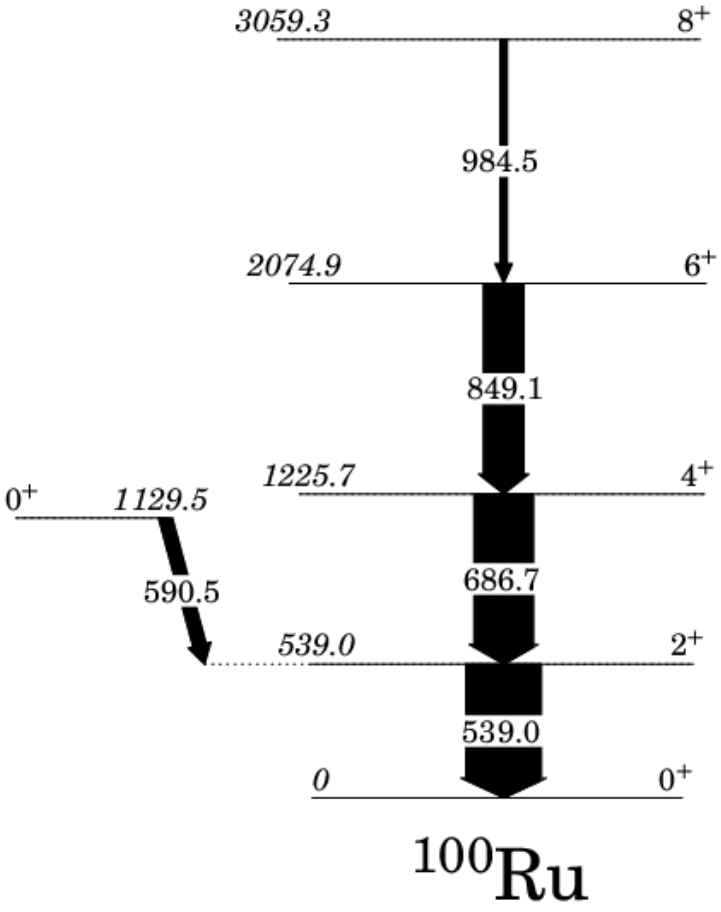

Figure 5.2: The partial decay scheme of ^{100}Ru includes the γ-ray transitions that are listed in Table 5.1. The arrows represent the γ-ray transitions having energies labelled in keV, while their width denotes their relative intensities.

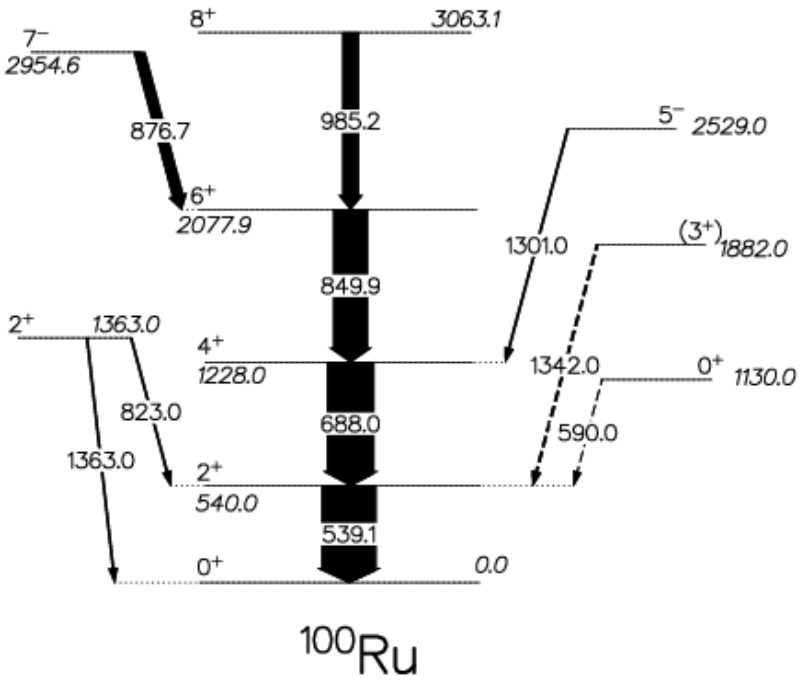

Figure 5.3: The ^{100}Ru partial γ-ray decay scheme was extracted from the fusion evaporation reaction ^{98}Mo$(\alpha, 2n\gamma)^{100}$Ru at 28 MeV beam energy and reported CM. Lederer *et al.*, [105]

5.2 ^{150}Sm results

As previously pointed out since the present ^{150}Sm direct reaction data is not well time correlated no meaningfull conclusions could be reached from the results. Earlier in a related measurement WP. Alford *et al.*, [80] investigated the nature of the $I^{\pi} = 0_2^+$ spin state that is position at 0.740 MeV excitation energy in the γ-ray level scheme via this ^{148}Nd (^{3}He, nγ)^{150}Sm reaction. At beam energy of E_{lab} = 25.0 MeV measured for $\theta_{lab} = 0^{\circ}$ using a 9 meter flight path and a time resolution of 1 ns 500 keV. The latter spin state was previously seen in the (p, t) reaction conducted by P. Debenham *et al* [106]. However WP. Alford *et al.*, could not found such a spin state. At first glanced it seems the data (see Figure 5.4) represents an opportunity to obtain information on the low-lying yrast spins states via fitting the line shape of the low resolution t-o-f histogram. However such a procedure is challenging and plague with uncertainties on the data digitization, on the excitation energy calibration and on the background subtraction amongst others therefore it was not attempted.

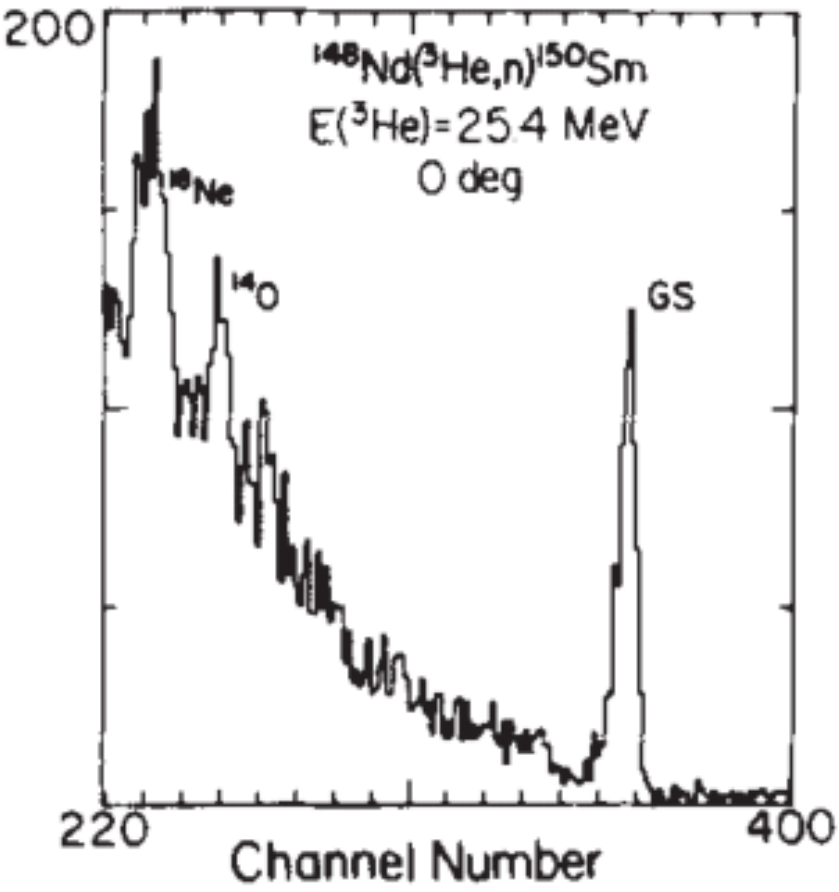

Figure 5.4: This direct ^{148}Nd(^{3}He, nγ)^{150}Sm reaction was carried out using a 25.4 MeV ^{3}He beam at zero degrees with respect to the beam axis, the neutron t-o-f distribution was reported by WP. Alford *et al.*, [80].

5.2.1 ^{150}Sm 2D γ-ray results

Again the present γ-γ coincidence data (Fig.5.5) are in agreement with the known yrast transitions shown in the partial decay scheme of Fig 5.7. Further Table 5.2 shows that the listed relative intensities for the yrast transitions as well as that of the $I^{\pi} = 0_2^+$ spin state compares well to those which were reported by JV. Thompson *et al* [107] for the fusion evaporation measurement ^{148}Nd(α, 2nγ)^{150}Sm at 22 MeV beam energy.

An inspection of the 2D γ-ray data reveals that the $I^{\pi} = 0_2^+$ spin state is fed by the 1223 keV transition which is shown in Fig.5.6. It's intensity was taken in account when the final intensity for the $I^{\pi} = 0_2^+$ spin state was extracted. Furthermore JV. Thompson *et al.*, [107] reported a 407.41 keV transition that is close in energy to the 405.58 keV transition. The former transition depopulates the I^{π}= 7_1^- level at 1.764 MeV excitation energy in Fig 5.7, however it was not observed.

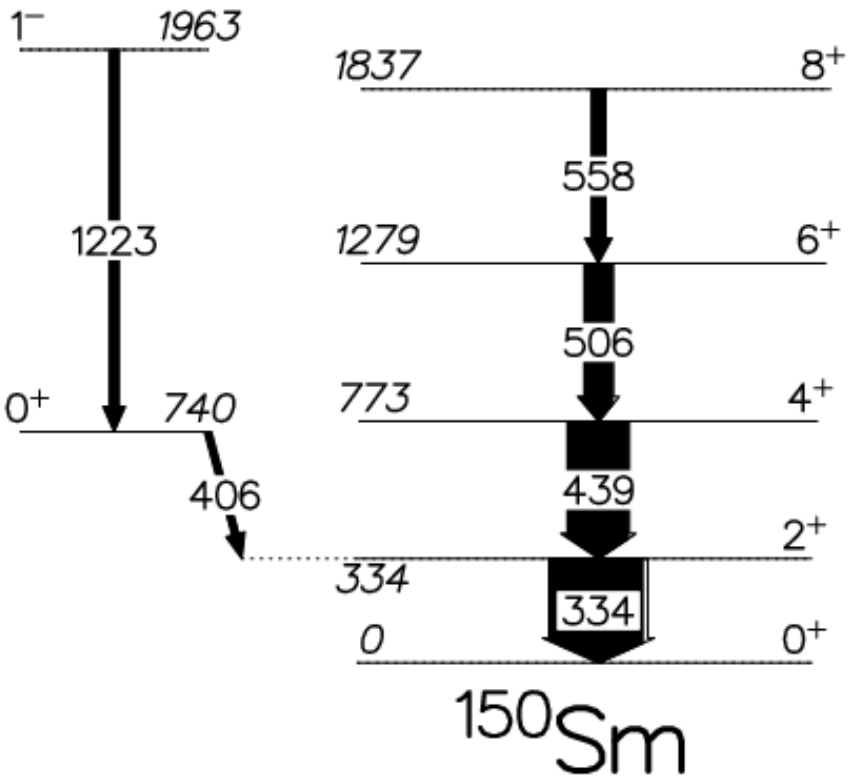

Figure 5.5: The partial decay scheme of ^{150}Sm was deduced from the γ-γ coincidence data.

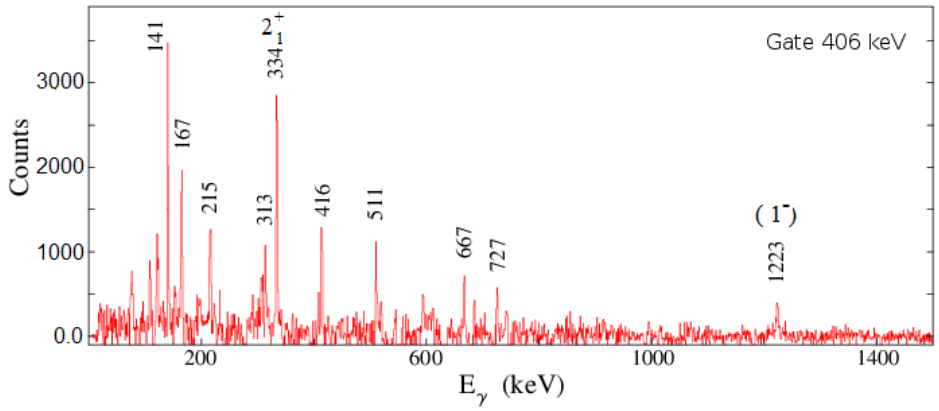

Figure 5.6: The gated 406 keV ($0_2^+ \rightarrow 2_1^+$) transition spectrum of ^{150}Sm. The 1223.26 keV transition that feed the $I^\pi = 0_2^+$ spin state at 740 keV excitation energy is clearly visible.

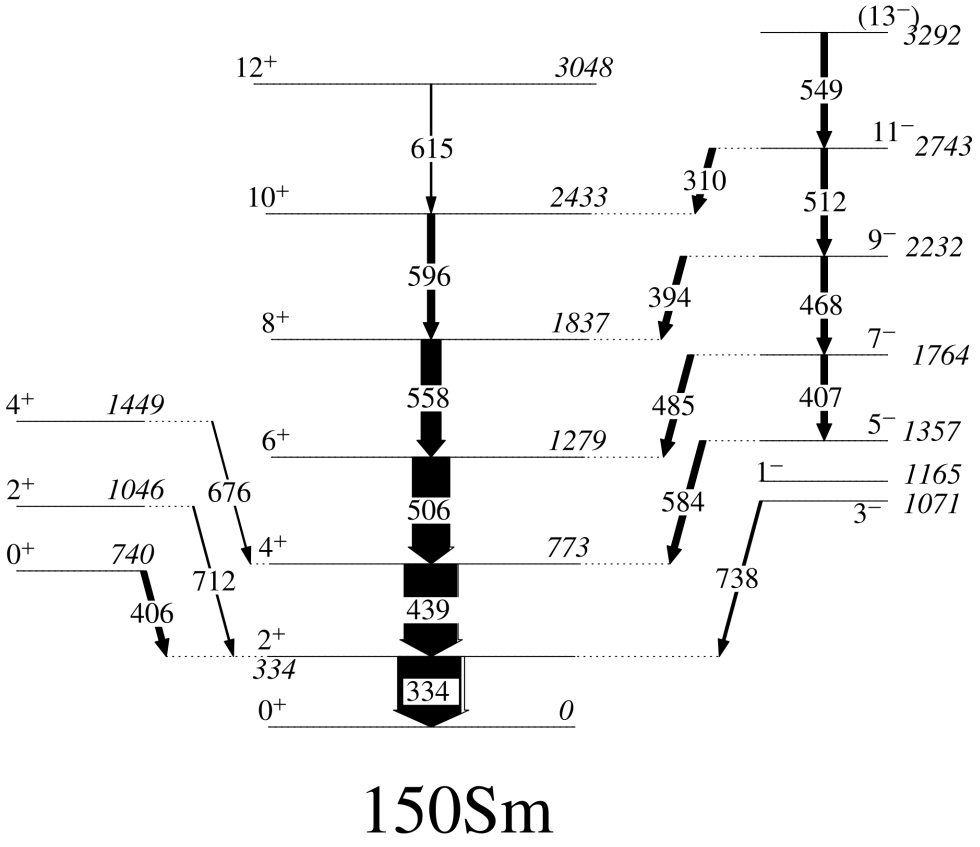

Figure 5.7: The ^{150}Sm γ-ray decay scheme was extracted from the fusion evaporation reaction ^{148}Nd$(\alpha, 2n\gamma)^{150}$Sm at 22 MeV beam energy and reported by JV. Thompson *et al.*, [107].

Table 5.2: The $I_{\gamma-\gamma}$ coincident intensities were extracted from Fig.4.18 for the listed transitions of ^{150}Sm. The intensities were normalised to the $2_1^+ \rightarrow 0_1^+$ transition intensity which was set to 100 and are compared to those that were reported by JV.Thompson *et al.*, [107].

^{150}**Sm**							
E_{ex}[keV]	I_i^π	$\rightarrow$	I_f^π	E_γ[keV]	$I_{\gamma-\gamma}$	$I_{\gamma-\gamma}$[107]	Mult
333	2_1^+	$\rightarrow$	0_1^+	333.70(4)	100.0(10)	100	E2
740	0_2^+	$\rightarrow$	2_1^+	406.58(2)+ 407.41(3)	10(8)a	9.1(5)	E2+M1
773	4_1^+	$\rightarrow$	2_1^+	439.08(5)	85.77(12)	80(4)	E2
1279	6_1^+	$\rightarrow$	4_1^+	505.36(6)	65.41(11)	58(3)	E2
1837	8_1^+	$\rightarrow$	6_1^+	558.14(11)	28.81(14)	31(2)	E2
1963	(1^-)	$\rightarrow$	0_2^+	1223.01(14)	10.1(12)		E1

The intensity contribution of the 1223.01 keV transition was subtracted from the 406 keV transition.

Chapter 6

Discussion

6.1 ^{100}Ru

The ^{100}Ru nucleus is located at the fringes of sphericity with Z = 44 which is six protons away from the Z = 50 shell closure, while the neutron Fermi level are located six neutrons away from the N = 56 shell closure. ^{100}Ru has a $I^{\pi}= 0_2^+$ spin state at E_{ex} = 1.130 MeV excitation energy this spin state shows unusual properties. In the present two proton stripping reaction measurement (^{3}He, nγ) on an even-even ^{98}Mo target nucleus it was populated with a relative strength value of $\sigma_{rel} \sim 13.7(1)\%$.

Recently Thomas *et al* performed a two neutron pickup measurement ^{102}Ru(p, t)^{100}Ru where the $I^{\pi} = 0_2^+$ spin state was populated with an absolute strength of $\sigma_{rel} \sim 3\%$ compared to the ground state strength [103]. Also in the single nucleon transfer reactions ^{101}Ru(p, d)^{100}Ru and ^{99}Tc(^{3}He, d)^{100}Ru the $I^{\pi} = 0_2^+$ spin state was populated with negligible strengths [108]. However in the single neutron stripping reaction measurement ^{99}Ru(d, p)^{100}Ru [109] the $I^{\pi} = 0_2^+$ spin state has a large cross section, but it has a relative large Coulomb excitation cross section [111]. It must be noted that the nature of the $I^{\pi} = 0_2^+$ spin state is still an open question. The $I^{\pi} = 0_2^+$ spin state was initially considered to be one of the two quasiphonon triplet member states base on excitation energy arguments. However the vibrational picture breaks down because both the experimemtal B(E2; $0_2^+ \rightarrow 2_1^+$)/B(E2; $2_1^+ \rightarrow 0_1^+$) ratio and also the B(E2; $0_2^+ \rightarrow 2_1^+$) transition probability are roughly two times smaller than the spherical phonon model predictions [110].

Van Isacker and Puddu attempted Interacting Boson Model (IBM)-2 calculations but they failed to reproduced the level energies and B(E2; $2_1^+ \rightarrow 0_2^+$) values for the $I^{\pi} = 0_2^+$ spin state [111]. They suggested mixing of coexisting shapes resulting from an intruder configuration to account for the properties of the $I^{\pi} = 0_2^+$ spin state. Similarly General Collective Model (GCM) calculations were performed by Troltenier *et al* their results predicting a coexisting spherical ground and a triaxial deformed (β, γ) $\sim$ (0.42, 24^0) $I^{\pi} = 0_2^+$ spin state [112]. According to Van Isacker

and Puddu an intruder state can arise due to proton 2p-2h excitations across the Z = 50 closed shell, as in the case of the Cd isotopes. The interaction of the additional proton 2 valence particles and 2 valence holes with the neutrons in the open 50-82 shell and the gain in the correlation energy results in the appearance of the deformed rotational-like band in the low-excitation energy region [113].

Transitions from this structure to the ground state band are forbidden or strongly retarted unless there is configuration mixing. In such a case a strong electric monopole transition strength $\rho^2(E0; 0_2^+ \rightarrow 0_1^+$ from the $I^\pi = 0_2^+$ spin state to the ground state is expected. Woods *et al.*, [114] reported large absolute $\rho(E0)$ strength values $\rho^2(E0; 0_2^+ \rightarrow 0_1^+) \sim 53 \times 10^{-3} - 185 \times 10^{-3}$ for nuclei in the A $\sim$ 100 mass region with a very large value of $\rho^2(E0; 0_2^+ \rightarrow 0_1^+) \sim 120 \times 10^{-3}$ for ^{102}Mo where the $I^\pi = 0_2^+$ spin state at 697 keV excitation energy is attributed to shape deformation [113]. In ^{100}Ru a relatively weak electric monopole reduced transition probability with a strength of $\rho^2(E0; 0_2^+ \rightarrow 0_1^+) \sim 6.1 \times 10^{-3}$ was reported for the $I^\pi = 0_2^+$ spin state [114]. This result suggests very little mixing between the spherical ground state and the assumed deformed $I^\pi = 0_2^+$ spin state or there must be small differences between their radii.

It is presently proposed that the $I^\pi = 0_2^+$ spin state has a non-collective origin, this claim is based on the electric quadrupole reduced transition probability B(E2, $2_1^+ \rightarrow 0_2^+$) strength which was extracted from a double E2 Coulomb excitation measurement reported McGowan *et al.*, [110]. They reported an upper value of B(E2, $2_1^+ \rightarrow 0_2^+$) $\leq 2.3 \times 10^2 e^2 fm^4$ which is in agreement with the single particle strength estimate B(E2, $2_1^+ \rightarrow 0_2^+$) $\sim 2.56 \times 10^2 e^2 fm^4$ obtained from the $B(E2)_{s.p} = (e^2/4\pi)|3/5R_0^2|^2$ relation where $R_0 = 1.2 \times A^{1/3}$ fm. This structure may be interpretated as a proton pairing isomer, which is a seniority zero two particle-two hole shell model state that is formed when there exists a steep oblate upsloping high-Ω Nilsson orbital close to the Fermi surface. The features of a neutron pairing isomer as recorded in the actinide region [45, 46] shows a strong (p, t) population strength, with large differences between its (p, t) and (t, p) reaction population strengths.

The first evidence in support of the proton pairing isomer claim is that the proton Fermi surface there exist a few downsloping prolate Nilsson orbitals on which the ground state is built. There is also a steep upsloping oblate high-Ω Nilsson [404] $9/2^+$ orbital extruded to the Fermi surface by the deformation see Fig.9.1. This orbital originates from the $\pi g_{9/2}$ shell model level, it was previously identified in ^{99,100}Zr[50, 115] and recently in ^{97}Sr [116] where it stabilizers the large prolate deformation for N$\sim$ 60 nuclei. The second piece of evidence is the relatively large two proton stripping reaction strength value of $\sim$ 37.71(8) with respect to the $I^\pi = 2_1^+$ spin state which was found in the present measurement.

Apart from the proposed proton pairing isomeric state at 1130 keV excitation energy. The two neutron pick-up ^{102}Ru(p, t)^{100}Ru [103] results suggest that the $I^\pi = 0_3^+$ spin state at 1742 keV excitation energy may be a neutron pairing isomeric state, since it is populated with a strength of $\sim$ 12.9% relative to the ground state

strength. If true it will be the first nucleus, according to our knowledge, that has both proton and neutron pairing isomers.

6.2 ^{150}Sm

Abdulvagabova, Ivanova and Pyatov [117] suggested that pairing isomers should not only be confined to the actinides isotopes but should also be a feature in other mass regions. Like for instance the shape transitional region of A $\sim$ 150. This region is at the start of a major neutron shell where down-sloping prolate orbitals predominate. While the oblate levels have a lower density of upsloping trajectories on the prolate side of the Nilsson diagram (see Fig 9.1). One example of a steep upsloping oblate high-Ω Nilsson orbital that is close to the neutron Fermi surface is the $\nu[505]11/2^-$ level that comes from the $1\nu h_{\frac{11}{2}}$ shell model level. Peterson and Garret [118] found that this orbital has a occupational probability of $V^2 > 0.5$ and a reduced off-diagonal pairing matrix element with nearby prolate orbitals that can result in the formation of pairing isomers, such states were recently found in the N=90 ^{154}Gd [50] and ^{152}Sm [51] isotones. In addition this orbital was recently identified in ^{155}Gd [119] where it is Pauli blocked and thereby preventing the $I^\pi = 0_2^+$ spin state in the core ^{154}Gd nucleus to couple with it.

It is probable that the $I^\pi = 0_2^+$ spin state in ^{150}Sm is also based on the $\nu[505]11/2^-$ orbital since this nucleus has N=88 neutrons which is only two neutrons fewer than the total amount of neutrons found in ^{152}Sm. The $I^\pi = 0_2^+$ state shows unusual properties, namely it has an enhanced two neutron pick-up reaction ^{152}Sm(p, t)^{150}Sm strength of $\sim$ 82%, and a two neutron stripping reaction ^{148}Sm(t, p)^{150}Sm strength of $\sim$ 25% relative to the ground state [30]. It is weakly populated in single-nucleon transfer reactions [120] and was not observed in the present two proton stripping ^{148}Nd(^{3}He, nγ)^{150}Sm measurement as well as in the measurement reported by WP. Alford *et al* [80]. Apart from the aformentioned problems the population of a proton $I^\pi = 0_2^+$ spin state is not supported by the current pair isomer hypothesis because of the non-availability of a steep upsloping oblate high-Ω Nilsson orbital that is close to the proton Fermi surface. Further, there is a weak electric monopole $\rho^2(E0; 0_2^+ \rightarrow 0_1^+) \sim 18(2) \times 10^{-3}$ transition [114]. An even smaller electric monopole transition of $\rho^2(E0; 0_2^+ \rightarrow 0_1^+) \sim 0.7(0.4) \times 10^{-3}$ has been reported for the $I^\pi = 0_3^+$ neutron pairing isomeric state with 1083 keV excitation energy in ^{152}Sm [50].

It was initially suggested that the strong two neutron pickup reaction strength (p, t) to the $I^\pi = 0_2^+$ spin state may be explained in terms of mixing and coexistence of a spherical ground and a β deformed $I^\pi = 0_2^+$ spin state [106]. A set of properties was suggested by Garret [122] for the $I^\pi = 0_2^+$ spin states belonging to the rare earth nuclei near N = 90 should have in order for them to qualify as β vibrational states. Enhancements in the interband B(E2; $0_2^+ \rightarrow 2_1^+$) values of between 12 - 33 W.u. or conversely B(E2; $2_1^+ \rightarrow 0_2^+$) values of between 2.5 - 6 W.u. should exist. Further there must be a large reduced electric monopole decay strength

$\rho^2(E0; 0_2^+ \rightarrow 0_1^+)$ value of between 85×10^{-3} to 230×10^{-3} from the β vibrational band head to the ground state. There must be closely-spaced rotational spin states with enhanced electric quadrupole transitions probabilities connecting the band members which are built on the β-deformed state. In addition enhancements are also expected in its inelastic electron scattering and Coulomb excitation cross sections, while no such effects are expected in its single and two-nucleon transfer reactions strengths [124, 125]. An examination of the listed properties does not support the idea that the $I^\pi = 0_2^+$ spin state at 740 keV excitation energy is a β vibrational state.

It is proposed that the $I^\pi = 0_2^+$ spin state is base on a neutron two particle-two hole configuration also known as a pairing isomeric state. This is based on the large asymmetry in the two-neutron transfer reaction population strengths, the large two-neutron pickup reaction strength, the small single-neutron transfer reaction population strength, the availability of the steep upsloping oblate high-Ω Nilsson $\nu[505]11/2^-$ level at the neutron Fermi surface. This orbital is a polar orbital, its energy increases as a function of deformation and it has a large negative static intrinsic quadrupole moment compared with the strong down-sloping prolate orbitals around the Fermi surface.

Peterson and Garret [119] reported that the off diagonal pairing matrix elements $G_{op} = G_0 - G_2|q_{v_o} q_{v_p}|$, that correlate the movement of a neutron pair from a prolate to the oblate $\nu[505]11/2^-$ Nilsson level is much smaller than the matrix elements which pairs of particles moving in Nilsson states showing the same sign of the intrinsic quadrupole moment $G_{oo} \approx G_{pp} = G_0 + G_2|q_{v_o}|^2 \gg G_{op}$. Hence it is possible to distinguish between two groups of single-particle states which are almost completely uncoupled from each other. The $I^\pi = 0_1^+$ ground state which is predominately based on the orbitals with positive values of the quadrupole moment and the $I^\pi = 0_2^+$ spin state which is based on two-neutrons that move in the steep upsloping oblate high-Ω Nilsson $\nu[505]11/2^-$ level.

Lastly if the two $I^\pi = 0^+$ states were due to shape coexistence and mixing, then the ratio of their populations would depend only on the mixing and would be the same for two neutron and two proton stripping or pick-up reactions, which is clearly not the case.

6.3 Summary and Conclusion

The aim of this work was to investigate the intruder state hypothesis that was put forward by P. van Isacker and G.Puddu in order to account for the small B(E2, $2_1^+ \rightarrow 0_2^+$) values that was found for the the $I^\pi = 0_2^+$ spin state of ^{100}Ru. Although a strong $L = 0$ proton pair transfer transition to the $I^\pi = 0_2^+$ spin state was observed and shell model calculations indicates that the latter spin state has a dominated proton pair character. It was not possible to associate it with an intruder state, since its properties does not match does of an intruder state. For example this

nucleus does not have a proton shell closure etc. Based on its other observed properties this structure was further interpreted to be closely associated with a proton pair isomer, meaning pair isomers are more widespread than previously believed. This result is not only limited to the field of nuclear structure research but can also be used to better understand the nature of the anti-neutrino is it a Dirac or a Majorana particle once $0\nu2\beta$-decay is discovered. It is not possible to draw any conclusions for the $I^{\pi} = 0_2^+$ spin state of ^{150}Sm, since technical problems were experienced during the measurement.

Another interesting result was the observation of strongly populated low-lying yrast spin states up to $\leq I^{\pi} = 8_1^+$ for both nuclei. These were suggested to be caused by multistep reaction mechanismes, however this hypothesis is not supported by coupled channels code calculation results. Even statistical model codes calculation results indicates that the single neutron exit channels should be populated very weakly. However the GEANT4 NE102A plastic scintillator detectors efficiency simulations indicates large efficiencies for the most probable neutron emission energies that originates from the 1n exit channel. Based on the latter information it is concluded that the strongly populated low-lying yrast spin states are due to fusion evaporation.

6.4 Future Work

The main deficiency of this work was the lack of target thickness and beam current information as well as the $I^{\pi} = 0_1^+$ ground state was not directly being measured the latter needs to be determine as well as the experimental NE102A plastic scintillator detectors efficiencies.

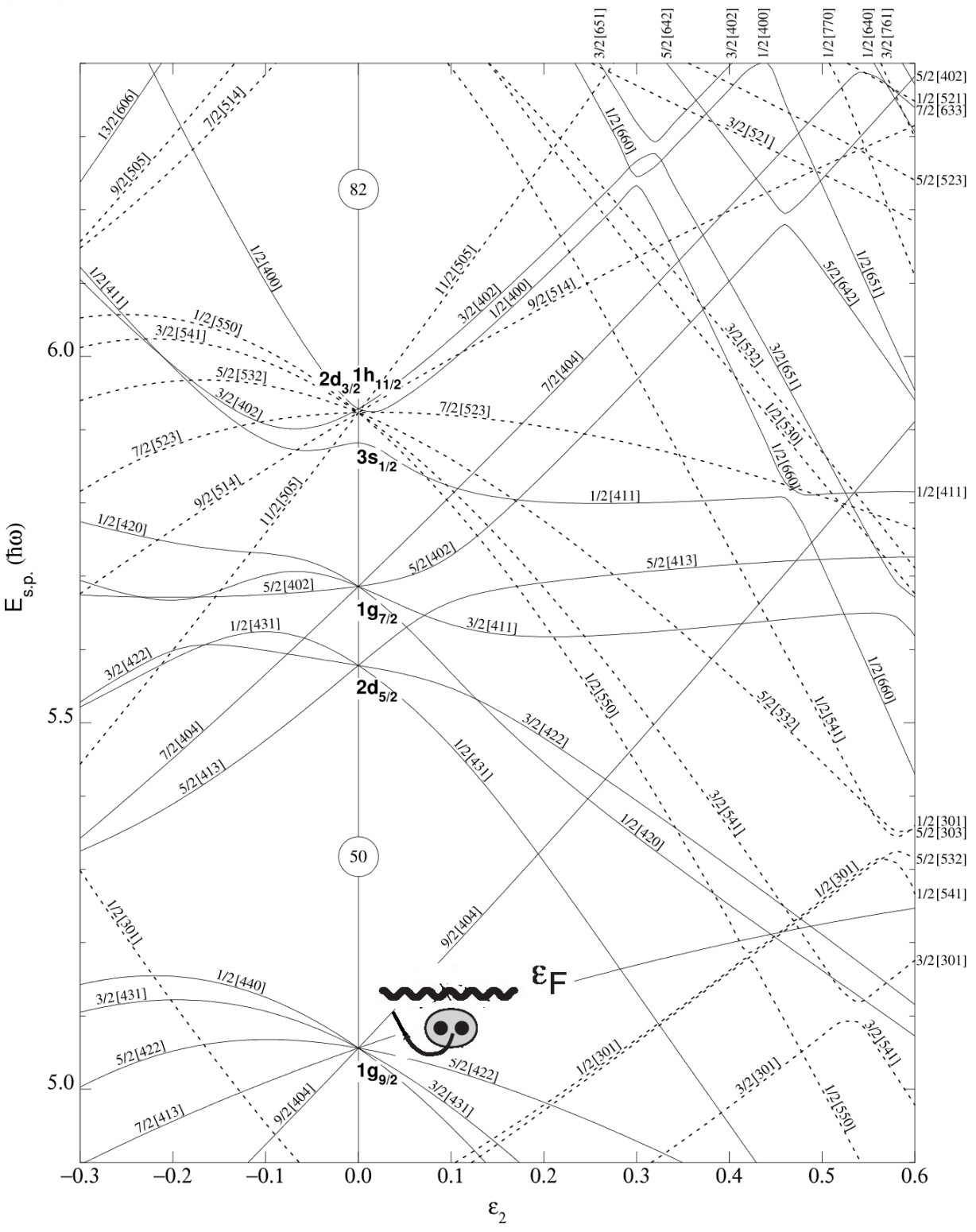

Figure 6.1: Nilsson single particle energies levels versus quadrupole deformation. The illustration depicts the scattering of a proton pair out of a ground state orbital into the $\pi[404]9/2^+$ level giving rise to the $I^\pi = 0_2^+$ state.

Bibliography

[1] https://en.wikipedia.org/wiki/Double beta decay

[2] M.Goeppert-Mayer Physical Review, vol. 48, no.6, pp.512 516,1935.

[3] S.R. Elliott, A. A. Hahn, and M. K. Moe,Physical Review Letters, vol. 59, no. 18, pp. 2020-2023, 1987.

[4] B.Lehnert EPJ Web of Conferences 93,01025 (2015)

[5] https://science.energy.gov/ /media/np/nsac/pdf/docs/2014/NLDBD Report 2014 Final.pdf

[6] J.Barea, F.Iachello, Phys. Rev.C 79, 044301 (2009).

[7] E.Caurier et al., Rev. Mod. Phys. 77, 427 (2005).

[8] V.A Rodin et al., Phys. Rev.C 68, 044302 (2003), Nucl.Phys. A,Nucl.Phys.A 766, 107 (2006) and erratum Nucl.Phys A. 766 107 (2006)

[9] Simkovic et al. ; Phys. Rev. C 77, 045503 (2008); F. Phys. Rev. C 79 055501 (2009).

[10] E.Majorana, (1937)."Teoria simmetrica dell'elettrone e del positrone". Il Nuovo Cimento (in Italian). 14 (4): 171ĭ013184. doi:10.1007/BF02961314

[11] W.H.Furry, (1939). "On Transition Probabilities in Double Beta-Disintegration". Physical Review. 56 (12): 1184ĭ0131193. Bibcode:1939 PhRv...56.1184F. doi:10.1103/PhysRev.56.118

[12] T. Bloxham et al., Physical Review C 82, 027308 (2010) and reference therein.

[13] L. De Braeckeleer, M. Hornish, A. Barabash, and V. Umatov Phys. Rev. Lett. 86, 3510 Published 16 April 2001.

[14] Introductory Nuclear Physics by Kenneth S. Krane (John iley Sons 1987)

[15] A Bohr and B.R. Mottelson 1975 Nuclear Structure Vol II (READING, MA: Benjamin-Cummings)

[16] Peter Ring Peter Schuck The Nuclear Many-Body Problem Series ISSN 1864-5879 1980.

[17] S.G.Nilsson and O.Prior Mat.Fys. Medd. Dan Vid. Selsk 32 no.16 (1961)

[18] A. Bohr, B.R. Mottelson and D. Pines Phys. Rev 110. 936 1958

[19] D.R.Bes and R.A.Broglia,Phys.Rev.Lett.25;302 (1976).

[20] D.Carbone et al., Journal of Physics Conference Series 312 (2011) 082016.

[21] G. Racah et al., Phys Rev.62 438

[22] M.G. Mayer. Phys. Rev., 78 (1950), p. 22.

[23] J.Bardeen, L. N. Cooper, and J. R. Schrieffer. Phys. Rev. 108, 1175 1 December 1957

[24] S.Belyaev et al., Mat. Fys. Medd. Dan. Vid. Selsk. 31. 641. 1959.

[25] A.Migdal et al., Nucl. Phys. 13 655, Sov. Phys. JETP 10, 176 1959.

[26] L.S Kisslinger and R.A. Sorensen Mat. Fys. Medd.Dan. Vid. Selsk.32. no.9 1960

[27] Bogoliubov, N. N. (1958). A new method in the theory of superconductivity. i. Soviet Physics JETP, 34:41 46.

[28] S.Yoshida et al., Nucl. Phys A33.

[29] G.Racah and Talmi Phys. Rev.89.913 1953.

[30] J.H.Bjerregaard et al., Nucl. Phys.A 110 1(1968).

[31] J.H. Bjerregaard et al., Nucl. Phys. A103 (1967) 33

[32] J.B. Ball et al., Phys. Rev. C4 (1971) 196

[33] J.H. Bjerregaard et al., Nucl. Phys. A131 (1969) 481

[34] M.Oothoudt et al., Phys. Letters 32B (1970) 270

[35] G.Igo et al., nnals of Physics 66 (1971) 60

[36] D.R.Bes et al., Nucl. Phys. 80 (1966) 289

[37] R.A.Broglia et al., Nucl. Phys. A115 (1968) 273

[38] E.R.Flynn et al., Nucl.Phys A154 (1970) 225

[39] J.H.Bjerregaard et al; Nucl. Phys. A110 (1970) 1

[40] D.Fleming et al., Nucl. Phys. A157 (1970) 1

[41] J.H.Bjerregaard et al., Nucl. Phys. 86 (1966) 145

[42] D.G.Fleming et al., Nucl. Phys. A163 (1971) 401.

[43] G.Igo, P.D. Barnes and E.R. Flynn. Annals of Physics 66 (1971) 60 and reference theirein.

[44] D.R.Bes and R.A.Broglia, Phys.Rev.C3.(1971) 2349.

[45] R.F.Casten et al., Phys.Lett. B40,333 (1972).

[46] J.V.Maher et al., Phys. Rev. Lett 25, 302 (1976).

[47] R.E.Griffin Jackson and Volkov Phys.Lett. 36B, 281 (1971)

[48] I.Ragnarsson and R.A. Broglia Nucl.Phys A263 (1976) 315-348.

[49] W.I.van Rij and Kahana Phys. Rev Lett 28 (1972) 50.

[50] W.D.Kulp et al., Phys. Rev. C71, 041303(R) (2005).

[51] W.D.Kulp et al., Phys. Rev. Lett. 91, 102501 (2006).

[52] A.Gavron, Phys.Rev. C21 (1980) 230-236.

[53] W.Reisdorf, Z.Phys.A 300,227 (1981).

[54] F.Puhlhofer et al., Nucl.Phys.A280(1977)267.

[55] G.Viesti et al., Phys. Rev.C 38 (1988) 2640.

[56] http://www.fresco.org.uk/

[57] T. Czosnyka, D. Cline and C. Y. Wu, GOSIA manual (2012)

[58] 52 International Winter Meeting on Nuclear Physics, Bormio (Italy). 27-31January 2014.

[59] NuShellX, W.D.M. Rae, http://wwww.garsington.eclipse.co.uk.

[60] http://www.geant4.org/geant4/

[61] N.Bohr, Nature 137, 344 (1936).

[62] S.E. Vigdor, Lecture Notes, XHI-th Masurian Summer School on Nuclear Physics, Makolajki, Poland, Sept. 1-11, 1980.

[63] S.E. Vigdor, H.J. Karwowski, W.W. Jacobs, S. Kailas, P.P. Singh, F. Soga, and T.G. Throwe, Phys. Rev. C 21. 1035 (1982).

[64] https://www.mdpi.com/2218-2004/1/1/2/pdf.

[65] U.Facchini and E. Saetta-Menichella, Energ. Nucl. 15 54 (1968).

[66] H.A. Bethe Fizika iadra, part 2. Moscow-Leningrad, 1948 (Translated from English).

[67] L. Landau and Ia. Smorondinskii. Lektsii po teorii atomnogo iadra. Moscow 1955.

[68] V. Weisskopf Statisticeskaia teoriia iadernykh reaktsii. Moscow, 1952. (Translated from English).

[69] W.Hauser, H. Feshbach, Phys. Rev.87 366 (1952)

[70] https://www.osti.gov/servlets/purl/799575

[71] Durham E F and Halbert M L 1965 Phys. Rev. B 137 850.

[72] W.Bothe W. Gentner, Z. Phys.112, 45 (1939)

[73] Migdal, A.B.1945. Zh.Eksp.Teor.Fiz.,15,81.

[74] Brink D M 1955 Thesis Oxford 101

[75] http://cdfe.sinp.msu.ru/

[76] P.D.Kunz, University of Colorado, Computer code CHUCK3, unpublished.

[77] M.Brekiesz et al., Nuclear Physics A, 2007 and reference thierein.

[78] R.W.Ibbotson et al., Nuclear Physics A 619 (1997) 213-248.

[79] J.Vervier, P. Mareschal Zeitschrift fr Physik A Atomic Nuclei.

[80] WP.Alford et al., Nuclear Physics A321 (1979) 45-61.

[81] K. Alder et al., Rev. Mod. Phys. 28 432 (1956).

[82] Mokgolobotho nsc.pdf https:// etd.uwc.ac.za/

[83] NuShellX@MSU,B.A. Brown, W.D.M. Rae, E.McDonald and M. Horoi, http://www.nscl.msu.edu/ brown/resources/resources/.html.

[84] B.A. Brown et al., Nuclear Data Sheets 120 (2014) 115-11

[85] GLOECKNER INTERACTION (FINAL) NPA253, 301 (1975).

[86] T.Konstantinopoulos et al., Phys. Rev. C95, 014309 (2017).

[87] T.Dossing: Licentiat Thesus, University of Copenhagen, (1977)

[88] D.Mahboub et al., PHYSICAL REVIEW C 69, 034616 (2004)

[89] P.Wong et al., Nucl. Phys. A151;549-560 (1970)

[90] Davide-specialistica.pdf http://www.infn.it

[91] J.Janecke et al., Nuclear Physics A325 (1979) 337-388.

[92] Particles and Nuclei An Introduction to the Physical Concepts.

[93] H.W.Fielding et al., Nucl. Physics A269 (1976) 125-137.

[94] N.Y. Kheswa et al., Nuclear Instruments and Methods in Physics Research A 655 (2011) 85-87.

[95] D.C. Radford Nucl. Instr. and Methods in Physics Research A361 (1995) 297-305.

[96] W.R. Leo. Techniques for Nuclear and Particle Physics Experiments. Springer-Verlag Berlin Heidelberg, 1987.

[97] http://etd.uwc.ac.za maqabuka phd nsc 2018

[98] https://midas.triumf.ca/MidasWiki/index.php/Main

[99] http://etd.uwc.ac.za Easton jl msc ns 2011

[100] https://www.root.cern.ch/

[101] http://scholar.sun.ac.za/handle/10019.1/20123

[102] https://midas.triumf.ca/MidasWiki/index.php/Main

[103] J.S. Thomas et al., Phys. Rev. C86, 047304 (2012).

[104] P. Papka ISTROS conference, Bratislava, Slovakia, 1-6 May 2015

[105] C.M. Lederer et al., Nuclear Physics A169 (1971) 449-488.

[106] P.Debenham et al., Nucl.Physics. A195 (1972) 385-414.

[107] J.V THOMPSON et al., Can. J. PHYS.53.1975.

[108] R.J. Peterson et al., Nucl. Physics A348 (1980) 8-24.

[109] L.B. Horodynski et al., Nuclear Physics A 709 (2002) 73-84.

[110] F.K McGowan et al., Nucl.Physics A113 (1968) 529-542.

[111] P.Van ISACKER et al., Nucl. Physics A348 125-139.

[112] D.Troltenier et al., Z. Phys A Hadrons and Nuclei 338, 261-270 (1991).

[113] A.J Radich et al., Physical Review C 91 044320 (2015).

[114] J.L Wood et al., Nucl. Phys A651 323.

[115] W. Urban et al., Acta. Phys. Pol. B32, 2527 (2001).

[116] J.K. Hwang et al., Physical Review C 67, 054304 (2003).

[117] S K Abdulvagabova et al., Phys. Lett. 38, 215333333 (1972).

[118] R.J.Petersen and J.D. Garrett Nucl. Phys. A414 (1984) 59-66.

[119] J.F. Sharpey-Schafer et al., Eur. Phys. J.A 47,6(2011).

[120] W.Oelert et al., 58 Phys. Rev.C Vol 12 number 5.

[121] P.E.Garret et al., J.Phys. G; Nucl. Part.Phys 27 (2001) R1-R22.

[122] A.Passoja et al., J. Phys.G:Nucl.Phys 12 (1986)1047-1057.

[123] R.J. Keddy et al., Nucl. Physics A113 (1968) 676-688.

[124] E.I Obiajunwa et al., Nucl. Phys. A500,341 (1989).

[125] A.Passoja et al., J. Phys.G:Nucl.Phys 12 (1986)1047-1057.

[126] 52 International Winter Meeting on Nuclear Physics, Bormio (Italy). 27-31 January 2014.